NTNU
Norwegian University of
Science and Technology

The Effect of Hydrogen on the Corrosion Resistance of Stainless Steel in Seawater

Henrik Horten Olavesen

Chemical Engineering and Biotechnology
Submission date: June 2018
Supervisor: Ida Westermann, IMA
Co-supervisor: Roy Johnsen, MTP
Andreas Erbe, IMA
Cristian Torres Rodriguez, MTP

Norwegian University of Science and Technology
Department of Materials Science and Engineering

Preface

This master thesis is written at the Department of Material Science and Engineering at the Norwegian University of Science and Technology (NTNU) during the spring semester of 2018. The work has been done in collaboration with Framo, where the goal has been to investigate the effect of hydrogen on the corrosion resistance of stainless steel in seawater.

The work presented has been performed by the author, except for the XPS analysis which was performed and analysed by Amin Hossein Zavieh, and the SEM images which were obtained with the assistance from Cristian Torres Rodriguez. The experimental work has been conducted at the Department of Mechanical and Industrial Engineering and at the Department of Material Science and Engineering.

The thesis is a continuation of the project "The Effect of Hydrogen on the Corrosion Resistance of Super Duplex Stainless Steel in Seawater" conducted by the author during the fall semester of 2017.

Trondheim

June 27, 2018

Henrik Horten Olavesen

Acknowledgements

I would like to thank my supervisors Ida Westermann[1], Roy Johnsen[2] and Andreas Erbe[1] for thorough guidance during the project. It has been interesting to be part of the project and see the relevance of the study through presentation of the results at international conferences in Copenhagen and Milan. A special thanks is extended to Roy Johnsen for taking the time to discuss results and for showing great interest in the project, inspiring me to work harder.

I would also like to extend my gratitude to Cristian Torres Rodriguez[2] and Mats Ingdal[2] for sharing their knowledge regarding practical measurements in the laboratory. I wish to thank Amin Hossein Zavieh[2] for his work on the XPS analysis and sharing of his knowledge on the matter. Further, I would like to extend my gratitude to technical staff both at the Department of Materials Science and Engineering and at the Department of Mechanical and Industrial Engineering for technical training and help with equipment.

I also want to thank the people I have gotten to know in Trondheim for five fantastic years, my time here would not have been the same without you. Lastly, I want to thank both my family and Sarah for encouragement, support and for always pushing me to work harder during these five years.

[1]Department of Materials Science and Engineering, NTNU, Trondheim
[2]Department of Mechanical and Industrial Engineering, NTNU, Trondheim

Abstract

Stainless steels have been used for various applications in the oil and gas industry for a long time due to, among others, their high corrosion resistance. However, immersion in seawater is demanding of the material because of varying temperatures and the presence of Cl^- ions. Cathodic protection (CP) in the form of sacrificial anodes is therefore typically applied to protect the stainless steel parts. It has been observed that cathodically protected stainless steels suffer from hydrogen induced stress cracking (HISC), believed to have been caused by the hydrogen development during CP. After the sacrificial anodes were removed, severe corrosion attacks occurred on the materials, suspected to have initiated due to adsorbed hydrogen during CP.

The objective of this work has been to investigate the effect of absorbed hydrogen on the corrosion resistance of stainless steel. Samples from two different batches of UNS S32750 have been used as well as samples from UNS S31254. Welded samples of the second batch of UNS S32750 were also provided. Simulation of cathodic protection was performed through cathodic polarisation of the samples at fixed current densities. The effect of different hydrogen charge current densities (HCCD) and storage time after charging were investigated on anodic polarisation curves and the critical crevice corrosion temperature (CCT). The oxide film composition was examined with X-ray photoelectron spectroscopy (XPS), and the electrical properties of the oxide film were studied with Mott-Schottky analysis. Scanning electron microscope (SEM) and energy-dispersive X-ray spectroscopy (EDS) were used to evaluate selective corrosion.

The results reveal a clear decrease in corrosion resistance of samples charged with hydrogen. A decrease in corrosion potential, E_{corr}, and an increase in anodic current density was observed in the polarisation curves. The decreased E_{corr} for charged samples was explained by the low equilibrium electrode potential of hydrogen oxidation compared to that of Fe oxidation. The CCT of charged samples decreased compared to uncharged samples. Storage time, however, resulted in higher E_{corr}, lower anodic current densities and increasing CCTs, indicating improved corrosion resistance with storage time. During storage, hydrogen diffuses out of the stainless steel, leading to repassivation. SEM and EDS results confirmed selective corrosion of the austenite phase. Results obtained with XPS revealed a higher relative atomic percentage of $Cr(OH)_3$ in the oxide film on hydrogen charged samples, implying lower corrosion resistance due to the higher defect concentration in hydroxides compared to

protective oxides like Cr_2O_3 and CrO_3, and thus a higher conductivity in the oxide layer. The Mott-Schottky analysis showed electric properties of the oxide film which were contradicting to previous studies, and the limitations of the method are discussed.

The work presented in this thesis shows that hydrogen has a detrimental effect on the corrosion resistance of stainless steel in seawater. The reason for the decreased resistance is likely caused by interactions between hydrogen and the oxide film, resulting in higher concentrations of hydroxides compared to oxides, thereby destabilising the film, and facilitating easier and faster corrosion.

Sammendrag

Rustfrie står har over lang tid blitt brukt til forskjellige formål i olje og gass industrien, blant annet på grunn av materialets høye korrosjonsbestandighet. Eksponering i sjøvann er krevende for materialet på grunn av varierende temperaturer og tilstedeværelse av Cl^- ioner. Katodisk beskyttelse (CP) i form av offeranoder blir derfor typisk brukt til å beskytte rustfrie stål. Observasjoner viser at katodisk beskyttet stål er utsatt for hydrogenindusert sprekking (HISC), som antas å være forårsaket av hydrogenutviklingen fra CP. Etter fjerning av offeranodene, oppstod det kraftige korrosjonsngrep på materialene, som antas å ha initiert på grunn av absorbert hydrogen fra CP.

Formålet med denne oppgaven har vært å undersøke effekten av absorbert hydrogen på korrosjonsbestandigheten til rustfritt stål. Prøver fra to forskjellige batcher av UNS S32750 har blitt brukt i tillegg til prøver fra UNS S31254. Sveisede prøver fra den andre batchen med UNS S32750 ble også levert. Simulering av katodisk beskyttelse ble gjennomført ved katodisk polarisering av prøvene ved gitte strømtettheter. Effekten av ulike strømtettheter for hydrogenlading og lagringstid etter hydrogenlading ble undersøkt ved anodiske polarisasjonskurver og kritisk spaltkorrosjonstemperatur (CCT). Komposisjonen til oksidfilmen ble analysert med røntgen fotoelektron spektroskopi (XPS), og de elektriske egenskapene til oksidfilmen ble undersøkt med Mott-Schottky analyse. Skanning elektronmikroskop (SEM) og energi dispersiv røntgen spektroskopi (EDS) ble brukt til å undersøke og evaluere selektiv korrosjon i hydrogenladete prøver.

Resultatene viser en klar nedgang i korrosjonsbestandigheten til prøver ladet med hydrogen. En nedgang i korrosjonspotensialet, E_{corr}, og en økning i anodisk strømtetthet ble observert på polarisasjonskurvene. Nedgangen i E_{corr} for ladede prøver ble forklart ved det lave likevektspotensialet til hydrogenoksidasjon i forhold til jernoksidasjon. CCT til ladete prøver sank i forhold til uladete prøver. Lagringstid førte til en økning i E_{corr}, lavere anodisk strømtetthet og høyere CCTer, noe som indikerer bedre korrosjonsbestandighet om prøver ble lagret etter hydrogenlading. I løpet av lagringen vil hydrogen diffundere ut av det rusfrie stålet, og føre til repassivering. SEM og EDS resultatene bekreftet selektiv korrosjon av austenitt fasen. Resultatene oppnådd fra XPS analysen viste en høyere relativ prosent av $Cr(OH)_3$ i oksidfilmen på hydrogenladete prøver, som impliserer en lavere korrosjonsbestandighet på bakgrunn av en høyere defektkonsentrasjon i hydroksider sammenlignet med mer beskyttende oksider som cr_2O_3 og CrO_3, som igjen fører til høyere konduktivitet i oksidfilmen. Mott-Schottky

analysen viste elektriske egenskaper for oksidfilmen som var motsigende til tidligere studier og begrensningene til denne typen analyse er derfor diskutert.

Arbeidet som blir presentert i denne oppgaven viser klart at hydrogen har en skadelig effekt på korrosjonsbestandigheten til rustfritt stål i sjøvann. Grunnen til nedgangen i korrosjonsbestandighet skyldes sannsynligvis interaksjoner mellom hydrogen og oksidfilmen, noe som resulterer i høyere konsentrasjoner av hydroksider sammenlignet med oksider. Dette fører til destabilisering av filmen og fasilitering av lettere og raskere korrodering av det rustfrie stålet.

Abbreviations and nomenclature

Abbreviations

ASS	Austenitic stainless steel
CCT	Critical crevice corrosion temperature
CE	Counter electrode
CP	Cathodic protection
DSS	Duplex stainless steel
EDS	Energy dispersive X-ray spectroscopy
HAZ	Heat affected zone
HCCD	Hydrogen charge current density
HER	Hydrogen evolution reaction
HISC	Hydrogen induced stress cracking
ICPOES	Inductively coupled plasma optical emission spectroscopy
OCP	Open circuit potential
ORR	Oxygen reduction reaction
PDM	Point defect model
PREN	Pitting resistance equivalent number
RE	Reference electrode
RMS	Root mean square
SASS	Super austenitic stainless steel

SDSS	Super duplex stainless steel
TTT	Time-temperature-transformation
WE	Working electrode
XPS	X-ray photoelectron spectroscopy

Nomenclature

α	Ferrite
χ	Secondary phase chi
ΔE	Potential drop
γ	Austenite
γ_2	Secondary austenite
ν	X-ray frequency
ϕ	Instrument spectrometer work function
σ	Secondary phase sigma
ε	Dielectric constant
ε_0	Vacuum permittivity
C	Total capacitance
C_{H}	Helmholtz double layer capacitance
C_{SC}	Space charge layer capacitance
D_{H}	Effective hydrogen diffusivity
D_{L}	Ideal lattice diffusivity
E_{app}	Applied potential

E_{B}	Binding energy of hydrogen
E_{corr}	Corrosion potential
E_{FB}	Flat band potential
E_{f}	Passive film formation potential
E_{k}	Kinetic energy
E_{M}	Minimum energy barrier
E_{pit}	Pitting potential
I	Current
i_{corr}	Corrosion current density
i_{pass}	Passive current density
k	Value between 16 and 30 used to estimate PREN
N_{a}	Acceptor density
N_{d}	Donor density
R	Resistance

Contents

1 Introduction

Stainless steels have been used for industrial purposes for a long time. These materials are especially favored in the oil and gas industry because of the combination of good mechanical abilities and high corrosion resistance to both general and localised corrosion [1]. Corrosion resistance is a material's ability to resist deterioration of e.g. mechanical strength and surface appearance originating from corrosive attacks [2]. Super duplex stainless steels (SDSS) are a high alloyed version of stainless steels, which have experienced increased interest over the last years because of valuable properties, like corrosion resistance, in chlorinated environments like seawater [1]. Framo[3] has been delivering seawater lift pumps made from UNS S32750 grade super duplex stainless steel to the oil and gas industry for many years. During operation, the pump systems are exposed to a wide variety of seawater temperatures, ranging from cold water with temperatures of 5-10 ℃ to warm water with a temperature of 35 ℃. Chlorinated environments with varying temperatures are demanding for the material. Thus, to increase the lifetime of the pump systems under these conditions, cathodic protection (CP) in the form of sacrificial anodes are used. During cathodic protection, hydrogen may form on the surface of the pump system. Hydrogen induced stress cracking (HISC) has been observed on some of the pipe systems during operation, and is believed to have been caused by the hydrogen development on the surface. The cracks always initiated close to welded areas, and residual stress in the material is therefore a major contributing factor to the cracking. In order to avoid further attack by HISC, the sacrificial anodes initially used as protection were removed for selected pumps after a few years in operation. After removal of the sacrificial anodes, the pump systems suffered from severe corrosion attacks. The reason for the attacks is believed to be caused by absorbed hydrogen in the stainless steel, originating from the hydrogen formation during cathodic protection, causing decreased corrosion resistance and thereby promoting faster and earlier corrosion [3]. The objective of this work has thus been to investigate the effect of absorbed hydrogen on the corrosion resistance of the UNS S32750 grade super duplex stainless steel and the UNS S31254 super austenitic stainless steel.

This master thesis is a continuation of the specialisation project "The Effect of Hydrogen on the Corrosion Resistance of Super Duplex Stainless Steel in Seawater" conducted by the author, where the same research question was investigated exclusively for UNS S32750 grade stainless steel [4]. The effect of different hydrogen charge current densities (HCCD)

[3] https://www.framo.com/

on polarisation curves and critical crevice corrosion temperature (CCT) were investigated. Polarisation curves were obtained both at room temperature and at 60 ℃.

In this master thesis, the research done in the specialisation project will be continued and extended. The effect of storage time after hydrogen charging on corrosion resistance is investigated through polarisation curves and CCT measurements. Stainless steel of both welded and unwelded UNS S32750 grade, as well as UNS S31254 grade are used in the experimental work. Chemical analysis of the passive oxide layer before and after hydrogen charging of UNS S32750 grade stainless steel is performed using X-ray photoelectron spectroscopy (XPS), and Mott-Schottky analysis is used to better understand the electrical behaviour of both charged and uncharged UNS S32750 grade steel. In addition, a scanning electron microscope (SEM) coupled with energy dispersive X-ray spectroscopy (EDS) is used to investigate whether selective corrosion occurs in hydrogen charged UNS S32750 grade stainless steel.

2 Theory

Parts of section 2.1 to 2.3.2 have been written based on previous work by the author [4].

2.1 Super duplex and super austenitic stainless steel

Stainless steels are iron alloys that contain a chromium content of at least 12 wt%. Based on microstructure, these alloys can be divided into four groups. These are ferritic, austenitic, martensitic and ferritic/austenitic. Duplex stainless steels (DSS) are ferritic/austenitic steels where the ferrite and austenite phases are present in large, separate volumes of relatively equal amounts. Super duplex stainless steels (SDSS) are highly alloyed versions of DSS. These steels contain a minimum of 25 wt% chromium and exhibit good mechanical properties as well as resistance to stress corrosion cracking and localised corrosion [1].

Austenitic stainless steel (ASS) is the most commonly used type of stainless steel [5]. This type of stainless steel, containing a much higher amount of austenite than the duplex and super duplex stainless steels, commonly contains between 16 and 25 wt% chromium. Austenitic steels can in addition contain a small amount of nitrogen, and both chromium and nitrogen contribute to the good corrosion resistance exhibited by these stainless steels [5]. Nickel is one of the most important alloying elements added to austenitic stainless steel, as it stabilises the austenite phase at room temperature [6]. This will be discussed further in section 2.1.2. Super austenitic stainless steel (SASS) is a highly alloyed version of the austenitic stainless steel. These alloys contain a large amount of molybdenum, which makes it necessary to add even more chromium and nickel to stabilise the austenite phase [6].

2.1.1 Microstructure

DSS and SDSS obtain their favorable properties from the dual phase composition of ferrite (α) and austenite (γ). This combination of microstructure gives the material the mechanical abilities of a ferritic stainless steel while also providing the corrosion resistance of an ASS [7]. This dual phase composition is shown in Figure 2.1.

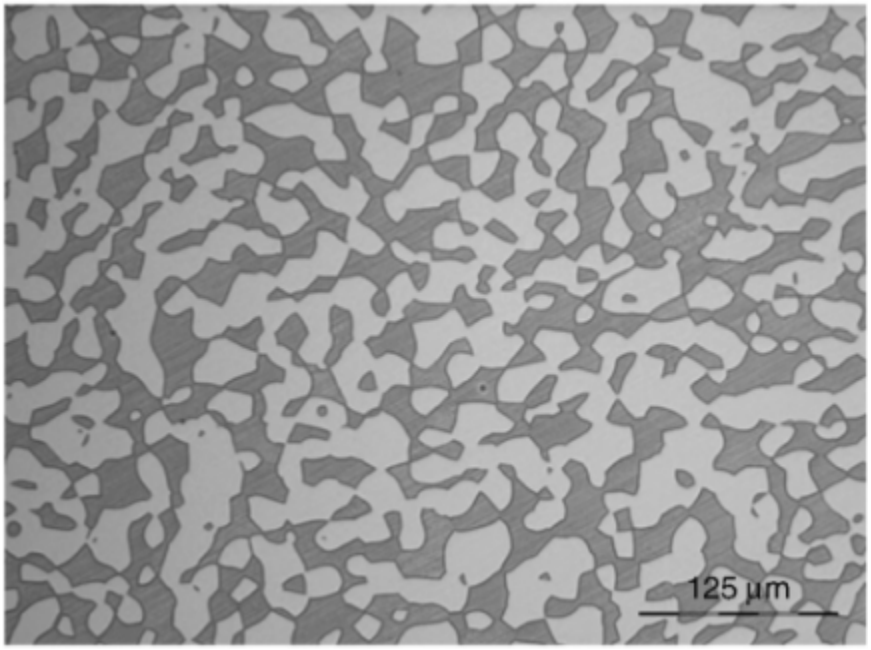

Figure 2.1: The dual phase composition of UNS S32750 SDSS, with dark α-phase and lighter γ-phase [8].

DSS and SDSS have γ-contents ranging from 35 volume% to 65 volume%. The optimal mechanical properties and corrosion resistance are obtained when the amounts of α and γ are roughly equal [9, 10]. To obtain this preferred composition, a variety of alloying elements are used, and these will be discussed in section 2.1.2. α and γ have different properties regarding hydrogen. α exhibits a high diffusivity and low solubility of hydrogen, whereas γ exhibits the opposite properties; a low diffusivity and high solubility. Thus, when hydrogen is absorbed by SDSS, γ will by saturated with hydrogen, while α will inhibit a much lower concentration [11].

2.1.2 Effect of alloying elements

Chromium

Chromium (Cr) is a α stabiliser which closes the γ-loop, shown in the equilibrium phase diagram of iron and chromium in Figure 2.2. Based on this equilibrium phase diagram, it is clear that Cr is more soluble in α than in γ. When Cr is added to steel, the formation of

α becomes favoured. However, when Cr is added to nickel rich steels, the $\gamma \rightarrow \alpha$ formation is delayed which makes it easier to maintain γ down to room temperature. When more than 25 wt% Cr is added to the stainless steel, formation of the secondary phase sigma (σ) occurs, which is undesired. This will be treated further in section 2.1.3. The main reason for addition of Cr to stainless steel is to increase the corrosion resistance of the material by formation of a thin oxide layer containing Cr on the surface [6]. This surface layer will be explained further in section 2.2.1.

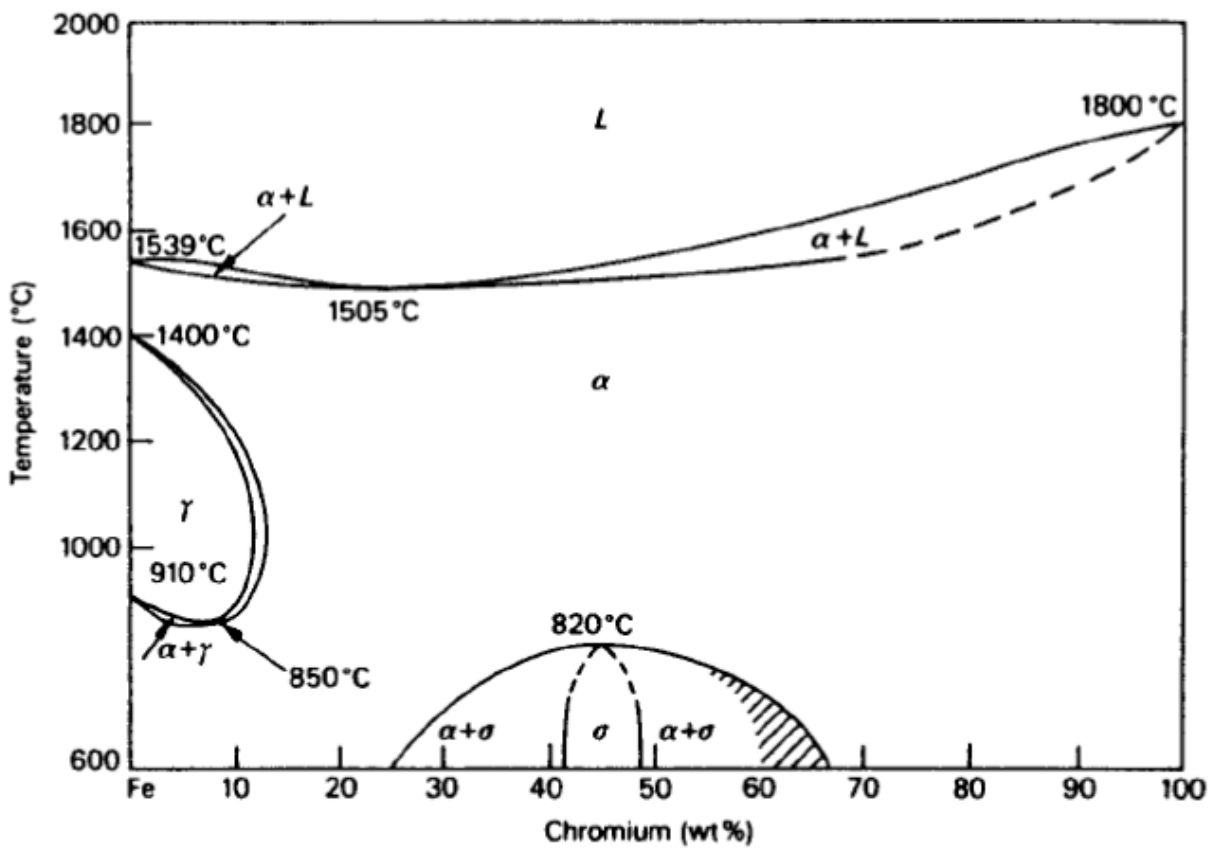

Figure 2.2: The equilibrium phase diagram of iron and chromium [6].

Molybdenum

Molybdenum (Mo) is a α stabiliser, found to be more soluble in α than γ [9]. For a long time it has been known that addition of Mo to austenitic Cr−Ni stainless steels increases the pitting corrosion resistance in chloride environments [12]. Cr is needed together with Mo to increase the pitting corrosion resistance [12]. Mo exists in the passive oxide layer of stainless steel in many different oxidation states. A majority of studies have shown that Mo^{4+} is found in the inner layer, while Mo^{6+} is found in the outer layer. The reason of why Mo increases the resistance to pitting is not well known [13]. Studies have reported that molybdenum in Cr−Ni stainless steels thickens the passive oxide layer [14], while other studies suggest that Mo impedes the adsorption of chloride on the surface by increasing the oxygen affinity of the stainless steel, thereby making it more corrosion resistant [15].

Nickel

Nickel (Ni), as can be seen in Figure 2.3, is an γ stabiliser that extends the γ phase field when added to stainless steel with high chromium content. Ni is found to be more soluble in γ than in α [9]. When the Cr content of stainless steel increases, higher amounts of Ni are required to maintain γ down to room temperature. For instance, for SDSS with a Cr content of 25 wt%, about 15 wt% Ni is needed to achieve a stable γ phase at room temperature [6]. On the other hand, a SASS containing 20 wt% Cr and 6,5 wt% Mo would need a Ni content of up to 24 wt% to stabilise the γ phase at room temperature [6]. When Ni is present in stainless steel, the corrosion resistance increases noticeably, especially in strongly reducing environments like acids because of Ni's low solubility in acid [9].

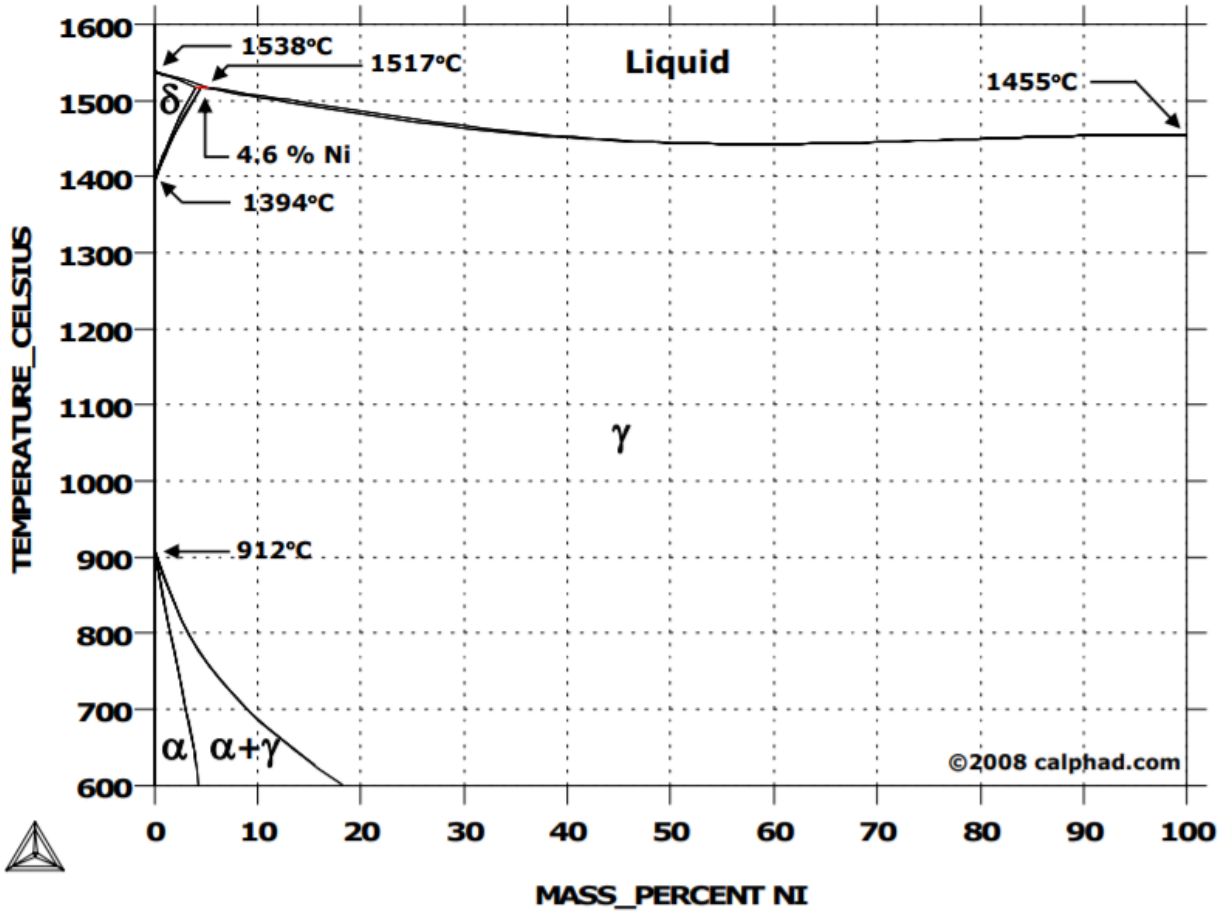

Figure 2.3: The equilibrium phase diagram of iron and nickel [16].

Manganese

Manganese (Mn) is, like Ni, an γ stabiliser expanding the γ phase field. However, it is only about half as effective av Ni. Thus, higher concentrations of Mn are needed to stabilise the γ phase. For stainless steels without Cr, a Ms content of approximately 12 wt% is needed, and this number increases with addition of more Cr [6].

Nitrogen

Nitrogen (N) is commonly added to steel to stabilise the γ. However, it is found that when N is present in combination with Mo, a significant increase in both the general and localised

corrosion resistance occurs [13]. With an increasing amount of N, an increased sensitivity to formation of secondary phases arises. SDSS, which has a high content of both Cr and N, thus exhibits a high susceptibility to formation of chromium nitrides [17]. N is mainly partitioned to the γ phase, but it is found that with increasing temperature, the concentration of N in the α phase also rises.

2.1.3 Heat treatment and secondary phases

Secondary phases are known to form in SDSS in the temperature range from 300-1000 °C. The most important phases are σ, chromium nitrides, secondary austenite (γ_2) and the chi-phase (χ). The σ phase is of special importance due to its influence on both toughness and corrosion resistance of the steel [1, 18]. A time-temperature-transformation (TTT) diagram contains information about the temperature ranges and holding times for the different secondary phases, and the TTT-diagram of UNS S32750 can be seen in Figure 2.4. As can be seen from the TTT-diagram, temperatures between 800 and 1000 °Cshould be avoided for longer periods of time, as that is the range in which σ-, γ_2-, χ-phases and chromium nitrides precipitate [1].

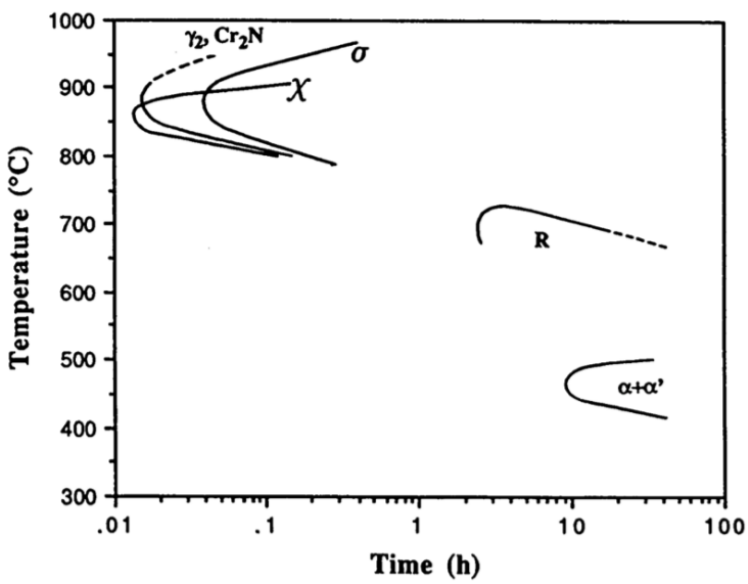

Figure 2.4: The TTT-diagram of UNS S32750 [1]. The R-phase and $\alpha + \alpha'$-phase are not discussed further in this work.

σ phase

Studies have shown that the σ phase is formed in a large number of stainless steels. This precipitation is found in both SDSS and SASS because of the large content of both Cr and Mo. Mo is also known to increase the stability of the σ phase towards higher temperatures [1]. Nucleation and growth of this secondary phase occurs mostly in α or at α/γ phase boundaries. This is because α has a high Cr and Mo content, which also holds true for the σ phase [1, 19]. The formation of σ follows the eutectic reaction given in reaction 2.1 [1].

$$\alpha \rightarrow \gamma_2 + \sigma \tag{2.1}$$

The σ phase is very brittle and affects ductility negatively at both room temperature and higher temperatures. Due to the high Cr content in σ, the areas surrounding the phase are depleted of Cr. This is believed to be the reason for the decreased corrosion resistance [18, 1]. With increasing aging time, the corrosion resistance of stainless steel is found to decrease even more, due to formation of γ_2 around the σ phase [18].

γ_2 phase

γ_2 can form during the same eutectoid reaction as the σ phase. The eutectoid reaction is facilitated by rapid diffusion along α/γ boundaries, which results in a microstructure of σ and γ_2 in the α grains. The γ_2 formed on these phase boundaries is low in Cr, especially when chromium nitrides form in cooperation. This results in low corrosion resistance in these areas, and explains why pitting corrosion is a problem when γ_2 precipitates in SDSS [1].

Chromium nitrides

As mentioned in section 2.1.2, SDSS contains high amounts of both Cr and N, which makes the stainless steel susceptible to precipitation of chromium nitrides. N is mostly partitioned to γ, but nitrogen content increases in α with increasing temperature. Since α is rich in Cr it is more likely that chromium nitrides form with increasing temperature in α [19, 17].

Chromium nitrides precipitate inside α grains when the temperature rapidly decreases, but may also form during isothermal heat treatment. By adjusting the heat treatment temperature, the formation of chromium nitrides can be avoided. However, chromium nitrides formed during rapid decrease of temperature are difficult to avoid, since the precipitation occurs during quenching of the metal. Thus, the cooling rate affects the precipitation of this secondary phase. An increased cooling rate results in precipitation within smaller α grains, and the precipitates are simultaneously increasing in size leading to decreased corrosion resistance [17].

χ phase

χ phase forms prior to the σ phase on the α/α interface and later grows into the α. χ phase is thermodynamically unstable, and the σ phase will thus form on the expense of the χ phase [20]. The χ phase has an adverse effect on both the corrosion resistance and toughness of stainless steels, but it is difficult to quantify this effect, as the χ phase always occurs as a minor phase together with the σ phase [1, 21].

Welding of stainless steel

During welding of stainless steel undesirable effects can develop in the resulting metal. Welding creates a heat affected zone (HAZ) which experiences temperature peaks ranging from room temperature at the edges, to melting temperatures closer to the weld area. The cooling and heating rates can also vary greatly, depending on heat input, structure of the material and position relative to the weld zone [1]. SDSS generally exhibit good weldability with regards to fluidity and resistance to hot cracking and delayed weld hydrogen cracking. However, an important part of welding SDSS is to control the thermal cycle to ensure that a desirable α/γ ratio is achieved in the welded metal and the HAZ. Equally important is the hindering of secondary phase formation, especially the σ phase [21].

2.2 Corrosion of stainless steel

2.2.1 The passive oxide layer

As mentioned in section 2.1.2, the corrosion resistance of stainless steel can be attributed to the oxide layer formed on the surface. The structure of this oxide film is complex, and often described as bi-layered. The inner layer of the structure is enriched in chromium oxides like Cr_2O_3 and CrO_3, while the outer layer is a mixture of iron oxides and other hydroxides [22]. Other species also play an important role for the properties of the passive film. The formation of $Cr(OH)_3$ in the passive film promotes localised corrosion, while Mo has been found to enhance the formation of more stable compounds from Cr^{3+} and Cr^{6+} ions [23, 24]. It has also been suggested that Mo slows down the corrosion process through formation of compounds that adsorb corrosive species like Cl^- [25].

It has been found that the inner layer of the passive film functions as a p-type semiconductor, while the outer layer functions as an n-type semiconductor. Between the two layers, a clear p-n junction has been observed. When stainless steel samples of 2205 DSS have been charged with varying HCCDs, there has been observed a weakening of the p-n junction. This is caused by a gradual conversion of the p-type semiconducting properties of the inner layer to n-type behaviour [26]. The same effect is also documented for the austenitic stainless steel, AISI 310 [27]. A conversion of the p-type behaviour of the passive layer was changed to n-type behaviour with increasing HCCD. The n-type behaviour was also linked to an increased susceptibility to pitting corrosion [27]. The acceptor density in the p-type chromium oxide layer and the donor density of the n-type Fe-rich outer layer have been found to decrease when Mo is used as an alloying element [25].

2.2.2 Pitting corrosion

Pitting corrosion is a localised form of corrosion, which is hard to predict and model. Pitting may therefore result in catastrophic failure of metal components during operation [2]. Pitting corrosion typically initiates through breakdown of the passive film on the metal surface, through e.g. defects or intermetallic phases, in chloride containing environments [2, 28]. Metals which form a passive film and contain alloying elements, like stainless steels, are therefore susceptible to pitting corrosion. During the attack, an electrochemical cell is

formed, with the anodic site being the small area where the passive film is broken, and the rest of the metal surface acting as the cathodic cite. Such a small anodic to cathodic area ratio is unfavorable, as large current flows occur on the small, anodic area, accelerating the corrosion process. At the anodic site, iron in stainless steels will dissolve according to [2]

$$\mathrm{Fe} \longrightarrow \mathrm{Fe}^{2+} + 2\,\mathrm{e}^- \tag{2.2}$$

whereas oxygen reduction will occur on the larger, cathodic site according to [2]

$$\frac{1}{2}\,\mathrm{O_2} + \mathrm{H_2O} + 2\,\mathrm{e}^- \longrightarrow 2\,\mathrm{OH}^-. \tag{2.3}$$

The positive iron ions inside the pit will attract negatively charged chloride ions to neutralise the charge difference between the inside and the outside of the pit [2], resulting in the formation of $FeCl_3$. The iron chloride reacts with water to form corrosion products according to [2]

$$\mathrm{FeCl_3} + 3\,\mathrm{H_2O} \longrightarrow \mathrm{Fe(OH)_3} + 3\,\mathrm{H^+Cl^-}. \tag{2.4}$$

Reaction 2.4 renders the pit more acidic, accelerating the pitting corrosion process even more [2]. The corrosion product $Fe(OH)_3$ will assemble at the pit opening, and may after some time block the pit entrance and thereby stop the corrosion process.

As mentioned in section 2.1.2, Cr, Mo and N are the most efficient alloying elements to raise resistance to both crevice and pitting corrosion of stainless steels [29]. A pitting index has thus been derived to characterise the resistance of stainless steel to these forms of corrosion. This index is called the pitting resistance equivalent number (PREN), given by equation 2.5. The value for k in the equation can be between 16 and 30, but 16 is most frequently used [29, 1]. In ISO 21457, the PREN is defined with k equal to 16, and the weight percent of tungsten is also included in the equation [30]. PREN values for SDSS have to be equal to or higher than 40 if they are to be used in natural seawater [8].

$$PREN = wt\%Cr + 3.3 \cdot (wt\%Mo) + k \cdot (wt\%N) \tag{2.5}$$

2.2.3 Crevice corrosion

Crevice corrosion is a type of localised corrosion. The areas where crevice corrosion can occur are designated by low diffusion and convection between the inside of the crevice and the bulk solution. A high metal surface to solution volume ratio is needed, as well as presence of large external surfaces exposed to the bulk solution. For many cases of crevice corrosion, a significant solution resistance between the inside of the crevice and the outside is also needed. Crevice corrosion occurs due to a change in environment, which allows anodic dissolution of metal inside the crevice. For passive metals, like SDSS, the change in environment must become severe enough to break down the passive film. The change in environment inside the crevice is caused by local consumption of reactants, usually dissolved oxygen. This, coupled with a local build-up of corrosion products due to the low diffusion and convection with the outside of the crevice, results in the formation of a galvanic cell where the outside of the crevice functions as the cathode and the crevice itself as the anode. Anodic dissolution of the metal will thus happen inside the crevice according to equation 2.2. The surplus of cations in the crevice needs to be neutralised. Anions, like Cl^-, from the bulk are therefore transported into the crevice, resulting in a decrease in pH and further acceleration of the corrosion of steel [29].

2.3 Absorbed hydrogen in steel

Some of the most common ways for atomic hydrogen to enter steel are during corrosion in acidic or poorly aerated environments, during overpolarisation from cathodic protection and during pitting corrosion. Under these processes, the hydrogen evolution reaction (HER) is one of the cathodic reactions that may take place on the surface of the metal. The HER has two steps, given by the first two steps in reaction 2.6. These are adsorption of hydrogen at the surface of the metal and recombination into hydrogen gas. Some of the adsorbed hydrogen may be absorbed into the steel lattice according to the last step in reaction 2.6.

$$\begin{aligned} M + H^+ + e^- &\longrightarrow MH_{ads} \\ 2\,MH_{ads} &\longrightarrow 2\,M + H_2 \\ MH_{ads} &\longrightarrow MH_{abs} \end{aligned} \tag{2.6}$$

The hydrogen solubility in Fe is reported to be somewhere between 0.001 and 0.01 ppm below 100 ℃, while the solubility of hydrogen in stainless steel has been reported to be as high as 680 ppmw [31]. Thus, absorbed hydrogen may diffuse through the stainless steel lattice, based on concentration gradients in the lattice. Absorbed hydrogen moves through the stainless steel lattice by interstitial lattice diffusion, described by ideal lattice diffusivity (D_L). This parameter is related to the energy needed for hydrogen to overcome the minimum energy barrier (E_M) between different interstitial lattice sites. Existing trap sites in the lattice can block the lattice diffusion of hydrogen. Trap sites can be grain boundaries, dislocations or other particles in the stainless steel. Hydrogen can be irreversibly or reversibly trapped, depending on the binding energy of hydrogen (E_B) for the different sites. If E_B is too high, the trap site is known as an irreversible trap site and for a given temperature, hydrogen atoms will not have the necessary thermal energy to overcome the energy barrier. For reversibly trapped sites, E_B is small enough for the thermal energy to overcome the energy barrier. If $E_B > E_M$, the effective hydrogen diffusivity (D_H) will be lower than D_L. These reversibly trapped hydrogen atoms, as well as the lattice hydrogen are known as the net diffusible hydrogen atoms. These atoms can interact with the passive film and participate in interfacial reactions on the stainless steel surface. The initial diffusion rate of hydrogen through the stainless steel may be slow, as much of the hydrogen may be trapped irreversibly. As the trap sites fill with hydrogen, the diffusion rate increases until a steady-state diffusion is achieved. The hydrogen atoms will exit the stainless steel lattice and come into contact with the passive layer, which causes destabilisation. As hydrogen is a strong reducing agent, it can reduce oxygen, the passive film itself and oxygen containing species like O_2^- and OH^-. In other words, hydrogen alters the chemical composition of the passive film, which can further alter the electronic properties and promote destabilisation [32].

2.3.1 Cathodic protection

One of the most effective ways to protect metals against corrosion is the use of cathodic protection (CP). CP is used to protect a wide variation of metallic structures in many different environments. The protection is provided through connection of sacrificial anodes to the metal that is to be protected, and thereby turning the metal into a cathode. The sacrificial anode is made of a more active metal which will corrode before the protected metal. By using CP to protect a metal surface, the anodic reaction of metal dissolution shifts from the metal surface to the sacrificial anode [33]. The HER given in reaction 2.6 and the oxygen

reduction reaction (ORR) given in reaction 2.3, are the two most common cathodic reactions occurring on the metal surface during CP [34]. Thus, hydrogen is introduced to the metal during CP through reaction 2.6 [27].

2.3.2 Hydrogen induced stress cracking

The presence of hydrogen in steel is known to cause hydrogen embrittlement [32]. HISC is one of the results of hydrogen embrittlement, and is caused by three essential factors: stress in the steel (either applied or residual), a susceptible microstructure and the presence of hydrogen [35]. As mentioned in section 2.1.1, α has a higher hydrogen diffusivity than γ [11]. As a consequence, hydrogen diffusion happens mainly through the α phase. γ on the other hand, acts as a trapping site for the hydrogen because of its low diffusivity and high solubility [35]. When atomic hydrogen accumulates at these trap sites, it can form hydrogen gas, which increases the internal pressure in the steel. When this is coupled with applied or residual stress in the steel (from e.g. welding), microcracks can form at exposed sites. When enough microcracks have accumulated, the stainless steel can experience critical failure [36].

2.4 Semiconductors and Mott-Schottky theory

Semiconductors are distinguished from metals and insulators by electrical resistivity (ρ) and electrical bandgap. The electrical resistivity of metals is commonly around 10^{-8} Ωm, while insulators typically have electrical resistivity around 10^{10} Ωm. The electrical resistivity of semiconductors can be found in between metals and insulators, with the actual values depending on defects, impurities and ambient conditions [37]. The bandgap is the other determining factor for semiconductors. In a metal, the conduction and valence band overlap or have a very small band gap. This makes it easy for electrons to be excited from the valence band to the conduction band, thus metals are good current conductors. Insulators have a large bandgap, resulting in difficulties related to electron excitation from the valence band to the conduction band. Semiconductors are found in between, and always present some electric conduction [38]. Semiconductors are divided into two groups, namely intrinsic and extrinsic semiconductors. Intrinsic semiconductors are pure semiconductors without any kind of dopant species while extrinsic semiconductors have added dopant elements. Two different extrinsic semiconductors exist, depending on what the major charge carrier in the

semiconductor is. An n-type semiconductor uses electrons as charge carriers, while a p-type semiconductor uses holes as charge carriers [38].

Based on the point defect model (PDM), passive films are regarded as highly defective, where the main point defects are cation vacancies ($V_M^{x'}$), oxygen vacancies ($V_O^{\bullet\bullet}$) and cation interstitials (M_i^{x+}) [39, 40]. These ionic point defects are very important for conducting current through the passive film [40].

Mott-Schottky analysis is used to study electrode interfaces. When used on a passive system, like the oxide film on SDSS, information on the defect density and semiconductor behaviour can be gathered [41, 42]. The method measures capacitance of the passive system as a function of the applied potential, and the passive system can be regarded as two capacitors in series. Thus, the measured capacitance of the passive system can be expressed as

$$\frac{1}{C} = \frac{1}{C_{\mathrm{SC}}} + \frac{1}{C_{\mathrm{H}}} \tag{2.7}$$

where C is the measured total capacitance, C_{SC} is the space charge layer capacitance and C_{H} is the Helmholtz double layer capacitance [40]. Generally, the assumption that the double layer capacitance is much higher than the space charge capacitance is valid, resulting in the measured total capacitance being equal to C_{SC} [43].

According to Mott-Schottky theory, C_{SC} for semiconductors is given as

$$\frac{1}{C^2} = \frac{2}{\varepsilon\varepsilon_0 e N_{\mathrm{d}}}\left(E - E_{\mathrm{FB}} - \frac{kT}{e}\right) \tag{2.8}$$

and

$$\frac{1}{C^2} = -\frac{2}{\varepsilon\varepsilon_0 e N_{\mathrm{a}}}\left(E - E_{\mathrm{FB}} - \frac{kT}{e}\right) \tag{2.9}$$

for n-type and p-type semiconductors, respectively [42, 43, 44]. Here ε is the dielectric constant for the semiconductor, ε_0 is the vacuum permittivity, e is the charge of an electron, A is the surface area of the sample in cm^2, E is the applied potential, E_{FB} is the flat band potential, k is the Boltzmann constant, T is the absolute temperature and N_{d}

and N_a are the donor and acceptor densities, respectively [40, 45, 43]. The plots of C^{-2} versus E is thus expected to be linear, with slopes inversely proportional to N_d and N_a. A positive slope indicates n-type semiconductor behaviour, and a negative slope indicates p-type semiconductor behaviour [46, 44]. Oxides that generally exhibit p-type behaviour are Cr_2O_3, MoO_2, $FeCr_2O_4$, FeO, $Cr(OH)_3$ and NiO while Fe_2O_3, MoO_3, CrO_3, Fe_3O_4 and FeO(OH) generally exhibit n-type behaviour [45, 47].

2.5 XPS-analysis

XPS is a research tool used for surface chemical analysis. It can be used on a wide range of materials, from metals and oxides to composites and biomaterials. XPS is a way of determining the elements and relative composition present on a material surface, by determining the kinetic energy of photoelectrons ejected from the surface of the material. The method works by irradiating the surface with X-rays with constant energy, $h\nu$. The X-rays interact with core level electrons and transfer photon energy to the electrons, resulting in the emission of a photoelectron. The relationship between the energy of the X-rays and the kinetic energy of the photoelectron is given by equation (2.10).

$$h\nu = E_k + E_B + \phi \tag{2.10}$$

Here the h is the Planck constant, ν is the X-ray frequency, E_k is the kinetic energy of the photoelectron, E_B is the binding energy of the electron relative to the Fermi level and ϕ is the instrument's spectrometer work function. Since the photon energy and spectrometer work function are known, and E_k can be determined experimentally, the E_B can be found using equation (2.10). Binding energy of an electron in a particular shell of an atom is unique to each element, thus the values found for E_B identify elements present on the surface, and relative composition can be determined [48, 49]. XPS can also be used for depth profiling, and two methods are used; the non-destructive method or the destructive method. The non-destructive method varies the emission angle of the X-ray, thus making the surface more sensitive. To get an even deeper profiling, the destructive method must be used. Surface layers are then removed by inert gas sputtering, typically with argon, and XPS analysis is performed at each new surface. This gives the chemical composition of each layer. XPS can also be used to estimate the oxide thickness [49].

3 Materials and methods

3.1 Material selection and preparation

Test material of two different production batches of UNS S32750 grade stainless steel and one batch of UNS S31254 grade stainless steel were used in the experimental work. Welded UNS S32750 grade stainless steel samples from batch 2 were also supplied, and will be referred to as welded UNS S23750 samples henceforth. The composition of the stainless steel is given in Table 3.1. The test material was provided pre-pickled by Framo. However, the pickling solution used for batch 1 of UNS S32750 was less effective than the solution used for batch 2 of UNS S32750, welded UNS S32750 and UNS S31254. This was confirmed by Framo. Details concerning the pickling process can be found in Appendix A. Before use the samples were thoroughly cleaned with acetone and distilled water.

Table 3.1: Chemical composition, given in wt%, of the two batches of UNS S32750 and the UNS S31254 batch used in the experimental work, provided by Framo. Only the major alloying elements are listed, as well as PREN values. The full chemical compositions can be found in the material specification sheets in Appendix A.

Grade	Batch number	Cr	Mo	Ni	N	Mn	C	PREN
UNS S32750	1	25.02	3.79	6.87	0.28	0.75	0.017	41.9
	2	24.73	3.79	6.94	0.27	0.78	0.017	41.6
UNS S31254	-	20.10	6.37	18.36	0.20	0.55	0.017	44.3

Two different types of samples of the test materials were provided, shown in Figure 3.1. Samples of the first type were used to record polarisation curves and conducting the Mott-Schottky analysis, while samples of the second type were used to determine the critical crevice corrosion temperature (CCT). The total surface area of both samples was 37 cm^2, and the dimensions of the samples were 4 cm $\times$ 4 cm $\times$ 0.3 cm. The diameter of the small holes in the corner of the samples was 0.3 cm, while the bigger hole in the center of the samples used for CCT was 0.7 cm.

(a) Sample used for recording polarisation curves and Mott-Schottky analysis.

(b) Sample used for testing critical crevice corrosion temperature.

Figure 3.1: The two different samples types provided by Framo. UNS S32750 and UNS S31254 were supplied in both types.

3.2 Electrochemical measurements

Electrolyte

The electrolyte used in all experiments was a 3.5 % NaCl solution. The solution was made by dissolving 70 g of NaCl in 2 L of distilled water. The resulting electrolyte had a pH of 6.5.

Reference electrode

An Ag/AgCl electrode in saturated KCl was used as reference electrode for all experiments.

3.2.1 Hydrogen charging

The hydrogen was introduced to the samples by cathodic polarisation at fixed current densities at room temperature using a three-electrode array connected to a Gamry Interface 1000 potentiostat. A platinum mesh served as the counter electrode (CE), while the stainless steel samples served as working electrode (WE). The reference electrode (RE) was the aforementioned Ag/AgCl electrode in saturated KCl. The CE worked as anode, while the stainless steel samples worked as cathode, thereby being site for the hydrogen evolution re-

action shown in reaction 2.6. Higher hydrogen concentrations in the material were obtained by using higher HCCDs. During hydrogen charging the electrolyte pH increased to 8.5, rendering the electrolyte used for charging unusable for further experiments.

Samples that were not charged with hydrogen were instead exposed at open circuit potential (OCP) to the electrolyte for a 24 hour period before being used in experiments.

3.2.2 Anodic polarisation curves

Table 3.2 shows the test matrix used to investigate the effect of different charge current densities on the corrosion resistance of UNS S32750, while Table 3.3, 3.4, 3.5 and 3.6 show the test matrices used to investigate the effect of different storage periods on the corrosion resistance of the stainless steel. The anodic polarisation curves were recorded using a Gamry Interface 1000 potentiostat.

To introduce hydrogen into the samples, hydrogen charging was performed according to the description provided in section 3.2.1. After changing the electrolyte, the samples were immersed once more and left for one hour to stabilise the OCP. While stabilising the OCP, oxygen was simultaneously purged from the electrolyte by bubbling with high purity nitrogen gas. Once the OCP had stabilised, anodic polarisation curves were recorded using the same three-electrode array described in section 3.2.1. The samples were polarised in the anodic direction from a potential of -0.1 V versus the OCP, with a scan rate of 0.167 mV/s. Polarisation was stopped after reaching the pitting potential (E_{pit}). The anodic polarisation curves of selected samples were recorded at 60 ℃, the rest were recorded at room temperature.

A simple illustration of the setup can be seen in Figure 3.2.

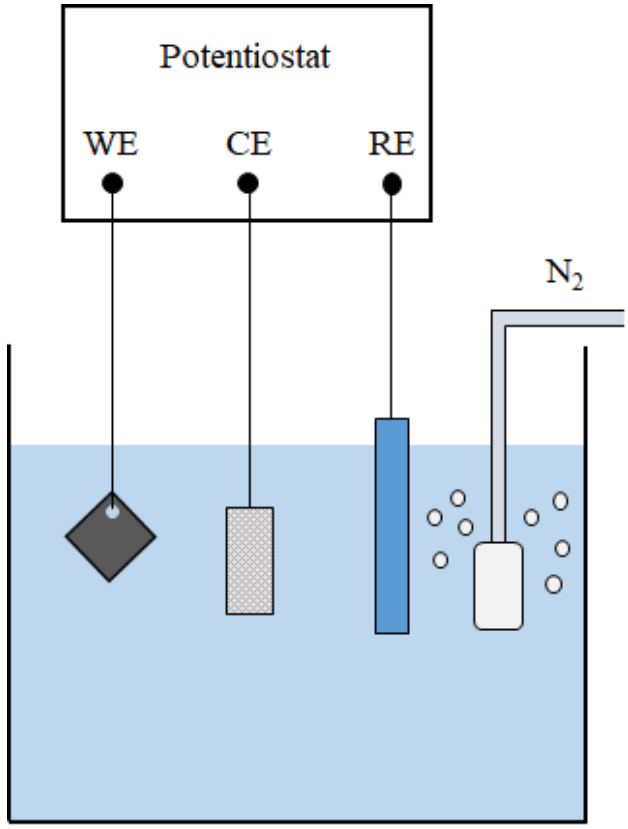

Figure 3.2: Schematic illustration of the experimental setup used to document the effect of hydrogen on the corrosion resistance.

Table 3.2: Test matrix used for investigating the effect of different hydrogen charge current densities on the corrosion properties of UNS S32750 samples at both room temperature and 60 °C [4].

HCCD [mA/cm^2]	**Charge duration [h]**
Uncharged	N/A
-0.5	24
-1	24
-10	24

Table 3.3: Test matrix used for investigating the effect of different storage periods in air after polarisation on the corrosion properties of UNS S32750 samples at room temperature.

HCCD [mA/cm^2]	Charge duration [h]	Storage time [days]
Uncharged	N/A	No
-0.1	24	No
-0.1	24	1
-0.1	24	7
-0.1	24	30
-0.1	168	No
-10	24	No

Table 3.4: Test matrix used for investigating the effect of different storage periods in air after polarisation on the corrosion properties of UNS S32750 samples at 60 ℃.

HCCD [mA/cm^2]	Charge duration [h]	Storage time [days]
Uncharged	N/A	No
-0.1	24	No
-0.1	24	1
-0.1	24	7
-0.1	24	30

Table 3.5: Test matrix used for investigating the effect of different storage periods in air after polarisation on the corrosion properties of welded UNS S32750 samples at room temperature.

HCCD [mA/cm^2]	Charge duration [h]	Storage time [days]
Uncharged	N/A	No
-0.1	24	No
-0.1	24	7
-0.1	24	30

Table 3.6: Test matrix used for investigating the effect of different storage periods in air after polarisation on the corrosion properties of UNS S31254 samples at room temperature.

HCCD [mA/cm^2]	Charge duration [h]	Storage time [days]
Uncharged	N/A	No
-0.1	24	No
-0.1	24	7

3.2.3 Critical crevice corrosion temperature (CCT)

Table 3.7 shows the test matrix used to investigate the effect of different HCCDs on the CCT of the stainless steel, while Table 3.8, 3.9 and 3.10 show the test matrices used to investigate the effect that different storage periods after hydrogen charging had on the CCT of the stainless steel. The samples were tested in pairs to ensure reproducibility.

Beakers with 3.5 % NaCl electrolyte were heated by a water bath to the starting temperature of 25 ℃. After hydrogen charging, the samples were cleaned with distilled water before being mounted in spring loaded assemblies as described by ISO 18070 [50], using a torque of 2 Nm. Figure 3.3 shows a sample mounted in the assembly. After the samples were mounted in the crevice formers, they were immersed in the electrolyte in the beakers. Approximately 10 minutes passed from the cathodic polarisation was finished until the samples were mounted and immersed in the electrolyte in the beakers. The samples were then left for an hour to stabilise OCP. An important difference is that samples from batch 1 of UNS S32750 was not left to stabilise OCP after immersion in the beakers. After immersion, the samples were then polarised to a constant applied potential, E_{app}, of 600 $\text{mV}_{\text{Ag/AgCl}}$ during the experiment using a potentiostat. This was done to simulate the potential reached in chlorinated seawater [8]. The temperature in the water bath, and thereby the beakers containing the samples, was then increased by 4 ℃/day. The recorded potential drop, ΔE, over the resistance was used to calculate the current from the samples through Ohm's law;

$$I = \frac{\Delta E}{R}. \tag{3.1}$$

The objective was to select a resistor which gave a maximum potential drop of 2 mV to maintain the potential on the sample at approximately 600 $mV_{Ag/AgCl}$. The current density was then found by dividing the current with the sample area. The CCT was determined as the temperature where the current density reached stable values above 0.1 mA/cm^2, according to ASTM G150 [51]. Confirmation of the initiation of crevice corrosion was also done visually by observation of brown corrosion products around the crevice.

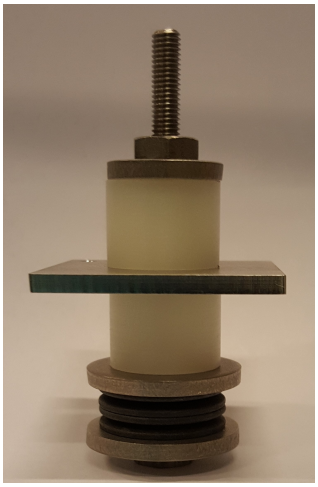

Figure 3.3: Spring loaded assembly with sample used for finding CCT [50].

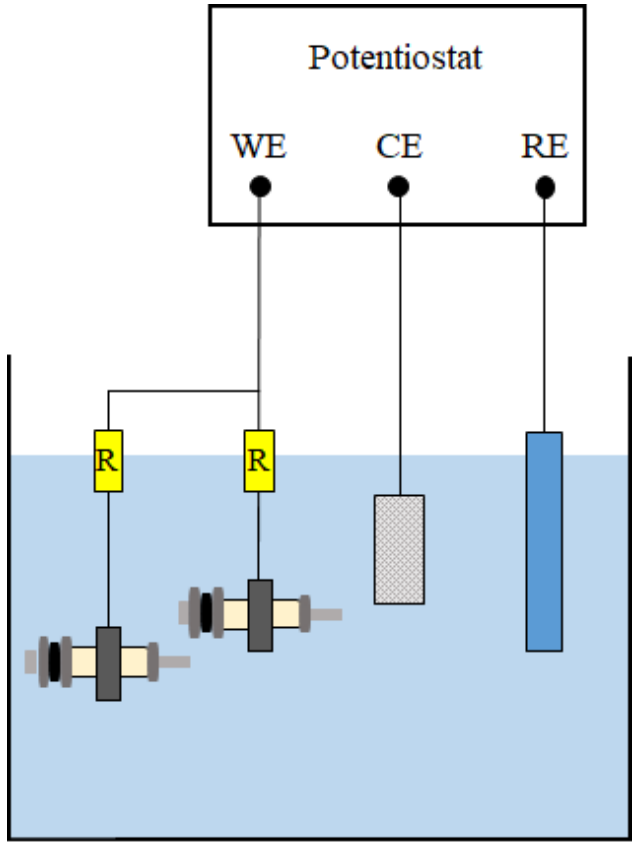

Figure 3.4: Schematic illustration of the setup used to determine CCT.

Table 3.7: Test matrix used for investigating the effect of different hydrogen charge current densities on the CCT of UNS S32750. Two samples were tested for each HCCD [4].

HCCD [mA/cm^2]	Charge duration [h]
Uncharged	N/A
-0.1	24
-1	24
-10	24
-10	192

Table 3.8: Test matrix used for investigating the effect of different storage periods in air after polarisation on the CCT of UNS S32750. Two samples were tested for each different storage period used, with the exception of the uncharged sample.

HCCD [mA/cm^2]	Charge duration [h]	Storage time [days]
Uncharged	N/A	No
-0.1	24	No
-0.1	24	1
-0.1	24	7
-0.1	24	30
-0.1	168	No
-10	24	No

Table 3.9: Test matrix for used for investigating the effect of different storage periods in air after polarisation on the CCT of welded samples of UNS S32750. Two samples were tested for each storage period used.

HCCD [mA/cm^2]	Charge duration [h]	Storage time [days]
Uncharged	N/A	No
-0.1	24	7

Table 3.10: Test matrix used for investigating the effect of different storage periods in air after polarisation on the CCT of UNS S31254. Two samples were tested for each storage period used.

HCCD [mA/cm^2]	Charge duration [h]	Storage time [days]
Uncharged	N/A	No
-0.1	24	No
-0.1	24	7

3.3 Surface characterisation

XPS analysis

Samples from batch 2 of UNS S37520 used for XPS analysis were cut into smaller pieces, roughly 6 mm × 4 mm × 2.5 mm. The surface to be examined was wet abraded with SiC-paper of 220, 550, 1000 and 2000 grit, then polished with 3 µm diamond paste. The sample pieces were further cleaned with acetone and distilled water in an ultrasonic bath. Four sets of samples were then prepared according to Table 3.11.

A Kratos Axis Ultra DLD machine with a monochromatic Al Kα source (12 mA, 12 kV) was used for the XPS analysis. The pressure in the chamber was $2 \cdot 10^{-9}$ torr. Depth profiles of each sample were obtained by sputtering with an argon ion gun. CasaXPS software was used for curvefitting, and Shirley background subtraction was used for all quantifications and evaluations of the data obtained [52]. Full width half maximum was kept constant for oxide components of each element, peak area ratio of the Mo doublets were kept constant, and Gaussian/Lorentzian asymmetry was used for curve fitting using the parameters of standard peaks.

Table 3.11: Test matrix used for XPS analysis of samples from batch 2 of UNS S37520.

HCCD [mA/cm²]	Charge duration [h]	Storage time [days]
Uncharged	N/A	No
-0.1	24	No
-10	24	No
-0.1	24	7

SEM and EDS

A Quanta FEG 650 SEM was used to study the surface of a sample used for determination of CCT after the end of the experiment. The sample in question was charged with a HCCD of -10 mA/cm^2. The SEM investigation was performed in order to determine if selective corrosion occurred in either α of γ. EDS was performed to determine the chemical composition

of the areas where corrosion occurred, and to calculate the corresponding PREN values.

Mott-Schottky analysis

Table 3.12 shows the test matrix used to investigate the semiconductor behaviour of the passive film formed on samples from batch 2 of UNS S32750. The same potentiostat used for hydrogen charging and to record anodic polarisation curves was also used for the Mott-Schottky analysis. A film formation potential, E_{f}, was selected based on the polarisation curves of the corresponding prerequisites. The samples were then polarised at the selected potential for 4 hours, before Mott-Schottky analysis was started. This was done by sweeping from the E_{f} in the negative direction with a voltage step of 5 mV. A frequency of 1 kHz and a peak-to-peak amplitude of 10 mV root mean square (RMS) was used in the experiments.

The density of defects in the passive film was then found from the slope of the linear parts of the Mott-Schottky plots.

Table 3.12: Test matrix used for Mott-Schottky analysis of samples from batch 2 of UNS S37520. The samples were not stored between hydrogen charging and the experiment.

HCCD [mA/cm^2]	**Charge duration [h]**	**E_f [mV$_{Ag/AgCl}$]**
Uncharged	N/A	650
-0.1	24	800
-10	24	800

4 Results

As E_{corr} and OCP are typically used interchangeably for the same value, E_{corr} will be used when addressing this value for the rest of this thesis.

4.1 Anodic polarisation curves

4.1.1 Effect of different hydrogen charge current densities

Figure 4.1 shows the anodic polarisation curves for samples from batch 1 of UNS S32750 charged with different HCCDs recorded at room temperature. As can be seen from the figure there is a clear drop in E_{corr} from around -0.1 $V_{\text{Ag/AgCl}}$ for the uncharged sample to approximately -0.7 $V_{\text{Ag/AgCl}}$ for the charged samples. E_{pit} (might also be an oxygen reaction) for all samples, independent of charge current density, is equal to 1 $V_{\text{Ag/AgCl}}$. With increasing hydrogen charge current densities, a clear increase in the recorded corrosion current densities (i_{corr}) from approximately 10^{-8} mA/cm^2 to 10^{-6} mA/cm^2 is observed, as well as an increase in the anodic current densities.

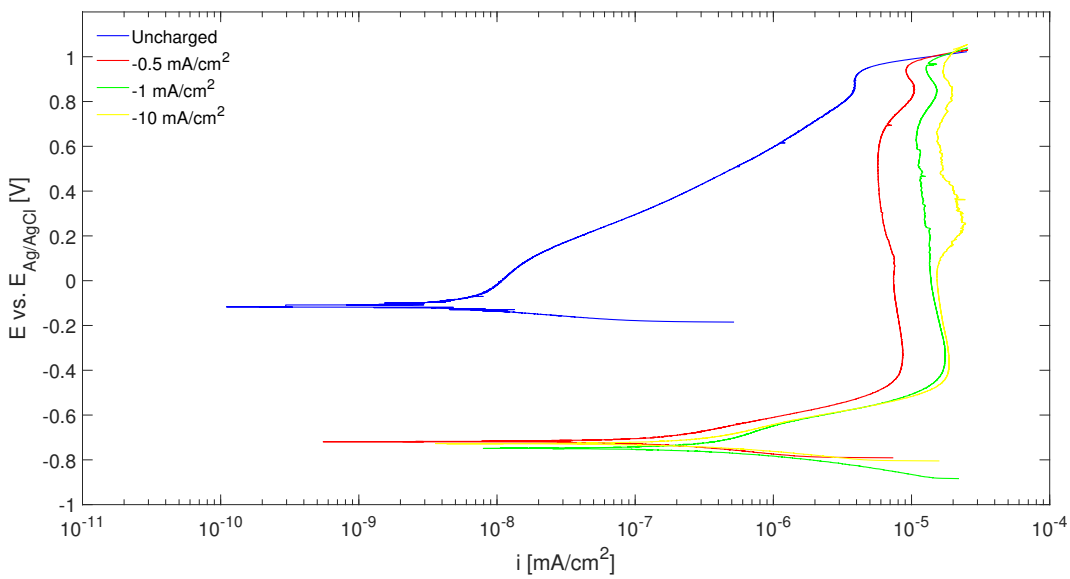

Figure 4.1: Anodic polarisation curves for UNS S32750 samples recorded at room temperature for different hydrogen charge current densities, according to Table 3.2 [4].

Figure 4.2 shows the anodic polarisation curves for samples from batch 1 of UNS S32750 charged with different HCCDs recorded at 60 ℃. E_{corr} drops from around -0.25 $V_{Ag/AgCl}$ to -0.7 $V_{Ag/AgCl}$ going from the uncharged sample to the charged samples. E_{corr} for an uncharged sample is thus lower at 60 ℃ compared to room temperature, but the charged samples all stabilise at a potential similar to the charged samples at room temperature. i_{corr} increases from an uncharged sample to a charged sample, from $5 \cdot 10^{-8}$ mA/cm^2 to $3 \cdot 10^{-6}$ mA/cm^2. The magnitude of the increase is therefore similar to that at room temperature, but the values at 60 ℃ are higher. Similar as for room temperature, the anodic current densities increase with increasing HCCD. The pitting potential for uncharged and charged samples are different at 60 ℃, unlike that observed at room temperature. E_{pit} of the uncharged sample is 0.8 $V_{Ag/AgCl}$, and charged samples show values around 0.4 $V_{Ag/AgCl}$. This indicates that increasing temperature decreases E_{pit} for both uncharged and charged samples and increases the difference in E_{pit} between uncharged and charged samples.

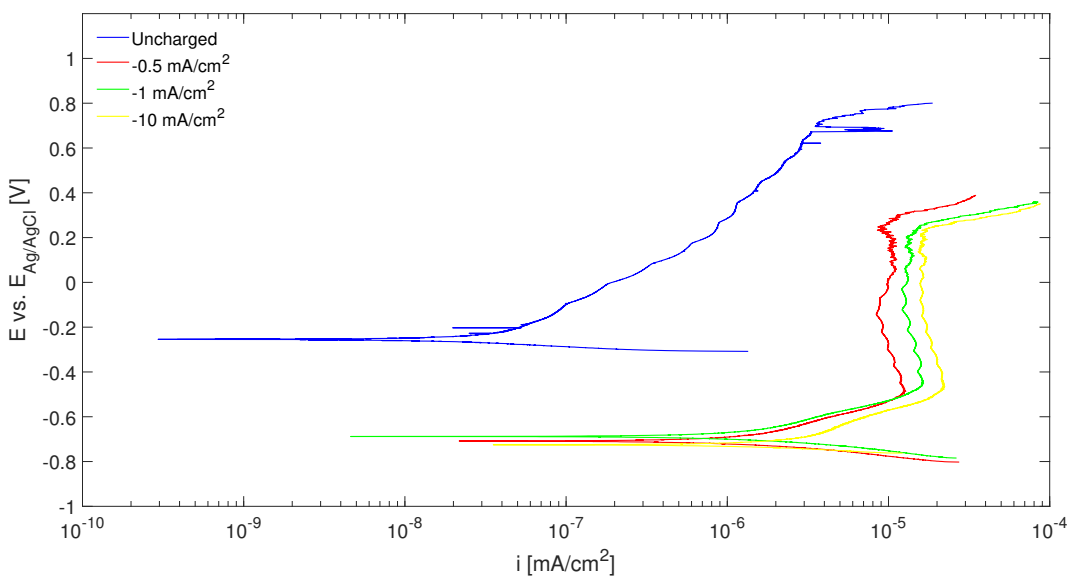

Figure 4.2: Anodic polarisation curves for UNS S32750 samples recorded at 60 ℃ for different hydrogen charge current densities, according to Table 3.2 [4].

4.1.2 Effect of storage time

Figure 4.3 shows the anodic polarisation curves for samples from batch 2 of UNS S32750 with different periods of storage time recorded at room temperature. A drop in E_{corr} is observed for all samples that have been charged, however, E_{corr} is also observed to increase towards more positive values with increasing storage time. E_{corr} for the charged sample with no storage after hydrogen charging exhibits a E_{corr} of around -0.7 $V_{\text{Ag/AgCl}}$ while the sample stored for 30 days after hydrogen charging exhibits a E_{corr} of around -0.55 $V_{\text{Ag/AgCl}}$. A decrease in i_{corr} and anodic current densities is observed with longer storage. E_{pit} stabilises around 1 $V_{\text{Ag/AgCl}}$ for all samples independently of hydrogen charge current density and storage time.

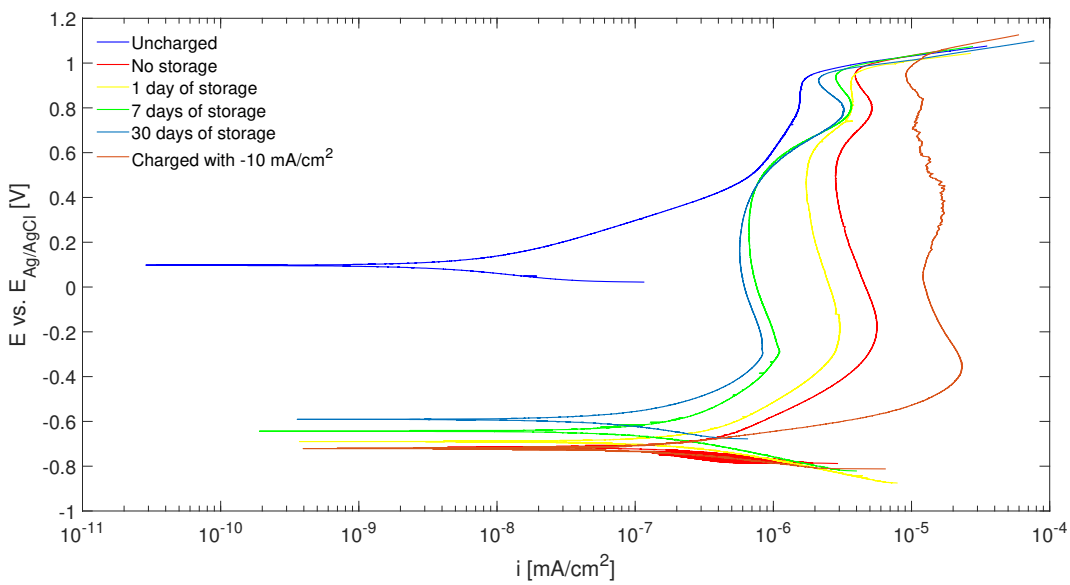

Figure 4.3: Anodic polarisation curves for samples from batch 2 of UNS S32750 samples recorded at room temperature for different periods of storage after hydrogen charging, according to Table 3.3.

Figure 4.4 shows the anodic polarisation curves for samples from batch 2 of UNS S32750 with different periods of storage recorded at 60 ℃. A similar drop in E_{corr} from the uncharged sample to the charged samples observed at room temperature is also found at 60 ℃. E_{corr} for the uncharged sample at 60 ℃ is approximately 0.45 $V_{\text{Ag/AgCl}}$ lower than E_{corr} for the uncharged sample at room temperature. Similar to the observations made at room temperature, E_{corr} increases with increasing storage time also at 60 ℃. However, the difference between the sample with no storage time after hydrogen charging and the sample stored for 30 days is smaller than at room temperature. i_{corr} and the anodic current densities exhibits the same decrease as the room temperature samples with increasing storage, but the difference is smaller than the one at room temperature. E_{pit} stabilises around 1 $V_{\text{Ag/AgCl}}$ for the samples at 60 ℃, similar to that observed at room temperature.

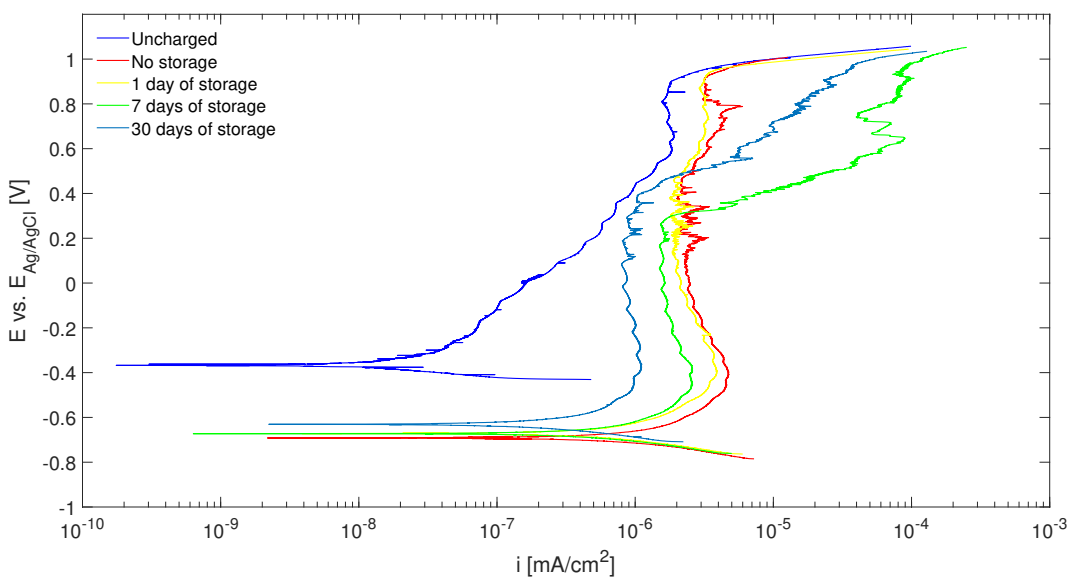

Figure 4.4: Anodic polarisation curves for UNS S32750 samples recorded at 60 ℃ for different periods of storage after hydrogen charging, according to Table 3.4.

Figure 4.5 shows the anodic polarisation curves recorded at room temperature for the welded samples of UNS S32750. The welded samples exhibit a drop in E_{corr} from around 0.05 $V_{Ag/AgCl}$ for the uncharged sample to -0.7 $V_{Ag/AgCl}$ for the charged sample without storage after hydrogen charging. E_{corr} also jumps from -0.7 $V_{Ag/AgCl}$ for the charged sample without storage time to -0.6 $V_{Ag/AgCl}$ for the sample that was stored for 7 days after hydrogen charging. As figure 4.5 shows, anodic current densities exhibit a wide range of values, from 10^{-9} mA/cm^2 for the uncharged sample to 10^{-5} mA/cm^2 for the sample with no storage time after hydrogen charging. E_{pit} stabilises at approximately 0.6 $V_{Ag/AgCl}$ for all samples.

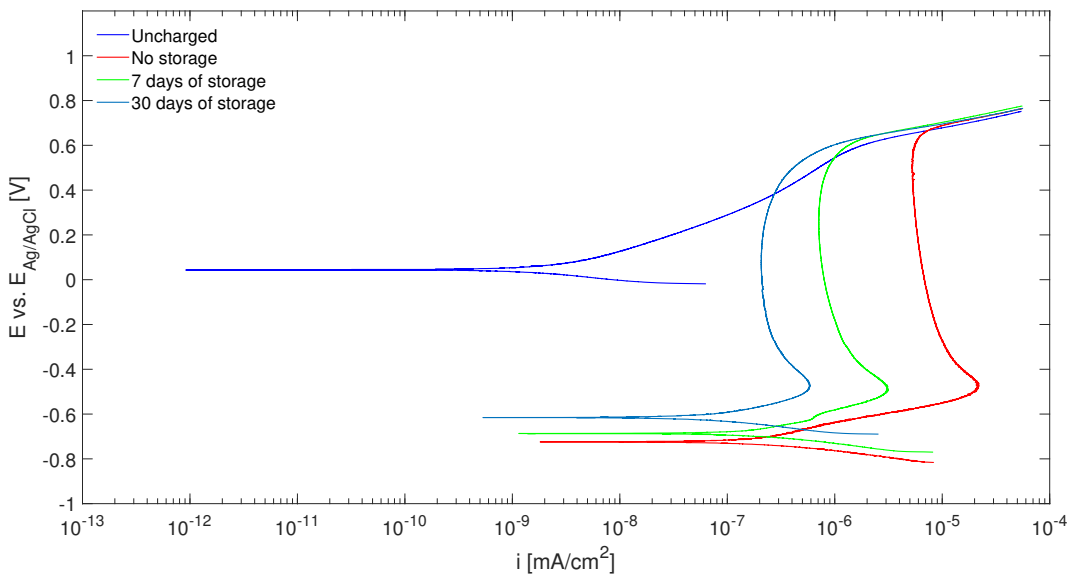

Figure 4.5: Anodic polarisation curves for welded UNS S32750 samples recorded at room temperature for different periods of storage after hydrogen charging, according to Table 3.5.

Figure 4.6 shows the anodic polarisation curves recorded for UNS S31254 samples at room temperature. E_{corr} for the uncharged sample is 0.1 $V_{\text{Ag/AgCl}}$. A drop in E_{corr} of approximately 0.8 V to -0.7 $V_{\text{Ag/AgCl}}$ is observed for the charged sample without storage after hydrogen charging. A difference of 0.1 V in E_{corr} is observed when comparing the sample with and without storage after hydrogen charging. There is also a difference in anodic current densities between the two samples, with the stored sample exhibiting the lowest values. E_{pit} stabilises at 1 $V_{\text{Ag/AgCl}}$ for all samples.

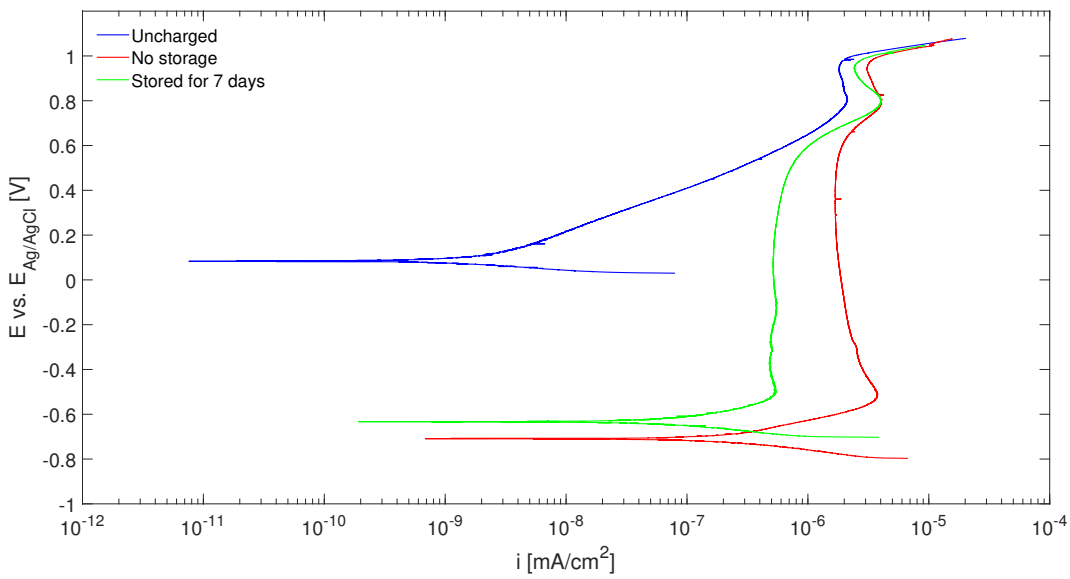

Figure 4.6: Anodic polarisation curves for UNS S31254 samples recorded at room temperature for different periods of storage after hydrogen charging, according to Table 3.6.

Table 4.1: Summary of some critical parameters from the anodic polarisation curves recorded in this work. The test conditions are presented in the following sequence; HCCD, charge duration and storage time. Passive current density for uncharged samples are presented as a range, as a clear passive current density is difficult to determine for these samples. All potentials given are versus the Ag/AgCl electrode in saturated KCl.

Steel grade	**Test conditions**	$E_{\mathbf{corr}}$ **[V]**	$i_{\mathbf{pass}}$ **[mA/cm^2]**	$E_{\mathbf{pit}}$ **[V]**
Batch 1 of UNS S32750, at RT	Uncharged	-0.1	$1 \cdot 10^{-8}$ - $4 \cdot 10^{-6}$	1
	-0.5 mA/cm^2, 24 h	-0.7	$5.5 \cdot 10^{-6}$	1
	-1 mA/cm^2, 24 h	-0.7	$1 \cdot 10^{-5}$	1
	-10 mA/cm^2, 24 h	-0.7	$1.5 \cdot 10^{-5}$	1
Batch 1 of UNS S32750, at 60 °C	Uncharged	-0.25	$4 \cdot 10^{-8}$ - $3 \cdot 10^{-6}$	0.8
	-0.5 mA/cm^2, 24 h	-0.7	$8 \cdot 10^{-6}$	0.4
	-1 mA/cm^2, 24 h	-0.7	$1.3 \cdot 10^{-5}$	0.4
	-10 mA/cm^2, 24 h	-0.7	$1.6 \cdot 10^{-5}$	0.4
Batch 2 of UNS S32750, at RT	Uncharged	0.1	$1 \cdot 10^{-8}$ - $1.5 \cdot 10^{-6}$	1
	-0.1 mA/cm^2, 24 h, no storage	-0.7	$2 \cdot 10^{-6}$	1
	-0.1 mA/cm^2, 24 h, 1 day of storage	-0.69	$1.7 \cdot 10^{-6}$	1
	-0.1 mA/cm^2, 24 h, 7 days of storage	-0.65	$6.5 \cdot 10^{-7}$	1
	-0.1 mA/cm^2, 24 h, 30 days of storage	-0.6	$5.5 \cdot 10^{-7}$	1
	-10 mA/cm^2, 24 h, no storage	-0.7	$1.3 \cdot 10^{-5}$	1
Batch 2 of UNS S32750, at 60 °C	Uncharged	-0.3	$2 \cdot 10^{-8}$ - $1.6 \cdot 10^{-6}$	1
	-0.1 mA/cm^2, 24 h, no storage	-0.7	$2.4 \cdot 10^{-6}$	1
	-0.1 mA/cm^2, 24 h, 1 day of storage	-0.7	$1.9 \cdot 10^{-6}$	1
	-0.1 mA/cm^2, 24 h, 7 days of storage	-0.65	$1.5 \cdot 10^{-6}$	1
	-0.1 mA/cm^2, 24 h, 30 days of storage	-0.6	$8 \cdot 10^{-7}$	1
Welded UNS S32750	Uncharged	0.05	$3 \cdot 10^{-9}$ - $1 \cdot 10^{-6}$	0.6
	-0.1 mA/cm^2, 24 h, no storage	-0.7	$5 \cdot 10^{-6}$	0.6
	-0.1 mA/cm^2, 24 h, 7 days of storage	-0.66	$7 \cdot 10^{-7}$	0.6
	-0.1 mA/cm^2, 24 h, 30 days of storage	-0.6	$1 \cdot 10^{-7}$	0.6
UNS S31254	Uncharged	0.1	$2 \cdot 10^{-9}$ - $2 \cdot 10^{-6}$	1
	-0.1 mA/cm^2, 24 h, no storage	-0.7	$1.5 \cdot 10^{-6}$	1
	-0.1 mA/cm^2, 24 h, 7 days of storage	-0.65	$5 \cdot 10^{-7}$	1

4.2 Critical crevice corrosion temperatures

In section 4.2.1 and 4.2.2 current densities are presented as a function of time and temperature. Based on the definition of the CCT provided in ASTM G150 and the recorded current densities, the CCTs of the different samples were determined. They are presented in Table 4.2, 4.4, 4.3 and 4.5. The difference in CCT between the uncharged samples and the charged samples is also given in the same tables, labeled as ΔT. If the two uncharged samples exhibit different CCTs, the highest temperature is chosen as reference.

4.2.1 Effect of different hydrogen charge current densities

Figure 4.7 shows the recorded current densities for two uncharged UNS S32750 samples from batch 1. The current density for sample 1 reached a stable value above 0.1 mA/cm^2 at 52 ℃, while sample 2 reached a stable value at 56 ℃.

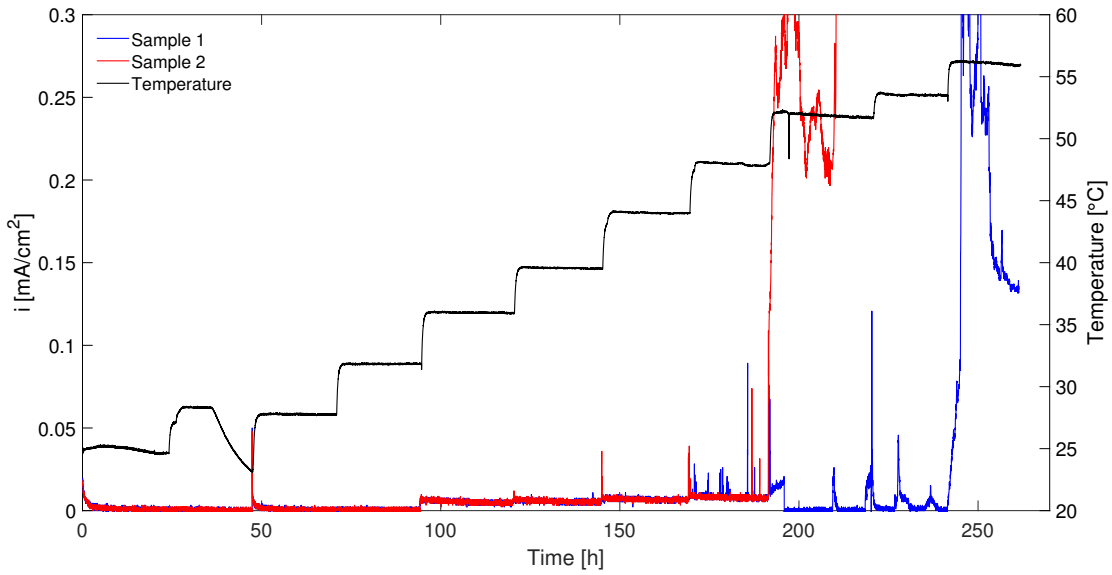

Figure 4.7: Recorded current densities for two uncharged UNS S32750 samples from batch 1, according to Table 3.7 [4].

Figure 4.8 shows the recorded current densities for two UNS S32750 samples from batch 1 charged with hydrogen using a HCCD of -0.1 mA/cm^2. Both samples exhibit current densities above 0.1 mA/cm^2 already at 25 ℃. The current density for sample 1 was higher than for sample 2 over the whole duration of the experiment.

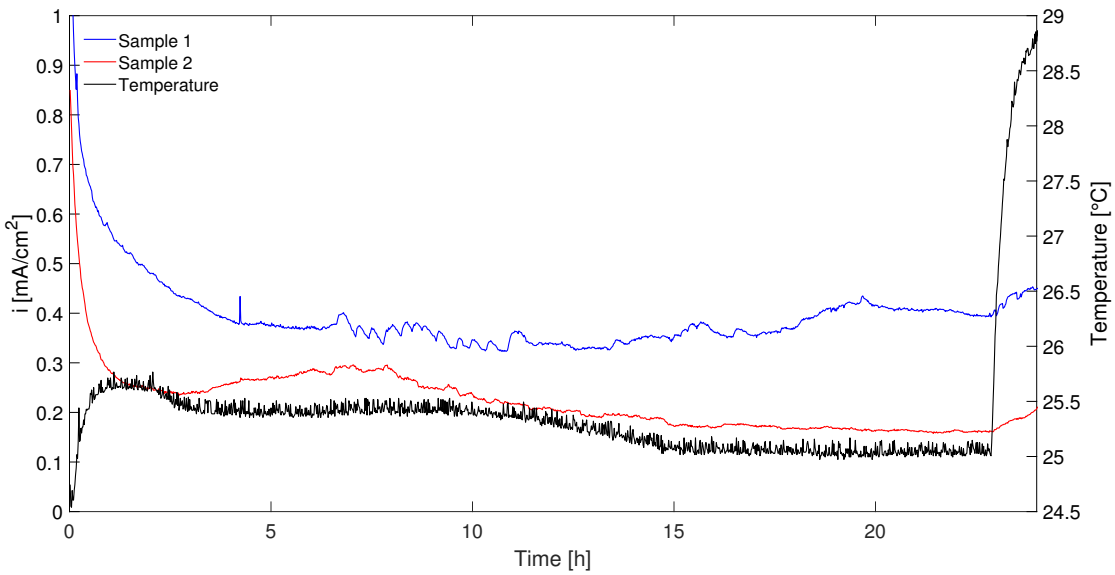

Figure 4.8: Recorded current densities for two UNS S32750 samples from batch 1 charged with hydrogen using a HCCD of -0.1 mA/cm^2, according to Table 3.7 [4].

Figure 4.9 shows the recorded current densities for two UNS S32750 samples from batch 1 charged with hydrogen using a HCCD of -1 mA/cm^2. Both samples show initiation of crevice corrosion from the start at 25 °C, with current densities above 0.1 mA/cm^2. Sample 2 exhibits a current density higher than sample 1 for approximately 7.5 hours, after which sample 1 has a higher current density.

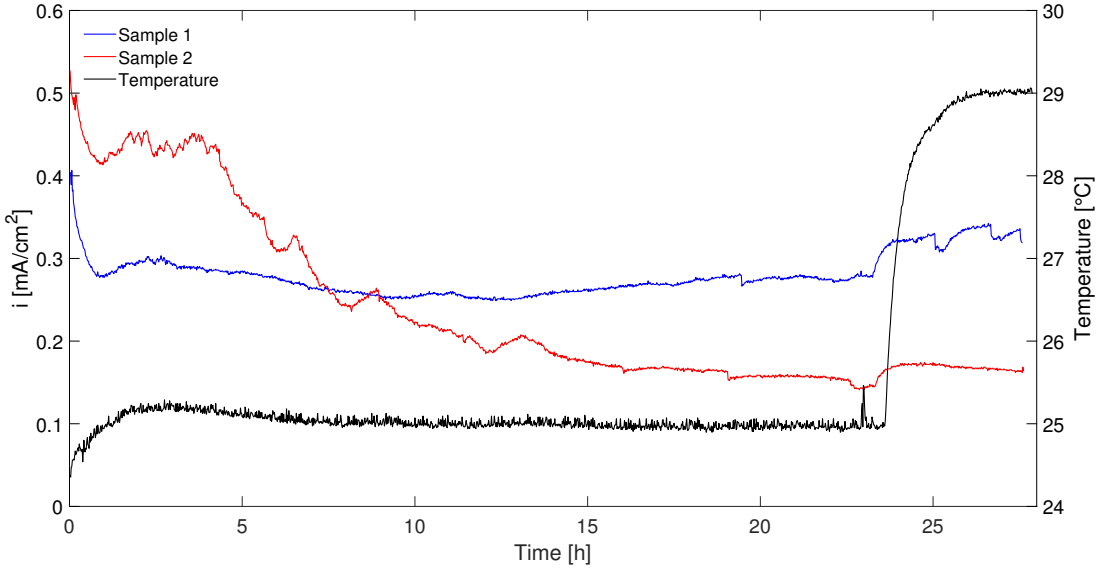

Figure 4.9: Recorded current densities for two UNS S32750 samples from batch 1 charged with hydrogen using a HCCD of -1 mA/cm^2, according to Table 3.7 [4].

Figure 4.10 shows the recorded current densities for two UNS S32750 samples from batch 1 charged with hydrogen using a HCCD of -10 mA/cm^2. Sample 2 shows stable current density values above 0.1 mA/cm^2 from 25 ℃ until the end of the experiment. Sample 1 on the other hand, exhibits current density lower than 0.1 mA/cm^2 until initiation of crevice corrosion after almost 120 hours at 36 ℃, where the current jumps to values above 0.1 mA/cm^2.

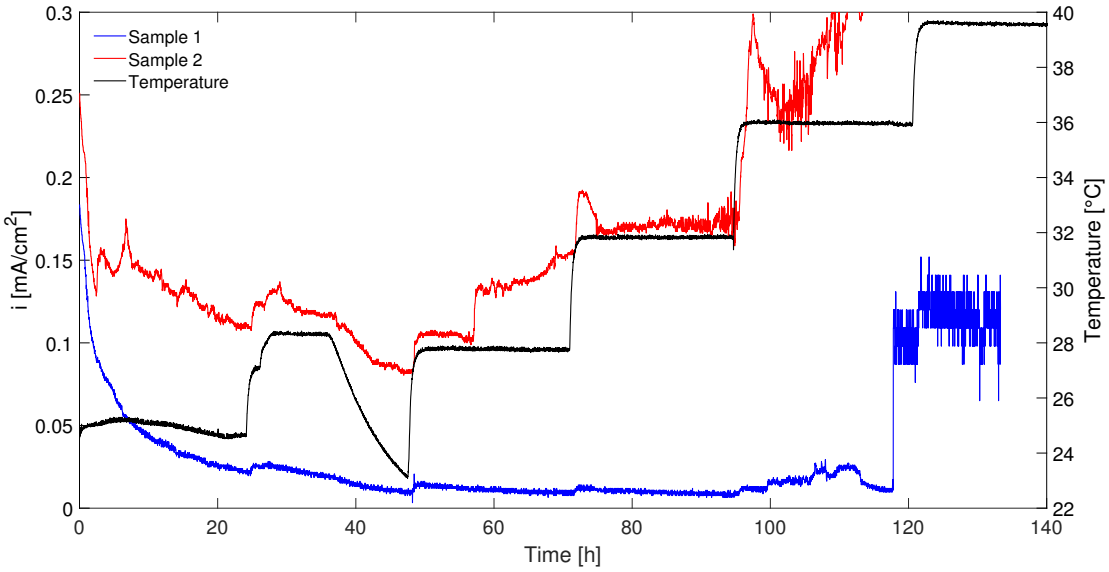

Figure 4.10: Recorded current densities for two UNS S32750 samples form batch 1 charged with hydrogen using a HCCD of -10 mA/cm^2, according to Table 3.7 [4].

Figure 4.11 shows the recorded current densities for two UNS S32750 samples from batch 1 charged with hydrogen using a HCCD of -10 mA/cm^2 over an 8 day period. Both samples exhibit current densities above 0.1 mA/cm^2 at 25 ℃, though the current values are significantly higher than all the other samples tested. Sample 2 reached values close to 2 mA/cm^2 after 15 hours, while sample 1 showed values of 2.5 mA/cm^2 after only 7 hours.

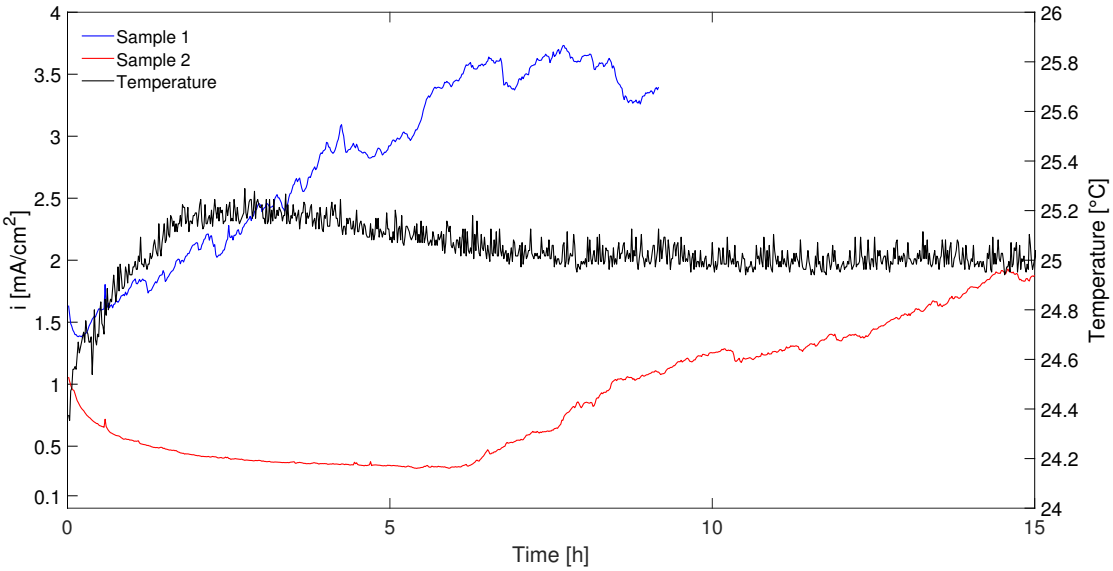

Figure 4.11: Recorded current densities for two UNS S32750 samples from batch 1 charged with hydrogen for 8 days using a HCCD of -10 mA/cm^2, according to Table 3.7 [4].

Based on the Figure 4.7 presented above and the given method of determining CCT, the CCTs for the samples tested are given in Table 4.2.

Table 4.2: The determined CCTs for UNS S32750 samples from batch 1 exposed to different HCCDs. ΔT is the temperature difference between the highest CCT of the uncharged samples and the CCT of the charged sample.

HCCD [mA/cm²]	**Charge duration [h]**	**Sample number**	**CCT [°C]**	**ΔT [°C]**
Uncharged	24	1	52	N/A
		2	56	N/A
-0.1	24	1	25	31
		2	25	31
-1	24	1	25	31
		2	25	31
-10	24	1	36	20
		2	25	31
-10	192	1	25	31
		2	25	31

4.2.2 Effect of storage time

Figure 4.12 shows the recorded current density for one uncharged UNS S32750 sample. The sample exhibits low current density until initiation of crevice corrosion at 66 ℃.

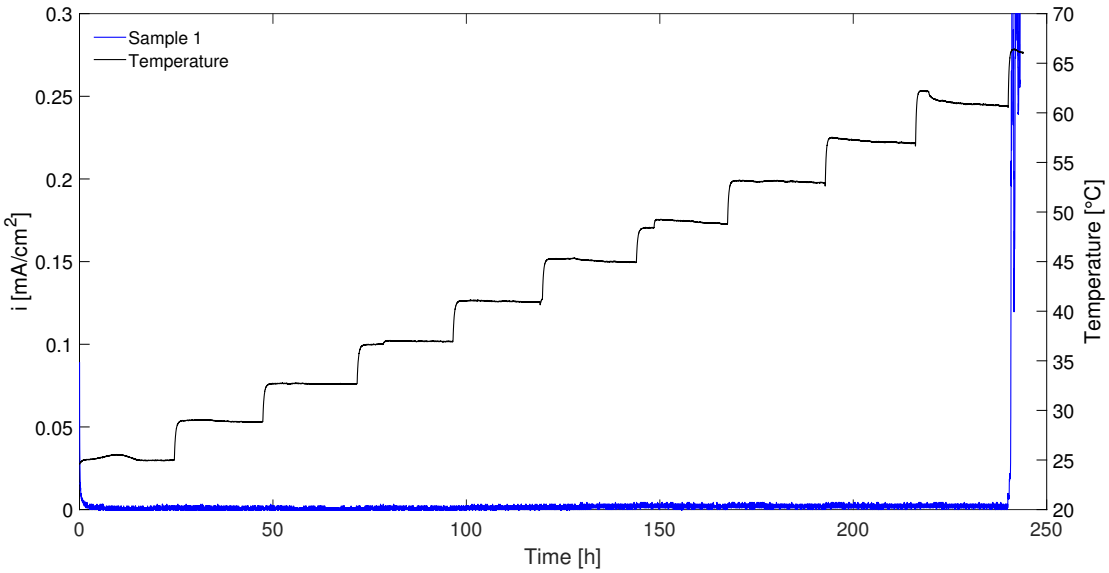

Figure 4.12: Recorded current densities for one uncharged UNS S32750 sample, according to Table 3.8.

Figure 4.13 shows the recorded current densities for two samples of UNS S32750 charged with a HCCD of -0.1 mA/cm^2, with no storage after hydrogen charging. Sample 1 exhibits an current density close to 0 mA/cm^2 until initiation at 37 ℃, while sample 2 exhibits a higher current density that increases steadily from 50 hours to around 80 hours and with crevice corrosion initiation at 37 ℃.

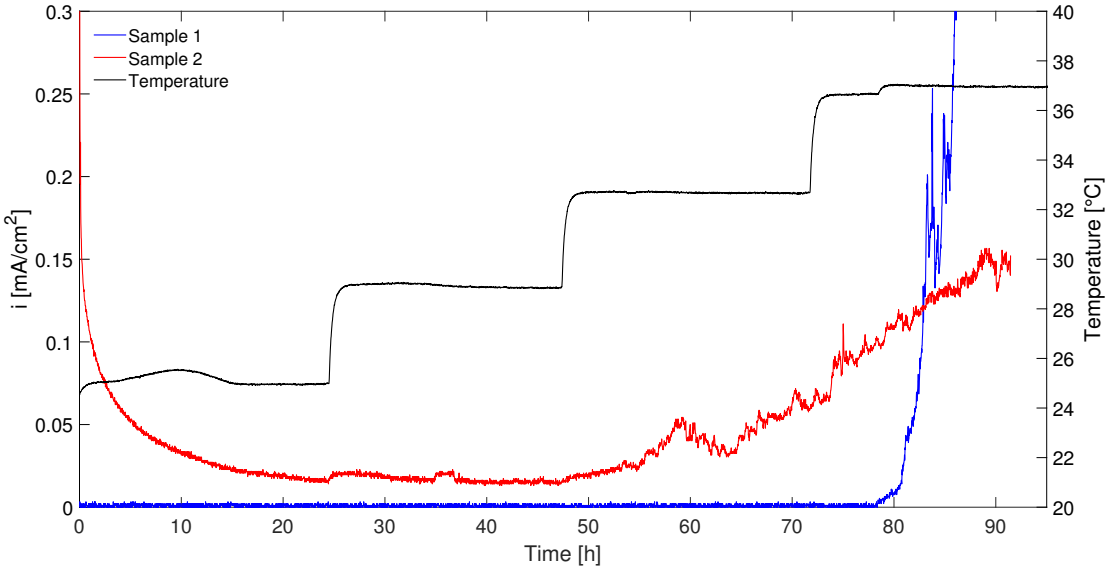

Figure 4.13: Recorded current densities for two UNS S32750 samples charged with hydrogen using a HCCD of -0.1 mA/cm^2, with no storage after hydrogen charging, according to Table 3.8.

Figure 4.14 shows the recorded current densities for two UNS S32750 samples charged with a HCCD of -0.1 mA/cm^2, with 1 day of storage in air after hydrogen charging. Both samples show noise during the experiment, especially at the start. The water bath stopped working after 125 hours, as can be seen by the drop in temperature. The current densities of both samples steadily rose until the water bath was turned off. The temperature was therefore kept at 45 ℃ for an extra 24 hours. During the second period with the water bath temperature of 45 ℃, the current densities of both samples stabilise above 0.1 mA/cm^2, indicating initiation of crevice corrosion.

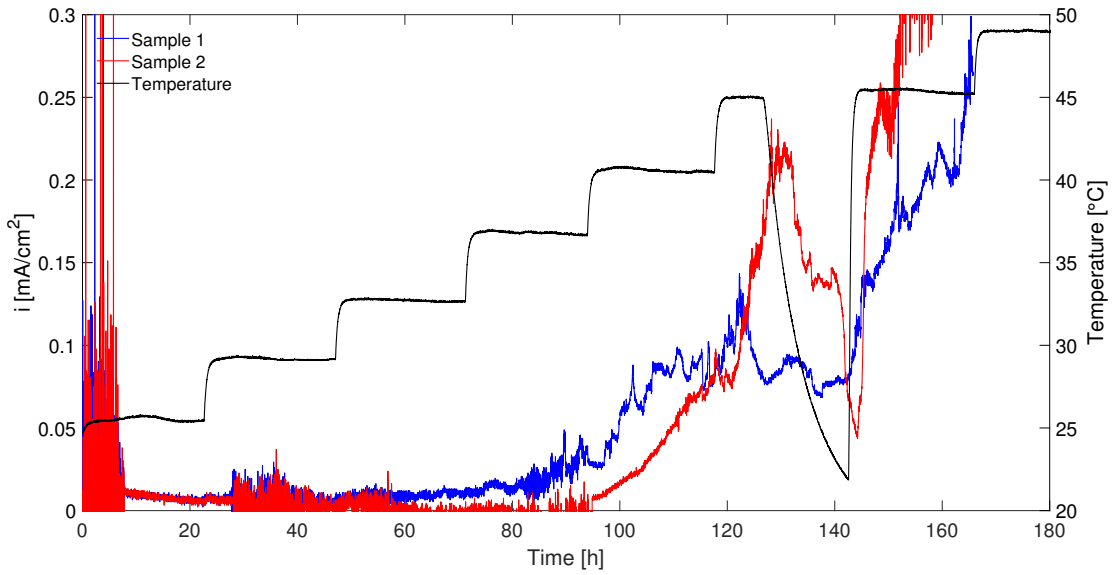

Figure 4.14: Recorded current densities for two UNS S32750 samples charged with hydrogen using a HCCD of -0.1 mA/cm^2, and stored in air for 1 day after hydrogen charging, according to Table 3.8.

Figure 4.15 shows the recorded current densities for two UNS S32750 samples charged with a HCCD of -0.1 mA/cm^2, with 7 days of storage in air after hydrogen charging. Both samples exhibit a spike in their respective current densities at 40 ℃, and sample 2 reaches a current density higher than 0.1 mA/cm^2 at this temperature. Sample 1, on the other hand, initiates crevice corrosion at 50 ℃.

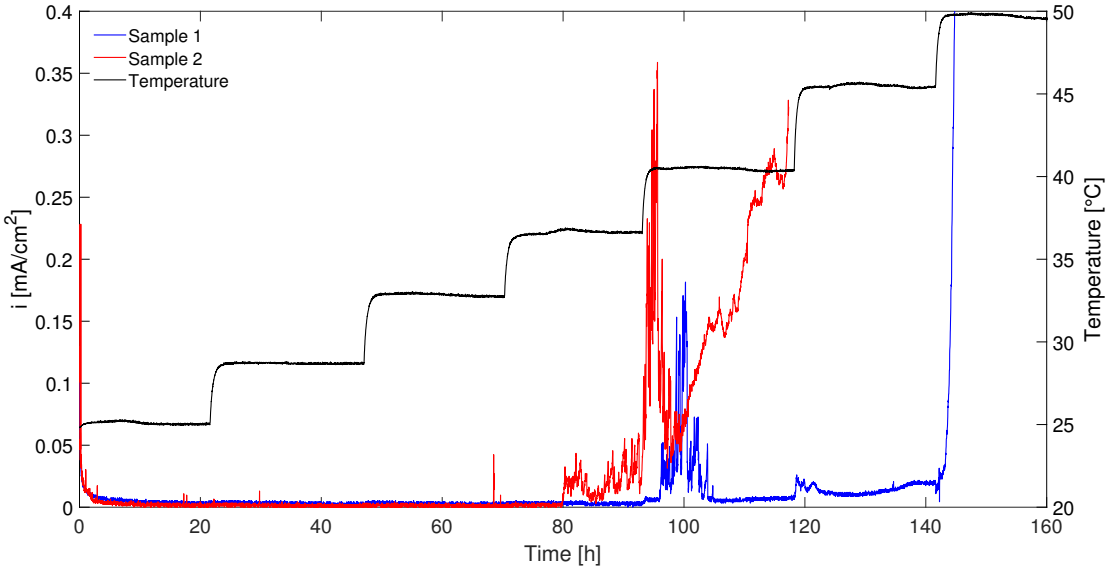

Figure 4.15: Recorded current densities for two UNS S32750 samples charged with hydrogen using a HCCD of -0.1 mA/cm^2, and stored in air for 7 days after hydrogen charging, according to Table 3.8.

Figure 4.16 shows the recorded current densities for two UNS S32750 samples charged with a HCCD of -0.1 mA/cm^2, with 30 days of storage in air after hydrogen charging. Both samples exhibit current densities close to 0 mA/cm^2 during the first 100 hours, followed by an increase until sample 1 initiates crevice corrosion at 41 ℃ and sample 2 initiates at 45 ℃.

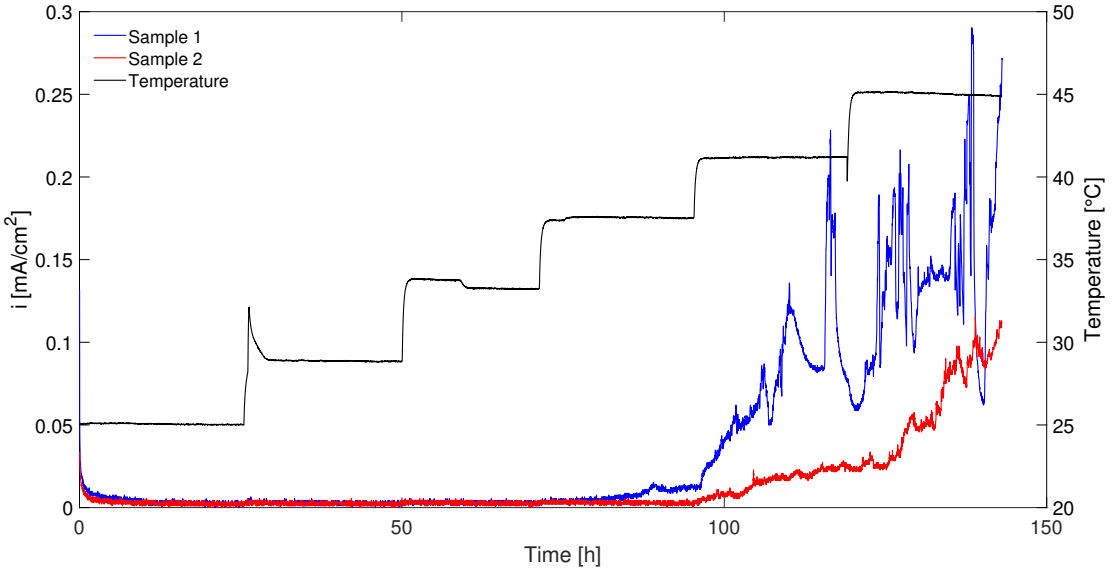

Figure 4.16: Recorded current densities for two UNS S32750 samples charged with hydrogen using a HCCD of -0.1 mA/cm^2, and stored in air for 30 days after hydrogen charging, according to Table 3.8.

Figure 4.17 shows the recorded current densities for two UNS S32750 samples charged with a HCCD of -0.1 mA/cm^2 over a period of 7 days, with no storage after hydrogen charging. The current density of sample 1 steadily decreases up until 120 hours, followed by a spike exceeding 0.1 mA/cm^2 indicating crevice corrosion initiation at 46 ℃. Sample 2 also shows a decrease in current density during the first 80 hours. However, after 80 and 100 hours, the current spikes and crevice corrosion initiates after 110 hours at 41 ℃.

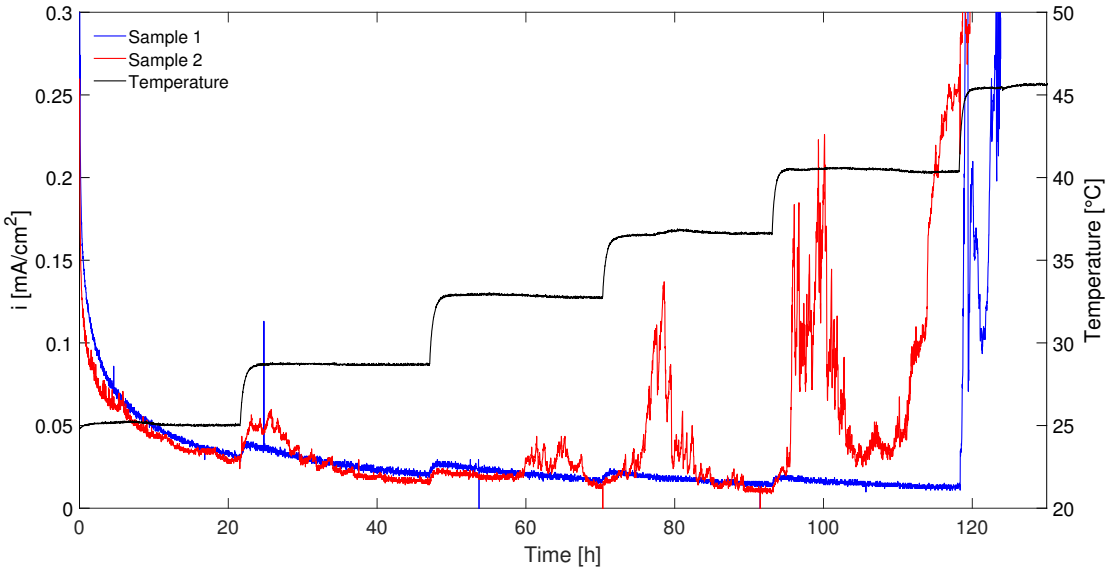

Figure 4.17: Recorded current densities for two UNS S32750 samples charged with hydrogen using a HCCD of -0.1 mA/cm^2 over a 7 days period, with no storage after hydrogen charging, according to Table 3.8.

Figure 4.18 shows the recorded current densities for two uncharged welded UNS S32750 samples. A jump in current density is observed for both samples following the increase in temperature. Both samples showed no signs of corrosion when the current densities reached values above 0.1 mA/cm^2, thus the experiment was extended beyond the usual limit for determining CCT. The experiment was ended when corrosion products were observed on the samples, which was at 57 ℃ for sample 2 and at 61 ℃ for sample 1.

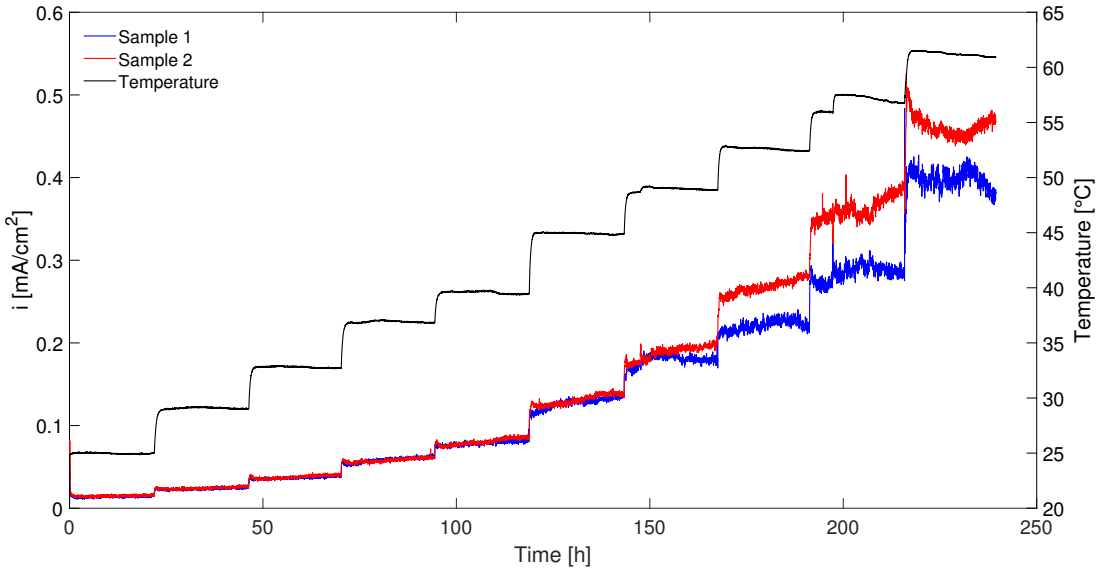

Figure 4.18: Recorded current densities for two uncharged welded UNS S32750 samples, according to Table 3.9.

Figure 4.19 shows the recorded current densities for two welded UNS S32750 samples charged with a HCCD of -0.1 mA/cm^2, with no storage after hydrogen charging. The same jump in current density is observed for these samples. Initiation of both samples happened when the temperature increased to 49 ℃.

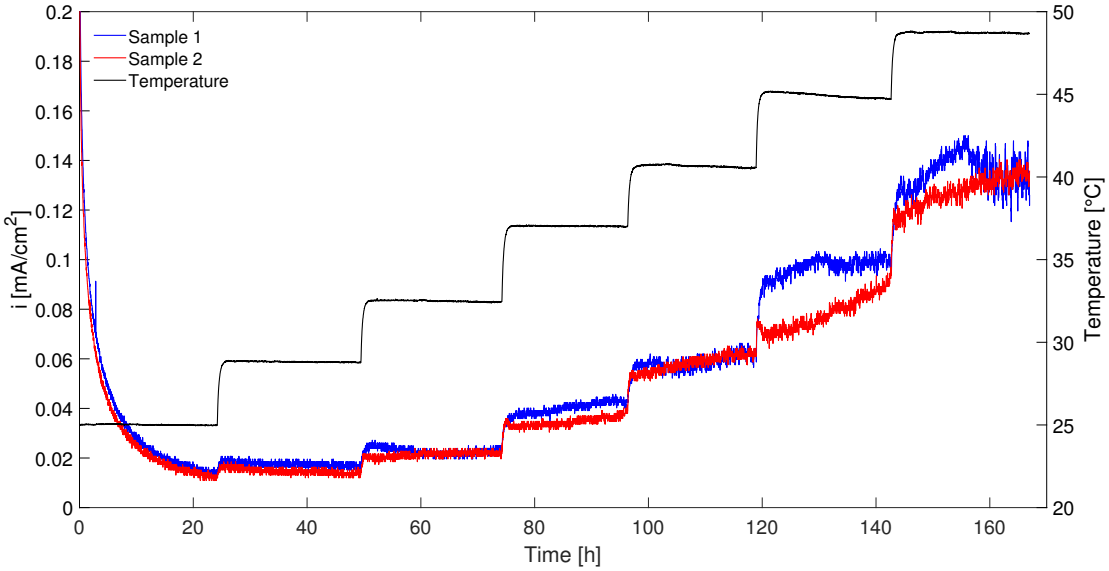

Figure 4.19: Recorded current densities for two welded UNS S32750 samples charged with a HCCD of -0.1 mA/cm^2, with no storage after hydrogen charging, according to Table 3.9.

Figure 4.20 shows the recorded current densities for two UNS S32750 samples charged with a HCCD of -10 mA/cm^2, with no storage after hydrogen charging. Both sample 1 and 2 show current densities around 0 mA/cm^2 until peaks occur after 120 h. Similar to that observed in figure 4.14, the water bath stopped working and the temperature was kept at 45 ℃ for an additional 24 hours. Sample 2 shows crevice corrosion initiation at 46 ℃, while samples 1 initiates at 49 ℃.

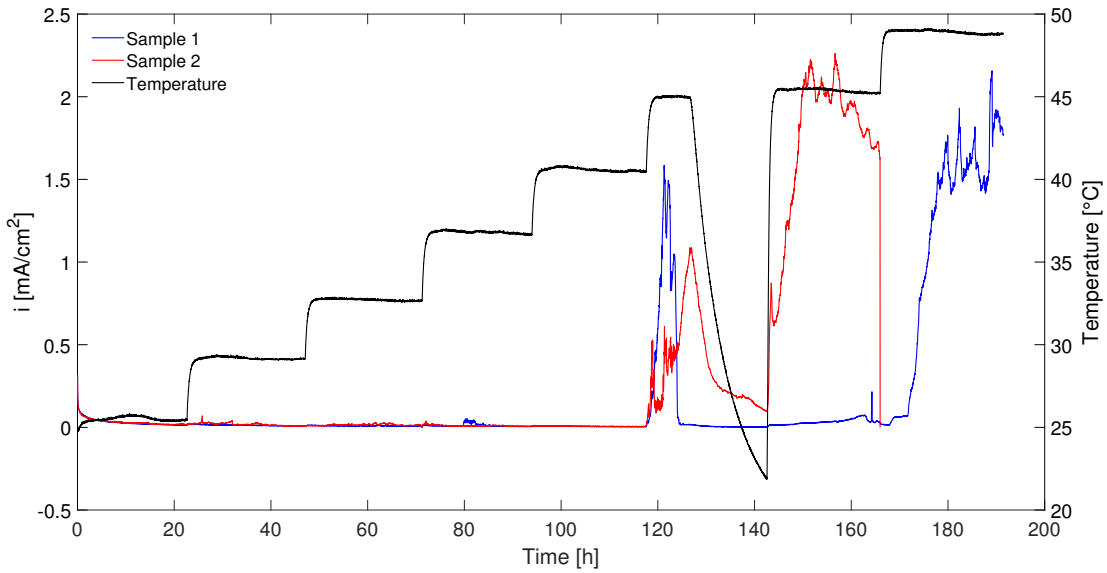

Figure 4.20: Recorded current densities for two UNS S32750 samples charged with a HCCD of -10 mA/cm^2, with no storage after hydrogen charging, according to Table 3.8.

Figure 4.21 shows the recorded current densities for two uncharged UNS S31254 samples. The current densities for both samples are very low until corrosion occurs at 56 ℃ and 58 ℃ for sample 1 and 2, respectively.

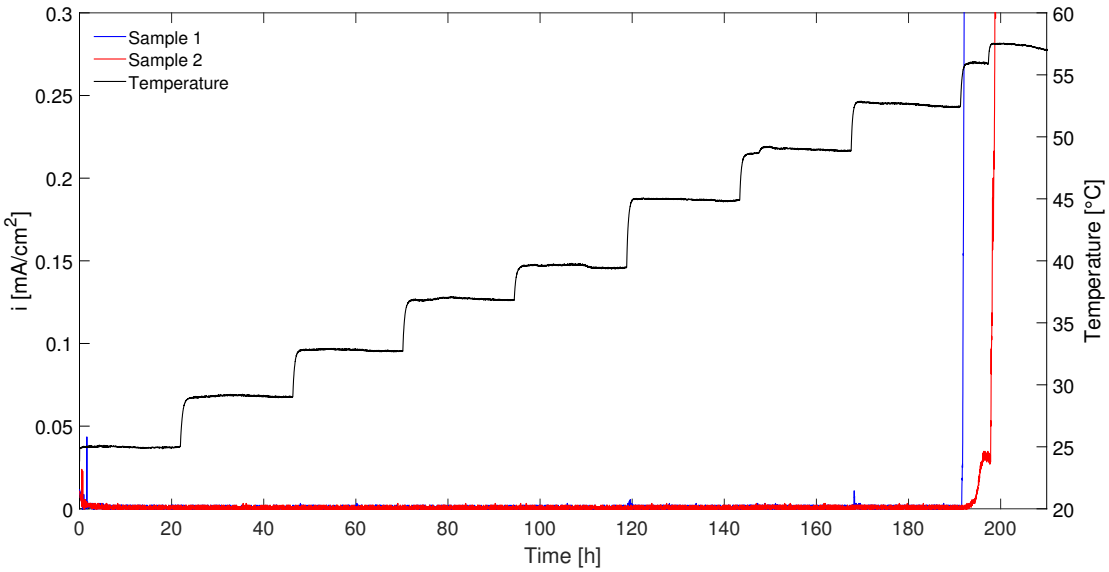

Figure 4.21: Recorded current densities for two uncharged UNS S31254 samples, according to Table 3.10.

Figure 4.22 shows the recorded current densities for two UNS S31254 samples charged with a HCCD of -0.1 mA/cm^2, with no storage after hydrogen charging. Both samples initiated corrosion at 25 °C, because of the stable current densities above 0.1 mA/cm^2 coupled with visible corrosion products on both samples.

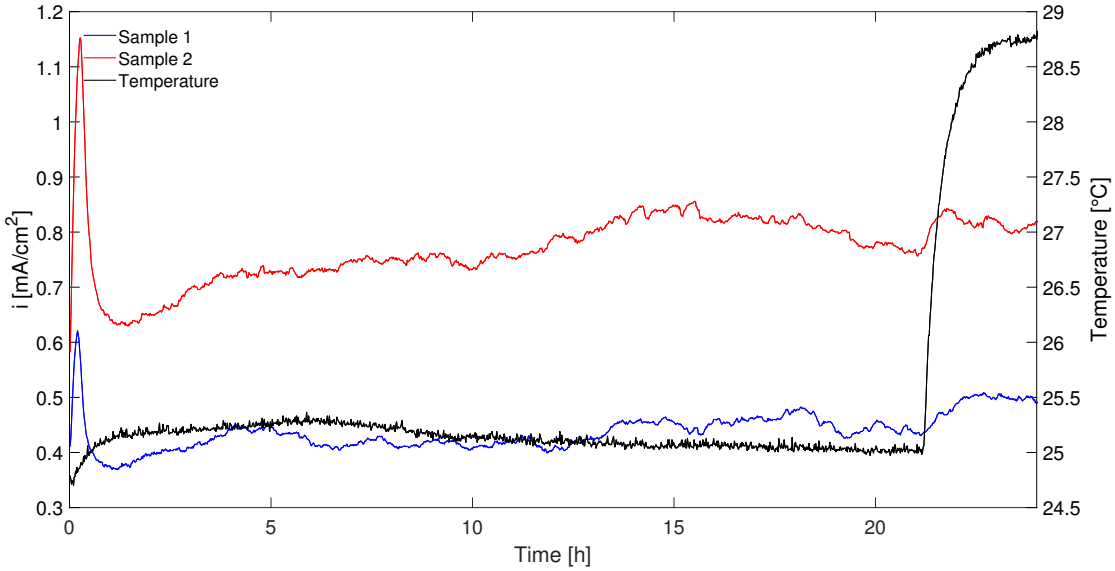

Figure 4.22: Recorded current densities for two UNS S31254 samples charged with a HCCD of -0.1 mA/cm^2, with no storage after hydrogen charging, according to Table 3.10.

Figure 4.23 shows the recorded current densities for two UNS S31254 samples charged with a HCCD of -0.1 mA/cm^2, with 7 days of storage in air after hydrogen charging. Both samples exhibit low current densities until initiation of crevice corrosion at 57 ℃.

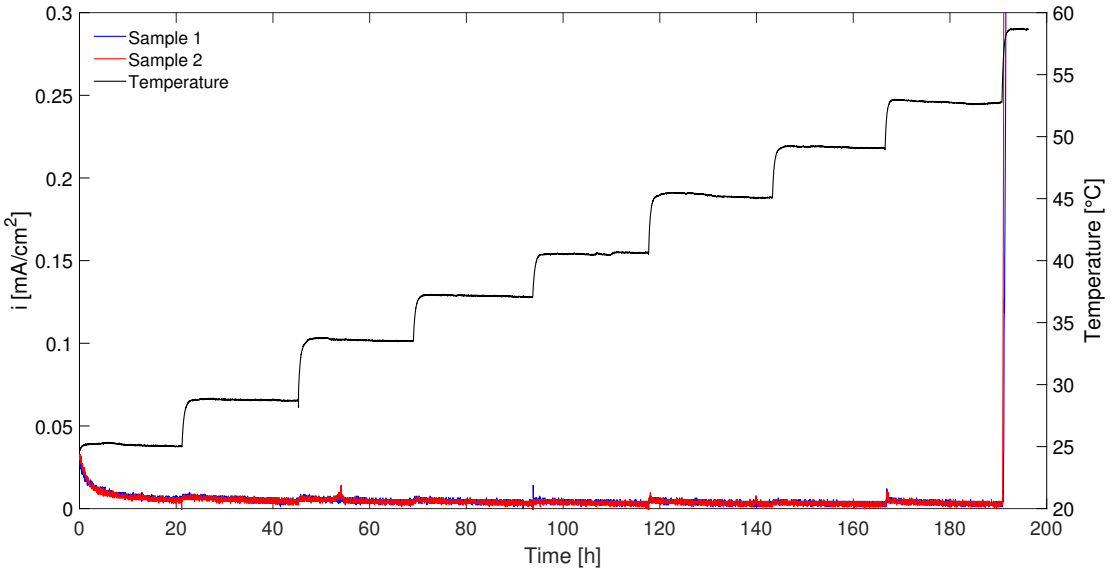

Figure 4.23: Recorded corrosion current densities for two UNS S31254 samples charged with a HCCD of -0.1mA/cm^2, with 7 days of storage in air after hydrogen charging, according to Table 3.10.

Based on the Figure 4.12 to 4.23 presented above and the given method of determining CCT, the CCTs for the samples tested are given in Table 4.3 to 4.5.

Table 4.3: The determined CCTs of UNS S32750 samples from batch 2 with different periods of storage. ΔT is the temperature difference between the CCT of the uncharged sample and the CCT of the charged sample.

HCCD [mA/cm²]	**Charge duration [h]**	**Storage time [days]**	**Sample number**	**CCT [℃]**	**ΔT [℃]**
Uncharged	24	No	1	65	N/A
-0.1	24	No	1	37	28
			2	37	28
-0.1	24	1	1	45	20
			2	45	20
-0.1	24	7	1	50	15
			2	40	15
-0.1	24	30	1	45	20
			2	45	20
-0.1	168	No	1	41	24
			2	46	19
-10	24	No	1	49	16
			2	45	20

Table 4.4: The determined CCTs of welded UNS S32750 samples exposed to different HCCDs. ΔT is the temperature difference between the highest CCT of the uncharged samples and the CCT of the charged sample.

HCCD [mA/cm²]	Charge duration [h]	Sample number	CCT [°C]	ΔT [°C]
Uncharged	24	1	61	N/A
		2	57	N/A
-0.1	24	1	49	12
		2	49	12

Table 4.5: The determined CCTs of UNS S31254 samples with different periods of storage. ΔT is the temperature difference between the highest CCT of the uncharged samples and the CCT of the charged sample.

HCCD [mA/cm²]	Charge duration [h]	Storage time [days]	Sample number	CCT [°C]	ΔT [°C]
Uncharged	24	No	1	56	N/A
			2	58	N/A
-0.1	24	No	1	25	33
			2	25	33
-0.1	24	7	1	57	1
			2	57	1

4.3 Surface characterisation

4.3.1 XPS

Figure 4.24 to 4.29 show the results obtained from the XPS analysis of the samples from batch 2 of UNS S32750.

Figure 4.24 shows that the atomic percentage of oxygen is high independent of HCCD and storage time. The oxygen content decreases with increasing sputtering time, i.e. depth into the material. The highest atomic percentage of oxygen is observed for a HCCD of -10 mA/cm^2. The atomic percentage of Fe and Cr are close. Fe increases with sputtering time, while Cr and Mo are relatively constant. Figure 4.24a and 4.24d, for the uncharged sample and the sample stored for 7 days, respectively, are similar, both in trends and values.

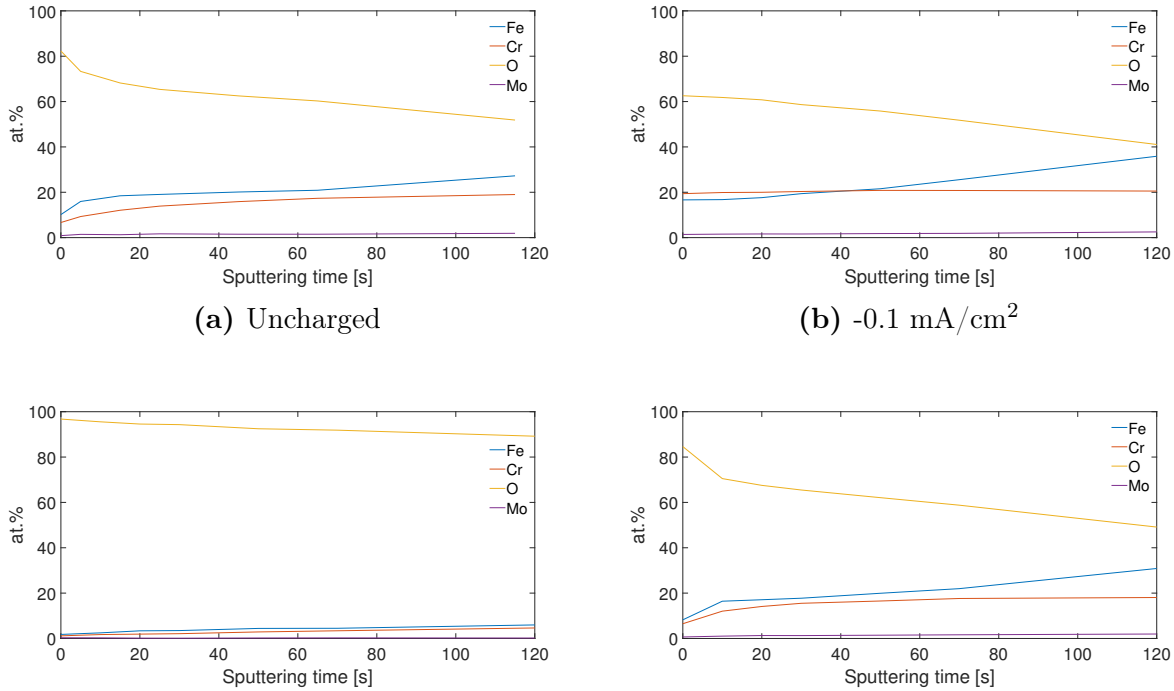

(a) Uncharged

(b) -0.1 mA/cm^2

(c) -10 mA/cm^2

(d) 7 days of storage

Figure 4.24: Overview of the atomic percentage of Fe, Cr, Mo and O as a function of sputtering time in the samples prepared according to Table 3.11.

Figure 4.25 shows a clear difference between the sample charged with a HCCD of -10 mA/cm^2 and all the remaining samples. All the metallic compounds result in a lower atomic percentage at -10 mA/cm^2 compared to the other samples, while oxygen is displaying highest values at -10 mA/cm^2. Common for Fe and Mo is the increase with sputtering time.

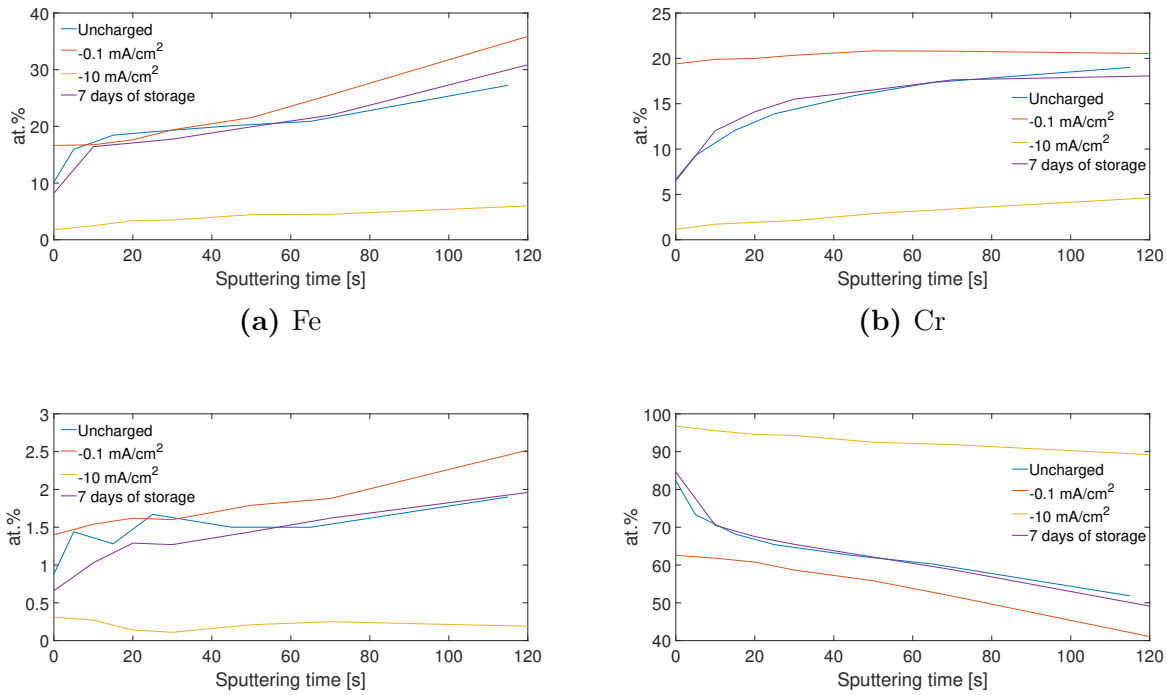

(a) Fe **(b)** Cr **(c)** Mo **(d)** O

Figure 4.25: Comparison of the atomic percentage of Fe, Cr, Mo and O with different HCCDs and storage time according to Table 3.11, as a function of sputtering time.

Figure 4.26 shows the relative atomic percentage of the elements Fe, FeO, Fe_2O_3 and Fe_3O_4. The uncharged sample, the sample charged with -0.1 mA/cm^2 and the sample stored for 7 days are all showing high relative atomic percentage of Fe which increases with sputtering time, a relative atomic percentage of FeO which decreases with sputtering time and similar Fe_2O_3 and Fe_3O_4 relative atomic percentage which decreases fast with sputtering time and stabilise, except the sample stored for 7 days where they are stable the whole time. A HCCD of -10 mA/cm^2, on the other hand, results in a relative atomic percentage of Fe which is lower than that of FeO and a relative atomic percentage of Fe_2O_3 and Fe_3O_4 which is higher than for the other samples and not showing similar values. 7 days of storage results in the lowest relative percentage of Fe oxides.

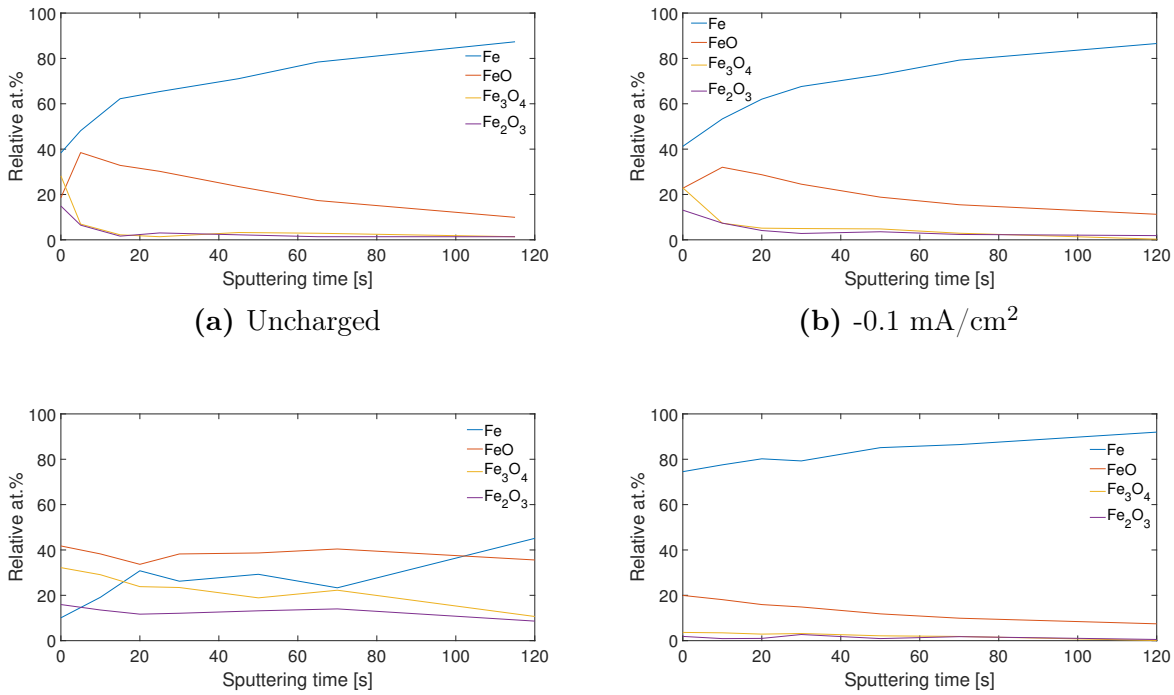

(a) Uncharged

(b) -0.1 mA/cm^2

(c) -10 mA/cm^2

(d) 7 days of storage

Figure 4.26: Overview of the relative atomic percentage of Fe, FeO, Fe_2O_3 and Fe_3O_4 as a function of sputtering time in the samples prepared according to Table 3.11.

Similar to the results obtained in Figure 4.25, the sample charged with -10 mA/cm^2 is showing results which are deviating from the remaining samples in Figure 4.27 as well. The Fe oxides are showing highest relative atomic percentage at -10 mA/cm^2 which decreases with sputtering time, while Fe is showing the lowest relative atomic percentage which increases with sputtering time. The uncharged sample and the sample charged with -0.1 mA/cm^2 are showing similar trends and values. Fe_2O_3 and Fe_3O_4 for the uncharged sample and the sample charged with -0.1 mA/cm^2 are showing a steep decrease in relative atomic percentage during the first 20 seconds of sputtering before they stabilise.

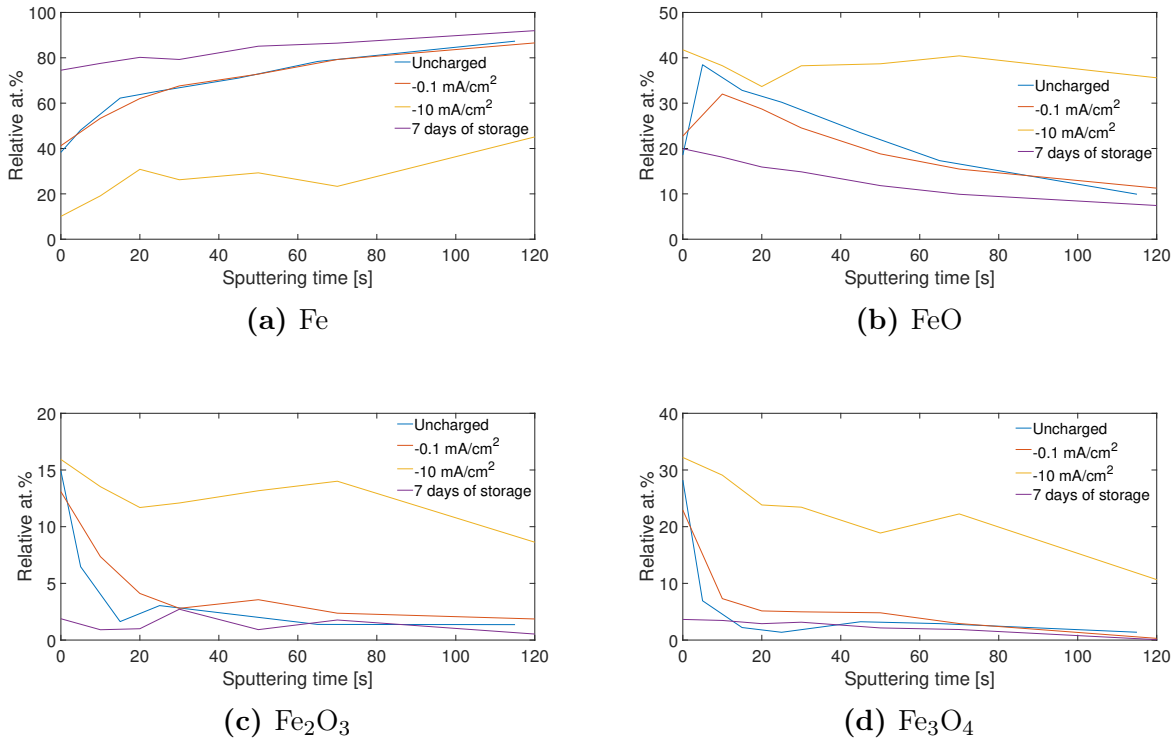

(a) Fe **(b)** FeO **(c)** Fe_2O_3 **(d)** Fe_3O_4

Figure 4.27: Comparison of the relative atomic percentage of Fe, FeO, Fe_2O_3 and Fe_3O_4 with different HCCDs and storage time according to Table 3.11, as a function of sputtering time.

Figure 4.28 shows that the uncharged sample and the stored sample both show highest relative atomic percentage of Cr_2O_3. The sample charged with -0.1 mA/cm^2 has a highest percentage of $Cr(OH)_3$ at sputtering time 0 to approximately 7, thus at the surface of the material, however, with increasing sputtering time the percentage of Cr_2O_3 increases above that of $Cr(OH)_3$. The relative atomic percentage of Cr increases with sputtering time for all samples except the one charged with -10 mA/cm^2. The sample charged with -0.1 mA/cm^2 and the sample stored for 7 days are showing increasing relative atomic percentage of Cr_2O_3 with sputtering time. The relative atomic percentage of $Cr(OH)_3$ and Cr_2O_3 for the sample charged with -10 mA/cm^2 are showing opposite trends; when $Cr(OH)_3$ increases Cr_2O_3 decreases, and vice versa.

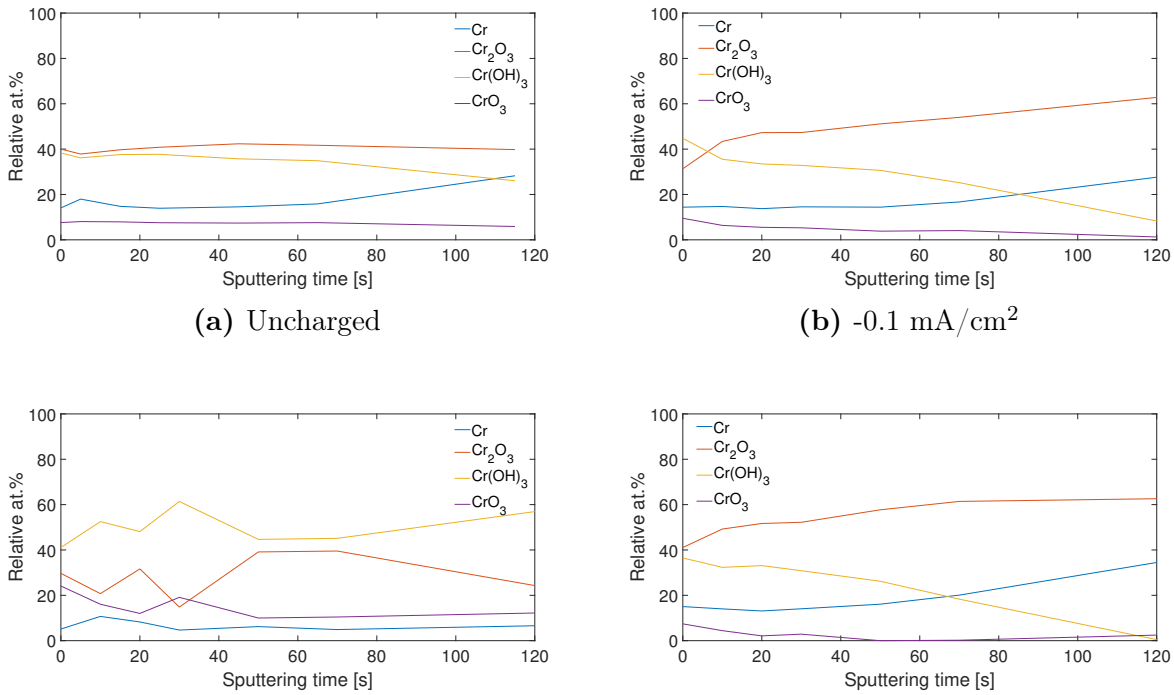

(a) Uncharged

(b) -0.1 mA/cm^2

(c) -10 mA/cm^2

(d) 7 days of storage

Figure 4.28: Overview of the relative atomic percentage of Cr, Cr_2O_3, $Cr(OH)_3$ and CrO_3 as a function of sputtering time in the samples prepared according to Table 3.11.

Figure 4.29 is also showing that the sample charged with -10 mA/cm^2 deviates from the other samples. While the relative atomic percentage of Cr increases with sputtering time for the uncharged sample, the sample charged with -0.1 mA/cm^2 and the stored sample, it is relatively constant for the sample charged with -10 mA/cm^2. The relative atomic percentage of $Cr(OH)_3$ and CrO_3 is highest for the sample charged with -10 mA/cm^2, while the percentage of Cr_2O_3 is lowest for the same sample. The charged samples are showing highest relative atomic percentage of $Cr(OH)_3$ and CrO_3 at sputtering time 0. The uncharged sample is showing very little variation in the percentage of Cr_2O_3, $Cr(OH)_3$ and Cr_2O_3 with increasing sputtering time.

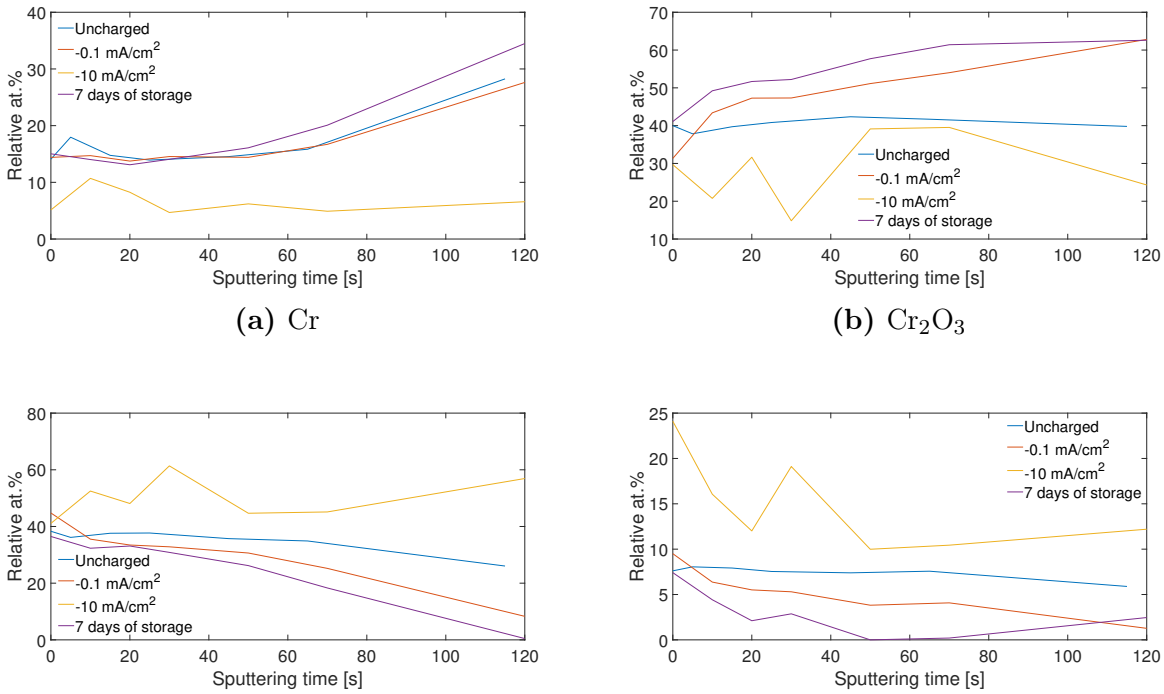

(a) Cr **(b)** Cr_2O_3 **(c)** $Cr(OH)_3$ **(d)** CrO_3

Figure 4.29: Comparison of the relative atomic percentage of Cr, Cr_2O_3, $Cr(OH)_3$ and CrO_3 with different HCCDs and storage time according to 3.11, as a function of sputtering time.

The Cr_2O_3/CrO_3 ratio was calculated from the results obtained with XPS at sputtering time 0 s for each test condition. The estimated ratios are shown in Table 4.6. A decrease in the Cr_2O_3/CrO_3 ratio is observed with increasing HCCD. The sample stored for 7 days exhibits the highest value.

Test condition	**Cr_2O_3/CrO_3 ratio**
Uncharged	5.26
-0.1 mA/cm^2	3.30
-10 mA/cm^2	1.23
7 days of storage	5.55

Table 4.6: The estimated Cr_2O_3/CrO_3 ratio for samples examined with XPS according to Table 3.11 at sputtering time 0 s.

The OH^-/O^{2-} ratio was calculated from the results obtained with XPS at sputtering time 0 s for each test condition. The estimated ratios are shown in Table 4.7. An increase in the OH^-/O^{2-} ratio is observed with increasing HCCD. The sample stored for 7 days displays the lowest ratio.

Test condition	**OH^-/O^{2-} ratio**
Uncharged	2.83
-0.1 mA/cm^2	4.86
-10 mA/cm^2	15.51
7 days of storage	0.53

Table 4.7: The estimated OH^-/O^{2-} ratio for samples examined with XPS according to Table 3.11 at sputtering time 0 s.

4.3.2 SEM and EDS

Figure 4.30 shows the SEM image taken of a UNS S32750 sample from batch 2. The whole area is found under the crevice former. The left and right parts of the image show no signs of corrosion. The middle part, however, shows the corrosion attack where areas showing different degrees of corrosion are seen. Selected spots were studied by EDS, and these are

shown in Figure 4.31. Spot 1 and 2 are situated outside of the corrosion attack, while spot 3 to 8 are found within the corroded area. Spot 3, 4 and 7 are showing less signs of corrosion compared to spot 5, 6 and 8. The weight percentages of Cr and Mo obtained with EDS for the different spots are given in Table 4.8. The PREN value for each spot was estimated using Equation 2.5 without wt% N since N cannot be measured with EDS. The obtained PREN values are therefore lower than what the actual values would have been if wt% N had been included. The difference in PREN value for spot 5, 6 and 8 compared to spot 3, 4 and 7 is found to be approximately 8, where the latter spots display the highest values. The PREN values for spot 1 and 2 are found to be in between those of spot 5, 6 and 8 and spot 3, 4 and 7.

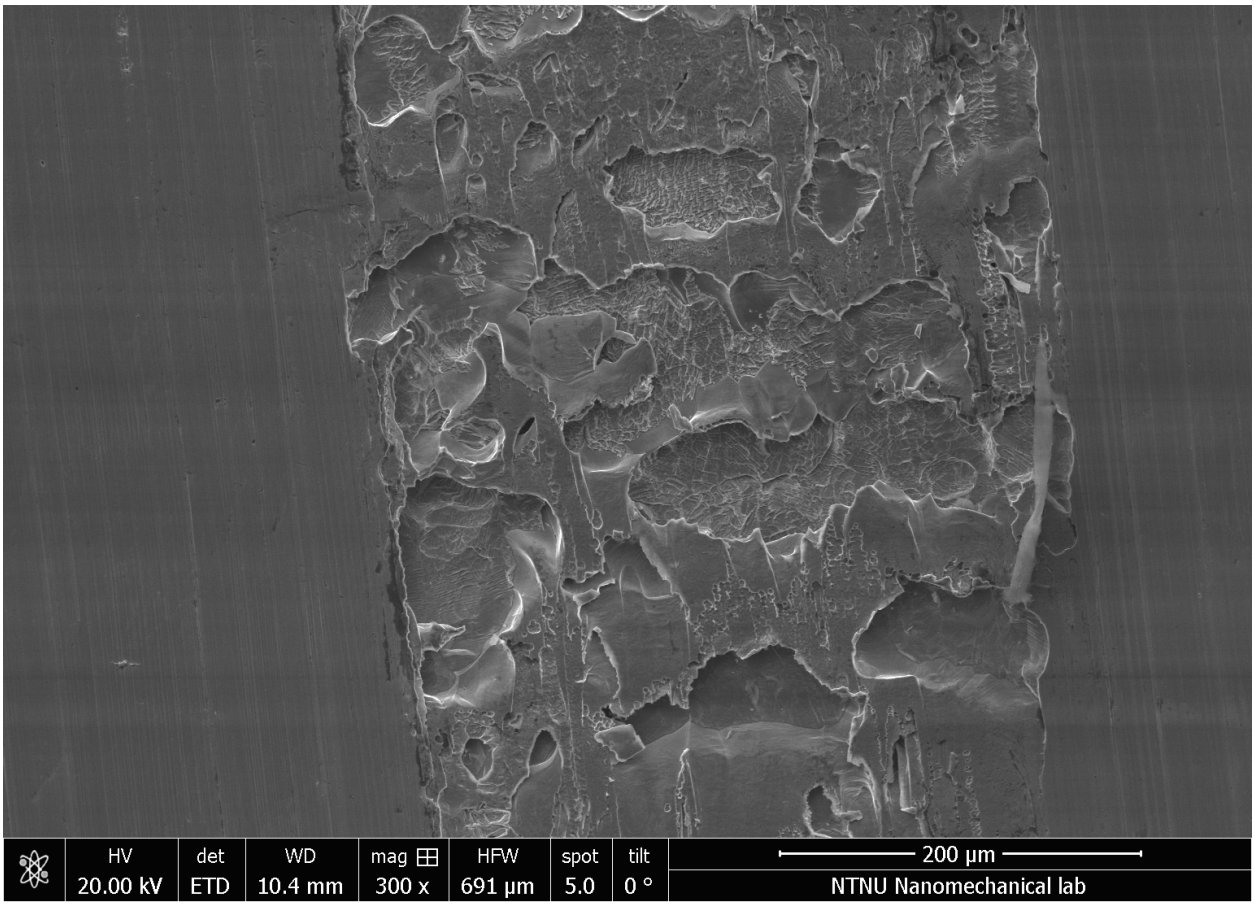

Figure 4.30: SEM image of crevice corrosion attack on a UNS S32750 samples charged with a HCCD of -10 mA/cm^2.

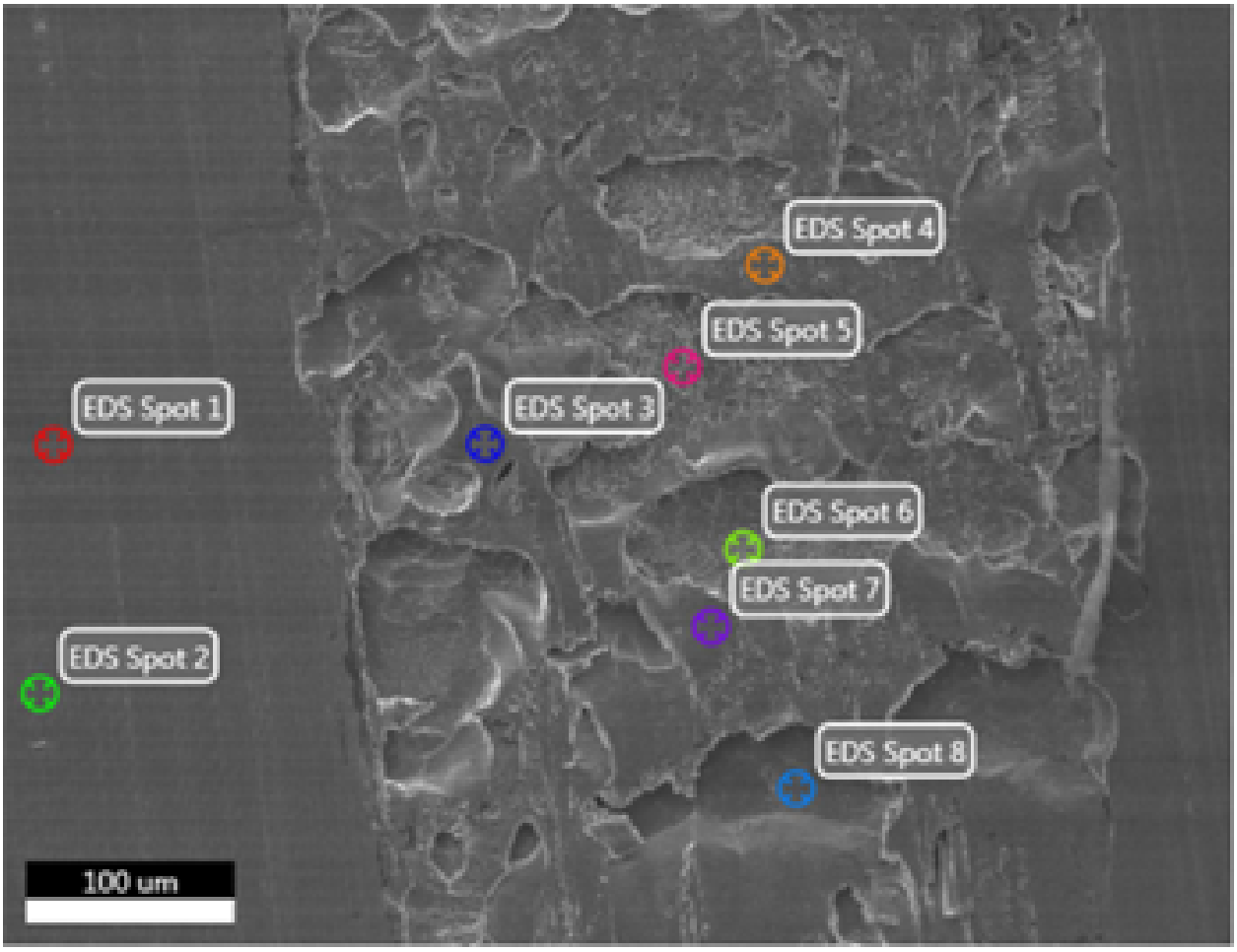

Figure 4.31: SEM image with selected areas highlighted where EDS analysis was performed.

EDS spot number	wt% Cr	wt% Mo	PREN
1	25.79	3.26	36.6
2	26.41	2.54	34.8
3	26.97	3.87	39.7
4	27.57	3.71	39.8
5	25.18	1.81	31.2
6	22.88	2.56	31.3
7	27.77	3.66	39.9
8	25.19	1.68	30.7

Table 4.8: Overview of the weight percent of chromium and molybdenum and the calculated PREN values using Equation 2.5 for the different EDS sites shown in Figure 4.31. The PREN values were estimated without wt% N.

4.4 Mott-Schottky analysis

Figure 4.32 shows the Mott-Schottky plot recorded for the passive film formed at 650 $mV_{Ag/AgCl}$ on an uncharged UNS S32750 sample. Based on the transition from a positive slope to a negative slope at -500 $mV_{Ag/AgCl}$, the oxide layer exhibits a change in semiconductor behaviour from n-type at potentials lower than -500 $mV_{Ag/AgCl}$ to p-type at higher potentials. The highest value for $1/C^2$ is found to be $5 \cdot 10^{12}$ cm^4/F^2 at the transition potential. Based on Equation 2.8 and 2.9 and the slopes of the plot, the donor and acceptor densities were calculated to be $3.54 \cdot 10^{14}$ cm^{-3} and $3.19 \cdot 10^{14}$ cm^{-3}, respectively.

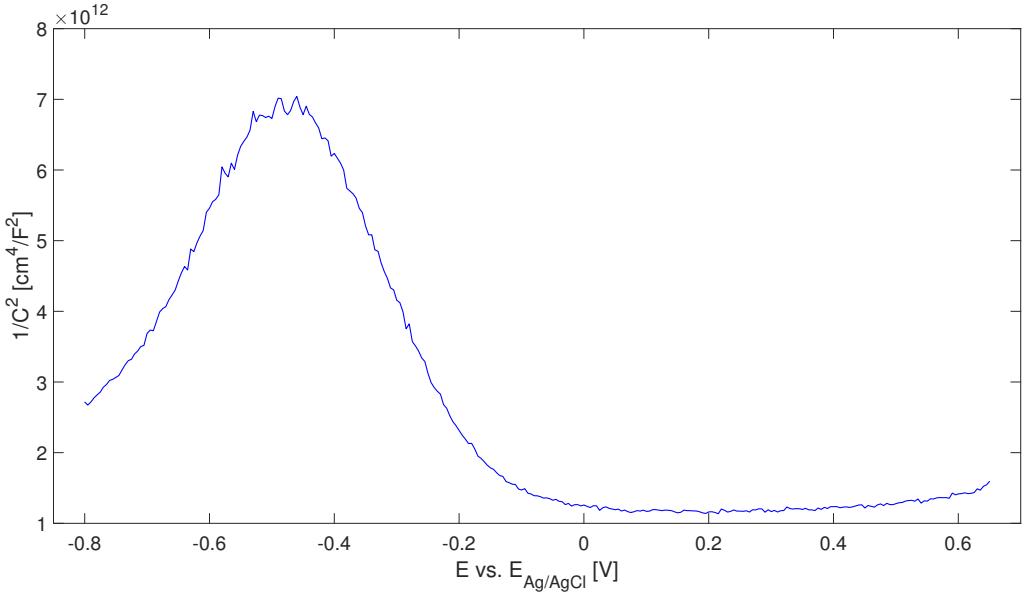

Figure 4.32: Mott-Schottky plot of the passive film formed at 650 mV for a UNS S32750 sample not charged with hydrogen.

Figure 4.33 shows the Mott-Schottky plot recorded for the passive film formed at 800 $mV_{Ag/AgCl}$ on a UNS S32750 sample charged with a HCCD of -0.1 mA/cm^2. Based on the transition from a positive slope to a negative slope at -500 $mV_{Ag/AgCl}$, the oxide layer exhibits a change in semiconductor behaviour from n-type at potentials lower than -500 $mV_{Ag/AgCl}$ to p-type at higher potentials. The highest value for $1/C^2$ is found to be $2.25 \cdot 10^{13}$ cm^4/F^2 at the transition potential. Based on Equation 2.8 and 2.9 and the slopes of the plot, the donor and acceptor densities were calculated to be $8.74 \cdot 10^{13}$ cm^{-3} and $1.05 \cdot 10^{14}$ cm^{-3}, respectively.

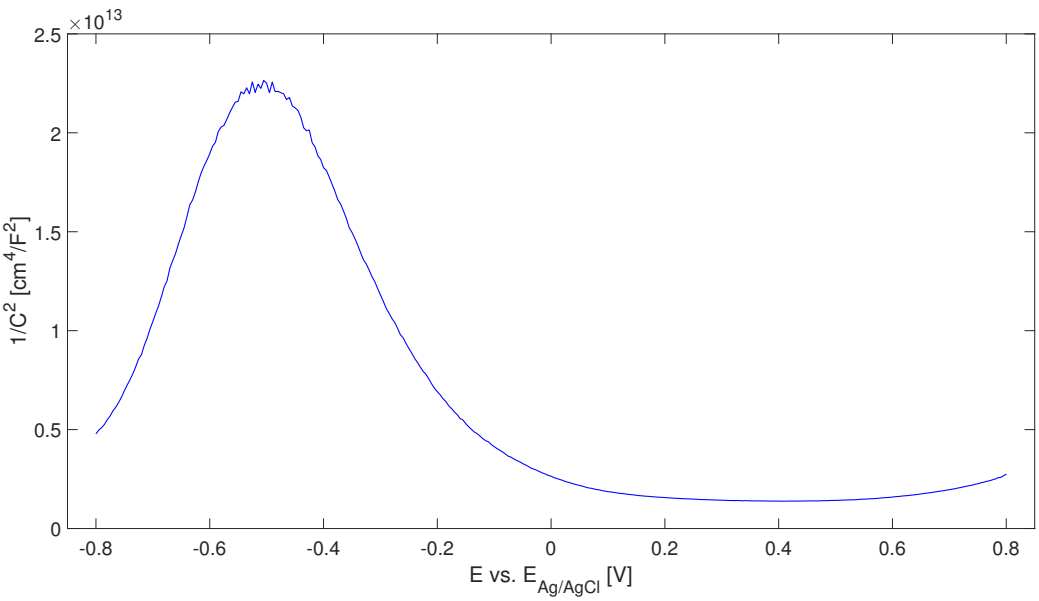

Figure 4.33: Mott-Schottky plot of the passive film formed at 800 mV for a UNS S32750 sample charged with hydrogen using a HCCD of -0.1 mA/cm^2.

Figure 4.34 shows the Mott-Schottky plot recorded for the passive film formed at 800 $mV_{Ag/AgCl}$ on a UNS S32750 sample charged with a HCCD of -10 mA/cm^2. Based on the transition from a positive slope to a negative slope at -600 $mV_{Ag/AgCl}$, the oxide layer exhibits a change in semiconductor behaviour from n-type at potentials lower than -600 $mV_{Ag/AgCl}$ to p-type at higher potentials. The highest value for $1/C^2$ is found to be $10 \cdot 10^{13}$ cm^4/F^2 at the transition potential. Based on Equation 2.8 and 2.9 and the slopes of the plot, the donor and acceptor densities were calculated to be $2.22 \cdot 10^{13}$ cm^{-3} and $2.25 \cdot 10^{13}$ cm^{-3}, respectively.

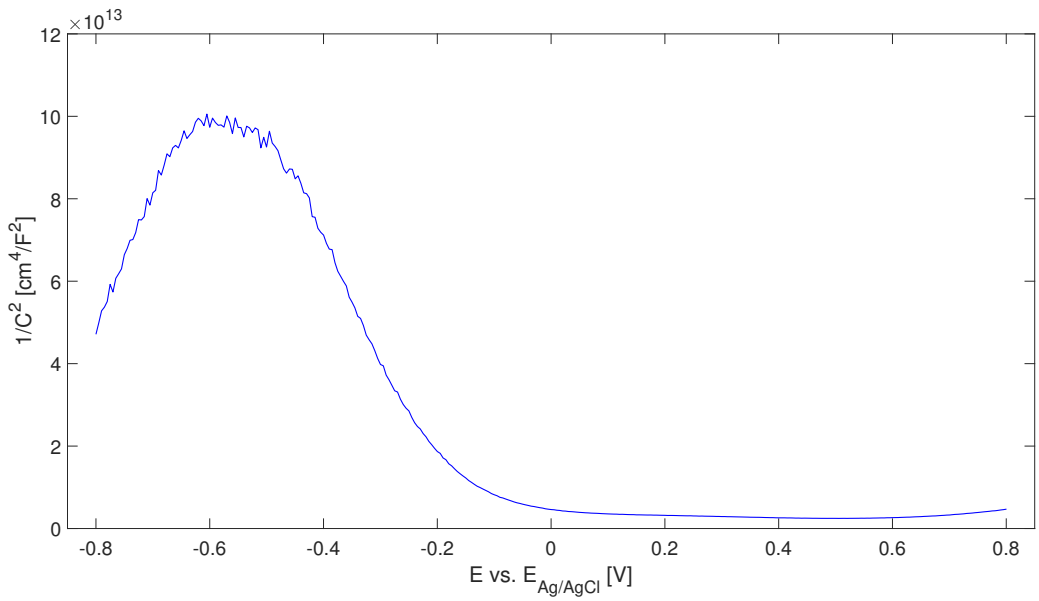

Figure 4.34: Mott-Schottky plot of the passive film formed at 800 mV for a UNS S32750 sample charged with hydrogen using a HCCD of -10 mA/cm^2.

5 Discussion

5.1 Effect of different hydrogen charge current densities

Anodic polarisation curves for batch 1 of UNS S32750 were recorded with varying HCCDs, and presented in Figure 4.1 and 4.2, at room temperature and 60 ℃, respectively. Hydrogen clearly affects the anodic polarisation curves as the E_{corr} decreases approximately 600 $\text{mV}_{\text{Ag/AgCl}}$ and 450 $\text{mV}_{\text{Ag/AgCl}}$ from uncharged to charged samples at room temperature and at 60 ℃, respectively. A decrease of the E_{corr} in the orders found here indicates a decreased corrosion resistance for samples charged with hydrogen. The increased anodic current density (later called current density) for charged samples also indicates a decreased corrosion resistance for these samples. Guo et al. (2013) investigated the effect of hydrogen charging on the pitting corrosion susceptibility of UNS S32750 in a 0.5 M H_2SO_4 + 3 % NaCl solution at room temperature [53]. Yao et al. (2016) investigated the effect of hydrogen charging on the electrochemical characteristics of UNS S32205 in deoxidised borate buffer solution with various chloride concentrations [26]. HCCDs used by Guo et al. ranged from -0.1 mA/cm^2 to -10 mA/cm^2 with a charge duration of 24 hours, while those used by Yao et al. ranged from -0.5 mA/cm^2 to -10 mA/cm^2 with charge duration of 1 hour. Both studies were performed at room temperature. The results obtained by Guo et al. and Yao et al. revealed a decrease in E_{corr} with increasing HCCD and a simultaneous increase in current density [53, 26], indicating decreased corrosion resistance for the charged samples. The results shown in Figure 4.1 display the same increase in current density, while the E_{corr} is found to be similar for all the charged samples, independent of the HCCD. The largest potential difference between the uncharged samples and the charged samples was 400 mV and 250 mV for Guo et al. and Yao et al., respectively. A larger potential difference of 600 mV is observed in Figure 4.1. This might be due to E_{corr} values around -350 $\text{mV}_{\text{Ag/AgCl}}$ of charged samples tested by Guo et al., which is approximately 350 mV more positive than those obtained here, or in the case of Yao et al., the low E_{corr} of the uncharged sample at -500 $\text{mV}_{\text{Ag/AgCl}}$. The only significant difference in the experimental parameters found when comparing this study to the one performed by Guo et al. is the electrolyte, since Guo et al. used the same material, charge duration and HCCDs. The large difference in E_{corr} for charged samples observed when comparing the study of Guo et al. to the one performed here, can thus be expected to have been caused by the effect of the electrolytes. E_{corr} and the current density show similar trends at 60 ℃ as at room temperature for the charged samples of batch 1 of UNS S32750, and the values are similar too. The uncharged sample, on the

other hand, shows a decrease of approximately 300 mV in E_{corr} when the temperature is increased to 60 ℃. An increase of approximately one order of magnitude is also observed for the corrosion current density, i_{corr}, and a decrease in E_{pit} of approximately 200 mV, implying lower corrosion resistance of the uncharged sample with increasing temperature as well.

E_{pit} at room temperature for batch 1 of UNS S32750 is close to 1 V for all samples, independent of HCCD. Yao et al. observed the same for their samples, while Guo et al. saw a decrease in E_{pit} of approximately 900 mV when the HCCD was increased to 10 mA/cm^2. Guo et al. thus concluded that pitting corrosion susceptibility increased with a high HCCD at room temperature. The same can not be said based on the study of Yao et al. or the results obtained here. However, at 60 ℃, the charged samples show a decrease in E_{pit} of approximately 400 mV compared to the uncharged sample, see Figure 4.2. The decrease implies a lower pitting corrosion resistance with increasing temperature for the charged samples. As a consequence of the decrease in E_{pit}, the passive area extends over a smaller potential range of approximately 700 mV at 60 ℃ compared to the 1400 mV range at room temperature.

As can be seen from the determined CCTs shown in Table 4.2 to 4.4, hydrogen clearly decreases the CCTs of batch 1 of UNS S32750 and welded UNS S32750 samples. All charged samples of batch 1 initiated crevice corrosion at 25 ℃ independent of HCCD and charged duration, except sample 1 of the parallel charged with a HCCD of -10 mA/cm^2, which is regarded as an outlier. The CCT of the charged samples is thus more than halved compared to the uncharged samples which initiated at 52 and 56 ℃. The welded samples of UNS S32750 also show a decrease in CCT when comparing uncharged samples to charged samples, see Table 4.4. However, the decrease in CCT observed for the welded samples is only between 8 to 12 ℃. Thus, a large difference in the decrease of CCT for the charged samples from batch 1 and the charged welded samples is observed, indicating a larger, negative effect of hydrogen charging on batch 1.

When hydrogen exits stainless steel in aqueous environment, it could undergo oxidation to form H^+. This reaction has an equilibrium electrode potential which is approximately 1.8 V lower than that of the oxidation of Fe [54]. Thus, the E_{corr} of hydrogen charged stainless steel is lower than the uncharged samples, as seen in all polarisation curves. This could also explain the difference in E_{pit} found for batch 1 at 60 ℃. As explained in section 2.2.2, pitting corrosion typically initiates as a result of localised breakdown of the passive film on stainless steels. Thus, the decrease in pitting corrosion resistance observed at 60 ℃ is

likely a consequence of interactions between hydrogen and defects present in the passive film [53]. Absorbed hydrogen from the cathodic polarisation diffuse into the metal and oxidise to protons in the passive film. The protons gather around defects and thereby create an attraction site for negatively charged Cl^- ions which may adsorb on the passive film. Higher chloride concentration on the surface could cause local breakdown of the passive film, and thereby initiate pitting [53].

The decreased corrosion resistance observed for hydrogen charged samples is expected to have been caused by hydrogen interacting with the passive film on the stainless steel surface. Hydrogen is known to destabilise the oxide film and also alter its chemical composition, see section 2.3. The effect is, however, reversible [32], which is why stored samples are showing improved corrosion resistance. A significant difference between batch 1 and batch 2 of UNS S32750, as well as the welded UNS S32750 samples, is observed when comparing CCTs, see table 4.3 and 4.2, where batch 2 and the welded samples display higher temperature values. One possible explanation for this might be a difference in experimental procedure used. Batch 1 was not left for 1 hour to stabilise E_{corr}, while both batch 2 and the welded samples were. This could be a contributing factor for the higher current density values experienced from the start of the experiments for batch 1, and thus the low CCTs determined for these samples. During the 1 hour E_{corr} stabilisation, hydrogen might have diffused out of the stainless steel, similarly to that observed for stored samples. A lower hydrogen concentration within the stabilised stainless steel samples could explain the higher CCTs compared to the unstabilised samples from batch 1. The less effective pickling solution used for batch 1 of UNS S32750 compared to more effective pickling solution used for the samples from batch 2 of UNS S32750 as well as the welded samples from UNS S32750, may be another contributing factor to the large differences in CCT between the charged samples of these materials. Choi et al. (2003) investigated the effect of pickling on the pitting corrosion of a hyper duplex stainless steel. They found that with increasing pickling time, the pitting potential and passive region increased [55]. Previous research have also found the difference in CCT between pickled and unpickled samples of welded UNS S31254 grade stainless steel to be around 20 °C [56]. As can be seen from Table 3.1, there is not a significant difference in chemical composition between the two batches of UNS S32750, thus the chemical composition is not the reason for the large differences observed between the two batches.

5.2 Effect of storage time

Anodic polarisation curves for batch 2 of UNS S32750, welded UNS S32750 and UNS S31254 were recorded with different storage times. As can be seen from Figure 4.3 to 4.6, E_{corr} increases and the current density decreases with increasing storage time, independent of material type and temperature. Thus, storage time clearly exhibits a positive effect on the corrosion resistance of stainless steel that has been charged with hydrogen.

E_{pit} for batch 2 at room temperature is independent of storage time, and is found around 1 $V_{\text{Ag/AgCl}}$, similar to that obtained for batch 1 in Figure 4.1. This indicates that E_{pit} is independent of both HCCD and storage time for UNS S32750 at room temperature. At 60 ℃ the samples stored for 7 and 30 days are showing E_{pit} values around 300 and 400 $mV_{\text{Ag/AgCl}}$, see Figure 4.4, respectively, while the other samples have E_{pit} values similar to those obtained at room temperature. A storage time of 7 and 30 days thus results in similar E_{pit} values as samples with no storage time charged with HCCDs of -0.5 mA/cm^2, -1 mA/cm^2 and 10 mA/cm^2 tested at 60 ℃, see Figure 4.2. However, the current density in the passive area is lower for the stored samples. The effect of increased storage time thus increases the corrosion resistance more than an increased HCCD decreases the corrosion resistance.

E_{pit} of the welded samples of UNS S32750 is approximately 400 mV lower than the samples from batch 2 of UNS S32750 indicating increased pitting susceptibility for the welded samples, see Figure 4.3 and 4.5. The current density in the passive region for samples stored for 7 days is similar for the two stainless steel samples. However, the welded sample stored for 30 days shows lower current density than the UNS S32750 sample stored for the same period. The lower current density value might indicate a larger positive, effect of storage time on the welded samples compared to the non-welded UNS S32750 samples regarding corrosion resistance. As mentioned in section 2.1.3, the welding process can introduce enough heat to allow precipitation of secondary phases in the metal. The precipitation of the σ phase can be a reason for why the E_{pit} decreases significantly for the welded UNS S32750 samples, caused by the chromium depleted areas left behind when the phase precipitates, see section 2.1.3. The determined CCTs for the uncharged and charged samples of welded UNS S32750 are not indicating the precipitation of the σ phase, as the difference is only 12 ℃. Precipitation of the σ phase, however, has not been investigated in this work.

Similar potential and current density values are observed for samples from UNS S32750 and samples from UNS S31254 at room temperature in Figure 4.3 and 4.6. Thus, no evident effect of the difference in chemical composition is observed when comparing the electrochemical behaviour of the materials in the form of polarisation curves.

No E_{corr} values lower than 800 $\text{mV}_{\text{Ag/AgCl}}$ are observed for any sample independent of HCCD, storage time and temperature. This could indicate that there exists a limit as to how much hydrogen charging and storage time can decrease the E_{corr} values of the materials used in this study, and that this limit might be around 800 $\text{mV}_{\text{Ag/AgCl}}$. The current density, on the other hand, depends on both HCCD and storage time, and the largest differences are observed between samples with different storage time.

The effect of storage time on the CCTs of samples from batch 2 of UNS S32750 and samples of UNS S31254 was investigated, and the results are presented in Table 4.3 and 4.5. Similar for both materials is the decrease in CCT for charged samples compared to uncharged samples.

The samples from batch 2 stored for 1 day and 30 days exhibit the same CCTs of 45 °C. The fact that these temperatures are equal, indicates that the hydrogen present in the samples diffuse out of the material fast, and more than 30 days of storage may be needed to get a larger repassivating effect on the stainless steel. This is, however, contradicting to the results gathered from the polarisation curves, where a clear decrease in current density is seen for samples stored for longer time.

The two samples from batch 2 stored for 7 days are showing both higher and lower CCTs when compared to the samples stored for 1 day and 30 days. The mean value is however equal to the CCTs obtained after 1 and 30 days of storage. The reason for the differences in observed temperatures could be stochastic differences in the samples, and previous research has also shown that recorded CCTs for the same material may span over a wide range of temperatures, sometimes as large as 30 °C [56].

Surprisingly, unstored UNS S32750 samples from batch 2 charged with -0.1 mA/cm^2 for 168 h and samples charged with -10 mA/cm^2 for 24 h show CCTs which are higher than the unstored sample charged with -0.1 mA/cm^2, indicating a positive effect of increased hydrogen concentration on the CCT. Further examination is required to conclude upon whether these result are within a statistical error margin.

As can be seen in Table 4.5, unstored, charged UNS S31254 samples show a similar decrease in CCT as the charged samples from batch 1 of UNS S32750. The stored samples, however, show a similar CCT as the uncharged samples. The fact that the CCTs for the uncharged samples and the stored samples are similar indicate that the stored samples have repassivated completely. This is very contradicting to the polarisation curves for the uncharged and stored sample, which show that the stored sample have a decreased corrosion resistance compared to the uncharged sample.

The large difference in CCTs between uncharged and charged UNS S31254 samples can be explained by the microstructure of the material. As UNS S31254 is a austenitic stainless steel, it will contain mainly austenite. As mentioned in section 2.1.1, the solubility of hydrogen in austenite is much higher than the solubility in ferrite. Thus, charging UNS S31254 with hydrogen would lead to a higher concentration of hydrogen in the samples, when compared to samples of UNS S32750, which contains roughly 50 % austenite. This would lead to a much more destabilised oxide layer when the higher concentration of hydrogen reacts with the oxides existing in the film. Since UNS S31254 contains a higher amount of austenite than UNS 32750, the effect of hydrogen charging would thus be much more severe. This is clearly seen from the CCTs determined for the UNS S31254 samples [11, 53, 57]. Figure 4.30 and 4.31 also confirm this selective corrosion of the austenite phase, which will be discussed further in section 5.3.

The positive effect on the corrosion resistance observed with increasing storage time could be due to repassivation of the samples during storage. Due to the low solubility of hydrogen in stainless steel, it tends to diffuse out of the material [54]. In ambient atmosphere the hydrogen would exit the steel as gas [54]. As the stainless steel samples investigated in this work were stored in ambient atmosphere, it is expected that hydrogen diffused out of the samples and thus contributed to the increased corrosion resistance.

5.3 Surface characterisation

XPS

The atomic percentage of Fe, O, Cr and Mo are similar for the uncharged sample and the sample stored for 7 days, see Figure 4.24, indicating that storage returns the material composition to near its initial state. However, the same is not observed for the relative atomic percentage of various Fe and Cr oxides and hydroxides. Additionally, the OH^-/O^{2-} ratio for the sample stored for 7 days is approximately 5 times lower than that of the uncharged sample, indicating a more defect-free oxide film for the stored sample. The polarisation curves, however, indicate a significantly better corrosion resistance for the uncharged sample compared to stored samples. The results from XPS and polarisation curves are thus clearly contradicting on the matter of the corrosion resistance of stored samples compared to uncharged samples.

The XPS-results for the samples charged with a HCCD of -10 mA/cm^2 are very different from the results gathered from the other three samples. This could indicate that larger alterations of the oxide layer occur with higher HCCDs. The larger current densities observed on the anodic polarisation curves with increasing HCCD also support this.

Guo et al. (2017) studied the effect of hydrogen on the passive film of a UNS S32750 stainless steel. Hydrogen charging was performed for 48 h with a HCCD of -1 mA/cm^2 [47]. They found that the oxide film structure of uncharged duplex stainless steel was mainly composed of $Cr(OH)_3$, Cr_2O_3, Fe_2O_3 and FeO, while it after hydrogen charging primarily consisted of $Cr(OH)_3$, CrO_3, Fe_3O_4 and FeOOH [47]. Here, at 0 sputtering time, the uncharged sample shows highest percentages for Cr_2O_3, $Cr(OH)_3$, Fe and Fe_3O_4, while the sample charged with -0.1 mA/cm^2 reveals that the oxide film mainly consists of $Cr(OH)_3$, Cr_2O_3, Fe, FeO and Fe_3O_4. Thus, similar chromium oxide compounds are observed for the uncharged samples, however, the iron oxides show completely opposite trends from this study compared to that of Guo et al. Both studies observe a decrease in the percentage of $Cr(OH)_3$ for the charged samples, but unlike the results collected here, Guo et al. observed a total disappearance of Cr_2O_3 for the charged sample. A significant difference between the results is that the results obtained here show high percentages of Fe and Cr at the surface, while Guo et al. mainly found oxides. Thus, the results are not comparable, which is surprising as the materials are similar. One reason for the deviations for the charged samples may be different HCCDs,

but this is not expected to be the full explanation. However, further explanations are not known.

Maurice et al. (1998) studied the passive film formed on Fe-18Cr-13Ni single-crystal surfaces [58]. They observed a dehydration of $Cr(OH)_3$, leading to more Cr_2O_3 in the oxide film. Growth of CrO_3 was also observed [58]. The XPS results obtained here show that the relative atomic percentage of $Cr(OH)_3$ is highest for the charged samples at sputtering time 0 s, see Figure 4.29c. $Cr(OH)_3$ has been found to promote localised corrosion, see section 2.2.1. Thus, charging stainless steel with hydrogen results in the formation of compounds in the oxide film which do not promote protection, but rather corrosion. The corrosion resistance is therefore expected to decrease. A possible explanation for the higher amount of $Cr(OH)_3$ observed on the charged samples could be that the absorbed hydrogen, in the form of protons, might slow down the formation of protective Cr_2O_3 and CrO_3 from $Cr(OH)_3$. Protons may additionally react with chromium at the surface and form more $Cr(OH)_3$. This, however, needs further examination. The ratio of Cr_2O_3/CrO_3 decreases with increasing HCCD, see Table 4.6, implying an effect of hydrogen on the formation reactions for these compounds. Figure 4.25c reveals that the atomic percentage of Mo is lowest for the sample charged with -10 mA/cm^2. Mo contributes to formation of Cr_2O_3 and CrO_3 from Cr^{3+} and Cr^{6+}. Both of these oxides are key species in the protective oxide film formed on stainless steel [22]. A low atomic percentage of Mo therefore implies less protective oxides in the oxide film which could further explain the decreased corrosion resistance observed for charged samples.

Guo et al. (2017) observed that hydrogen charging of UNS S32750 increased the conductivity of the passive film, explained by the increase in the OH^-/O^{2-} ratio for charged samples [47]. The calculated OH^-/O^{2-} ratio for the samples examined with XPS in this work increases for samples charged with increasing HCCD as well, thus implying a similar effect as that observed by Guo et al. An increased conductivity could be explained by the higher amounts of hydroxides in the oxide layer for charged samples, which typically contain more defects, and thus charge carriers, than oxides [59]. A higher conductivity contributes to more current and thus lower corrosion resistance of the material. Yang and Luo (2001) observed increasing pitting susceptibility for AISI310 stainless steel charged with hydrogen, and explained it with the higher disorder of the passive film under the influence of hydrogen [59].

SEM and EDS

The EDS analysis of the corroded UNS S32750 sample reveals clear differences in PREN values, depending on how severe the corrosion affected the different areas. The corroded areas with analysis spot 5, 6 and 8 show a much lower PREN value of approximately 31 compared to the uncorroded areas analysed in spot 3, 4 and 7 showing PREN values close to 40, see Table 4.8. This may explain why spot 5, 6 and 8 are affected by the corrosion attack, while spot 3, 4 and 7 are seemingly unaffected. Inclusion of N in the estimation of the PREN values for spot 3, 4 and 7, would highly likely increase the PREN values above 40, which is the minimum value needed for stainless steel to be applicable for use in seawater, due to their already high values. Spot 1 and 2 exhibit PREN values lower than the values for spot 3, 4 and 7, which is surprising considering that spot 1 and 2 look unaffected by the corrosion. The difference of 1.8 between the PREN values for spot 1 and 2 is also significant. As mentioned in section 2.1.2, Cr and Mo are more soluble in α than in γ. The lowered Mo value for spot 2 compared to spot 1 could indicate that spot 2 is γ, but the higher Cr value could indicate that it is α. It is thus hard to accurately conclude upon the difference in PREN value between spot 1 and 2. The increased values of both Cr and Mo in spot 3, 4 and 7 compared to the values of spot 5, 6 and 8 could indicate that the corroded areas are γ while the uncorroded areas are α. This implies selective corrosion of γ. Tsai et al (2003) investigated the selective corrosion of a 2205 duplex stainless steel in 0.01 M NaCl solution. They found that γ corroded before α [60]. Guo et al. (2013) also found that pitting initiated in γ before spreading into the α phase [53]. Both these studies support the results obtained from the SEM and EDS analysis of this work. As mentioned in section 5.3, Guo et al. (2017) observed that hydrogen increased the conductivity of the oxide film on UNS S32750, and the highest conductivity was found in the oxide film on the γ phase due to its higher hydrogen solubility compared to α [47], which could explain the observed selective corrosion of γ.

Mott-Schottky analysis

As can be seen from the Mott-Schottky plots shown in Figure 4.32 to 4.34, the general shape of the plots does not change much, regardless if the sample was charged with hydrogen or not. All the samples exhibit both n- and p-type semiconductor behaviour, at different applied potential ranges. The potential where the semiconductor behaviour shifts from n-type to p-type changes from -500 $mV_{Ag/AgCl}$ to -600 $mV_{Ag/AgCl}$ for the uncharged sample

compared to the sample charged with a HCCD of -10 mA/cm^2. This shift indicates that hydrogen charging increases the potential range for p-type behaviour, and increasing HCCD shifts the potential range to lower values. Yao et al. (2016) used Mott-Schottky analysis to study the effect of hydrogen charging, and found that uncharged samples exhibited both p- and n-type behaviour. Increasing HCCD, however, lead to gradual disappearance of the p-type behaviour, as well as higher donor densities [26]. The calculated values for N_d and N_a decrease with increasing HCCD. This is most unexpected, as the recorded polarisation curves and CCTs all point to a negative effect of hydrogen on the corrosion resistance. Based on these results, the densities of charge carriers should increase to ease the process of charge transfer, and thus corrosion. However, the results from this Mott-Schottky analysis imply the opposite. Yang et al. (1999) came to the same conclusion as Yao et al. regarding the disappearing p-type behaviour when they performed Mott-Schottky analysis on uncharged and charged AISI310 stainless steel samples. The results obtained in this thesis are thus contradicting to those obtained by Yao et al. and Yang et al., both with regard to n- and p-type behaviour and N_d and N_a with increasing HCCD.

Marconnet et al. (2008) obtained contradicting results from photoelectrochemical measurements compared to results from Mott-Schottky analysis, and partly explained it by a poor signal to noise ratio from Mott-Schottky [61]. However, the assumption of an ideal capacitor used in Mott-Schottky analysis was also used by Marconnet et al. to explain the deviating results and claimed not to be valid for stainless steel [61]. The results obtained from Mott-Schottky analysis depend on the solution media, the applied potential and the chosen frequency [47, 61]. Thus, a comparison of Mott-Schottky results obtained from different studies may not be easily comparable, which could partly explain why the results obtained in this work deviate from previous studies.

5.4 Further work

The effect of hydrogen on the corrosion resistance of various stainless steel grades can be investigated further with the following steps.

As stated in [32], the applied HCCDs used in relevant studies have not necessarily been selected based on realistic conditions when hydrogen from CP diffuses into stainless steel. This is, however, useful when investigating the effect hydrogen has on the corrosion resistance of stainless steel. Thus, a determination of correct HCCD based on field measurements of hydrogen concentrations within stainless steel after CP is needed.

Because the CCT of a material may vary over a wide range of temperatures, more tests on each material are needed to calculate a mean CCT with standard deviation for all samples. Repeating experiments up to 10 to 15 times might be necessary to get a statistically significant number of experiments. A lower starting temperature than 25 ℃ should be used for the samples that initiated crevice corrosion at 25 ℃ to find the lowest starting temperature.

The amount of dissolved Fe for uncharged and charged samples during electrochemical testing can be measured with inductively coupled plasma optical emission spectroscopy (ICPOES) and compared, similar to the analysis conducted by Thomas et al. (2016) [54]. The electrolyte should be slightly acidic to assure that Fe ions stay soluble and thus can be detected with ICPOES.

Similar tests as performed here should be conducted on stainless steel samples polarised in actual seawater, and the effect of immersion time, applied potential and seawater temperature should be investigated. The effect of calcareous deposits formed during exposure should also be examined.

6 Summary and conclusions

The effect of different hydrogen charge current densities and storage periods on the corrosion resistance of stainless steel exposed to artificial seawater were investigated in this thesis.

The anodic polarisation curves for the samples from batch 1 and 2 of UNS S32750, welded UNS S32750 and UNS S31254 show the same trends. The E_{corr} decreases drastically from the uncharged samples to samples charged with hydrogen. The anodic current densities were also found to increase with increasing HCCDs. An increase of the E_{corr} and a decrease in anodic current densities when the samples are stored after hydrogen charging was also observed. The anodic polarisation curves thus show that hydrogen charging decreases the corrosion resistance, while storage after hydrogen charging improves the corrosion resistance through repassivation. The determined CCTs also result in a large difference between uncharged and charged samples, similar to that observed in the anodic polarisation curves. The charged samples show lower CCTs than the uncharged ones. Samples from batch 1 of UNS S32750 shows the largest differences between uncharged samples and charged samples, compared to the other materials, likely caused by the use of a less effective pickling solution for the treatment of batch 1. The XPS results show that the hydrogen charged samples have an increased concentration of $Cr(OH)_3$ species in the oxide layer, compared to the more protective species like Cr_2O_3 and CrO_3. The OH^-/O^{2-} ratio is also found to increase with increasing HCCD. All the gathered results show a clear negative effect of hydrogen on the corrosion resistance of stainless steel. A few possible phenomenons could explain this decrease in corrosion resistance. Oxidised hydrogen in the form of protons in the passive film could gather around defects and thus create attraction sites for species like Cl^-, which would then adsorb on the oxide layer, causing local breakdown of the film. Oxidised hydrogen could also slow down the formation of Cr_2O_3 and CrO_3 from $Cr(OH)_3$. In addition, the protons might react with pure Cr and create more $Cr(OH)_3$. As $Cr(OH)_3$ in the passive film promotes localised corrosion, the increased concentration of this species in the hydrogen charged samples could explain the decreased corrosion resistance. The increase of OH^-/O^{2-} ratio with increasing HCCD also suggests a higher conductivity in the passive film of hydrogen charged samples, which implies a lowered corrosion resistance.

SEM and EDS analysis show selective corrosion of γ in the hydrogen charged sample. The higher hydrogen dissolution and lower hydrogen diffusion in γ compared to α is likely the cause of the selective corrosion of γ.

Mott-Schottky analysis results in electrical characteristics of the oxide film which are contradicting to results obtained in previous studies, thus further analysis is needed on this point. However, due to the dependence of Mott-Schottky analysis on frequency, applied potential and electrolyte, results from different studies might not be comparable.

References

[1] J.-O. Nilsson. "Super duplex stainless steels". In: *Materials Science and Technology* 8.8 (1992), pp. 685–700. DOI: 10.1179/mst.1992.8.8.685.

[2] ASM International Handbook Committee. *Corrosion. ASM Handbook, Volume 13*. Materials Park, Ohio: ASM International, 2005.

[3] R. Johnsen. *Project description: Corrosion properties of stainless steel in seawater after removal of cathodic protection*. 2017.

[4] H.H. Olavesen. "The Effect of Hydrogen on the Corrosion Resistance of Super Duplex Stainless Steel in Seawater". Project Thesis, Norwegian University of Science and Technology. 2017.

[5] M.F. McGuire. *Stainless Steels for Design Engineers*. ASM International, 2008.

[6] H.K.D.H. Bhadeshia and R.W.K. Honeycombe. *Steels*. 3rd edition. Oxford: Butterworth-Heinemann, 2006.

[7] T. Newson. *Stainless steels - Applications, grades and human exposure*. 2002. URL: http://aplicainox.org/sitio/wp-content/uploads/2010/11/02D1.pdf (visited on 11/25/2017).

[8] E.B. Haugan et al. "Effect of Tungsten on the Pitting and Crevice Corrosion Resistance of Type 25Cr Super Duplex Stainless Steels". In: *Corrosion* 73.1 (2017), pp. 53–67. DOI: 10.5006/2185.

[9] J.K. Solberg. *Teknologiske metaller og legeringer*. 1st edition. Trondheim: NTNU, 2014.

[10] J.M. Pardal et al. "Deleterious phases precipitation on superduplex stainless steel UNS S32750: characterization by light optical and scanning electron microscopy". In: *Materials Research* 13.3 (2010), pp. 401–407. DOI: 10.1590/S1516-14392010000300020.

[11] M. Solnørdal et al. "Hydrogen Induced Stress Cracking (HISC) and DNV-RP-F112". In: *Measurement and Control* 42.5 (2009), pp. 145–148. DOI: 10.1177/002029400904200504.

[12] K. Sugimoto and Y. Sawada. "The role of molybdenum additions to austenitic stainless steels in the inhibition of pitting in acid chloride solutions". In: *Corrosion Science* 17.5 (1977), pp. 425–445. DOI: 10.1016/0010-938X(77)90032-4.

[13] I. Olefjord and B.-O. Elfstrom. "The Composition of the Surface during Passivation of Stainless Steels". In: *Corrosion* 38.1 (1982), pp. 46–52. DOI: 10.5006/1.3577318.

[14] A.P. Bond and E.A. Lizlovs. "Anodic Polarization of Austenitic Stainless Steels in Chloride Media". In: *Journal of The Electrochemical Society* 115.11 (1968), pp. 1130–1135. DOI: 10.1149/1.2410923.

[15] J. Horvath and H.H. Uhlig. "Critical Potentials for Pitting Corrosion of Ni, Cr-Ni, Cr-Fe, and Related Stainless Steels". In: *Journal of The Electrochemical Society* 115.8 (1968), pp. 791–795. DOI: 10.1149/1.2411433.

[16] *Iron-Nickel Phase Diagram*. URL: http://www.calphad.com/iron-nickel.html (visited on 12/11/2017).

[17] N. Pettersson, R.F.A. Pettersson, and S. Wessman. "Precipitation of Chromium Nitrides in the Super Duplex Stainless Steel 2507". In: *Metallurgical and Materials Transactions A* 46.3 (2015), pp. 1062–1072. DOI: 10.1007/s11661-014-2718-y.

[18] D. Zou et al. "Sigma phase precipitation and properties of super-duplex stainless steel UNS S32750 aged at the nose temperature". In: *Journal of Wuhan University of Technology-Materials Science Edition* 26.2 (2011), p. 182. DOI: 10.1007/s11595-011-0193-5.

[19] J.W. Elmer, T.A. Palmer, and E.D. Specht. "Direct Observations of Sigma Phase Formation in Duplex Stainless Steels Using In-Situ Synchrotron X-Ray Diffraction". In: *Metallurgical and Materials Transactions A* 38.3 (2007), pp. 464–475. DOI: 10.1007/s11661-006-9076-3.

[20] P. Paulraj and R. Garg. "Effect of Intermetallic Phases on Corrosion Behavior and Mechanical Properties of Duplex Stainless Steel and Super-Duplex Stainless Steel". In: *Advances in Science and Technology Research Journal* 9.27 (2015), pp. 87–105. DOI: 10.12913/22998624/59090.

[21] C.W. Kovach. *High Performance Stainless Steels*. Nickel Development Institute, 2000.

[22] R.S. Yassar et al. "Microstructure–mechanical and chemical behavior relationships in passive thin films". In: *Thin Solid Films* 518.10 (2010), pp. 2757–2763. DOI: 10.1016/j.tsf.2009.08.032.

[23] C.R Clayton and Y.C. Lu. "A Bipolar Model of the Passivity of Stainless Steel: The Role of Mo Addition". In: *Journal of The Electrochemical Society* 133.12 (1986), pp. 2465–2473. DOI: 10.1149/1.2108451.

[24] R.D. Willenbruch et al. "An XPS and electrochemical study of the influence of molybdenum and nitrogen on the passivity of austenitic stainless steel". In: *Corrosion Science* 31 (1990). Passivation of metals and semiconductors, pp. 179–190. DOI: 10.1016/0010-938X(90)90106-F.

[25] M.F. Montemor et al. "The role of Mo in the chemical composition and semiconductive behaviour of oxide films formed on stainless steels". In: *Corrosion Science* 41.1 (1999), pp. 17–34. DOI: https://doi.org/10.1016/S0010-938X(98)00126-7.

[26] J. Yao et al. "The Electrochemical Behavior and Characteristics of Passive Film on 2205 Duplex Stainless Steel Under Various Hydrogen Charging Conditions". In: *Corrosion* 72.1 (2016), pp. 42–50. DOI: 10.5006/1811.

[27] M.Z. Yang, Q. Yang, and J.L. Luo. "Effects of hydrogen on passive film and corrosion of aisi 310 stainless steel". In: *Corrosion Science* 41.4 (1999), pp. 741–745. DOI: 10.1016/S0010-938X(98)00147-4.

[28] R.T. Loto. "Pitting corrosion evaluation of austenitic stainless steel type 304 in acid chloride media". In: *Journal of Materials and Environmental Science* 4.4 (2013), pp. 448–459.

[29] P. Marcus. *Corrosion Mechanisms in Theory and Practice*. 3rd edition. Hoboken, New Jersey: CRC Press, 2011.

[30] International Organization for Standardization. *Petroleum, petrochemical and natural gas industries - Materials selection and corrosion control for oil and gas production systems*. ISO 21457:2010. Geneva, Switzerland, 2010.

[31] L. Claeys et al. "Electrochemical hydrogen charging of duplex stainless steel". Unpublished article on the evaluation electrochemical hydrogen charging behaviour, and interaction between hydrogen and the microstructure of a duplex stainless steel. 2018.

[32] S. Thomas et al. "The Effect of Absorbed Hydrogen on the Corrosion of Steels: Review, Discussion, and Implications". In: *Corrosion* 73.4 (2017), pp. 426–436. DOI: 10.5006/2242.

[33] A. Bahadori. *Cathodic Corrosion Protection Systems*. 1st edition. Boston: Gulf Professional Publishing, 2014.

[34] F.C. Campbell. *Elements of Metallurgy and Engineering Alloys*. 1st edition. United States of America: ASM International, 2008.

[35] B.R.S. da Silva, F. Salvio, and D.S. dos Santos. "Hydrogen induced stress cracking in UNS S32750 super duplex stainless steel tube weld joint". In: *International Journal of Hydrogen Energy* 40.47 (2015), pp. 17091–17101. DOI: 10.1016/j.ijhydene.2015.08.028. URL: http://www.sciencedirect.com/science/article/pii/S0360319915021047.

[36] R.W. Revie. *Uhlig's Corrosion Handbook*. 3rd edition. Hoboken, New Jersey: John Wiley & Sons, 2011.

[37] D.S. Schmool. *Solid State Physics - From the Material Properties of Solids to Nanotechnologies*. Mercury Learning and Information, 2017.

[38] H. Xiao. *Introduction to Semiconductor Manufacturing Technology*. 2nd edition. SPIE, 2012.

[39] A. Fattah-alhosseini and S. Vafaeian. "Comparison of electrochemical behavior between coarse-grained and fine-grained AISI 430 ferritic stainless steel by Mott–Schottky analysis and EIS measurements". In: *Journal of Alloys and Compounds* 639 (2015), pp. 301–307. DOI: 10.1016/j.jallcom.2015.03.142.

[40] R.M. Fernández-Domene et al. "Effect of temperature on the passive state of Alloy 31 in a LiBr solution: Passivation and Mott-Schottky analysis". In: *Materials and Corrosion* 66.11 (2015), pp. 1305–1314. DOI: 10.1002/maco.201508263.

[41] M.J. Carmezim et al. "Capacitance behaviour of passive films on ferritic and austenitic stainless steel". In: *Corrosion Science* 47.3 (2005), pp. 581–591. DOI: 10.1016/j.corsci.2004.07.002.

[42] I.H. Toor. "Mott-Schottky analysis of passive films on Si containing stainless steel alloys". In: *Journal of The Electrochemical Society* 158.11 (2011), pp. C391–C395. DOI: 10.1149/2.083111jes.

[43] I.H. Toor, M. Ejaz, and H.S. Kwon. "Mott-Schottky analysis of passive films on Cu containing Fe-20Cr-xCu (x=0, 4) alloys". In: *Corrosion Engineering, Science and Technology* 49.5 (2014), pp. 390–395. DOI: 10.1179/1743278214Y.0000000154.

[44] K. Darowicki, S. Krakowiak, and P. Ślepski. "Selection of measurement frequency in Mott–Schottky analysis of passive layer on nickel". In: *Electrochimica Acta* 51.11 (2006), pp. 2204–2208. DOI: 10.1016/j.electacta.2005.04.079.

[45] Z. Feng et al. "Passivity of 316L stainless steel in borate buffer solution studied by Mott–Schottky analysis, atomic absorption spectrometry and X-ray photoelectron spectroscopy". In: *Corrosion Science* 52.11 (2010), pp. 3646–3653. DOI: 10.1016/j.corsci.2010.07.013.

[46] N.B. Hakiki et al. "The electronic structure of passive films formed on stainless steels". In: *Corrosion Science* 37.11 (1995), pp. 1809–1822. DOI: 10.1016/0010-938X(95)00084-W.

[47] L.Q. Guo et al. "Effect of hydrogen on semiconductive properties of passive film on ferrite and austenite phases in a duplex stainless steel". In: *Scientific Reports* 7.1 (2017), pp. 3317–3322. DOI: 10.1038/s41598-017-03480-8.

[48] M. Inagaki and F. Kang. *Materials Science and Engineering of Carbon - Characterization*. Elsevier, 2016.

[49] J.M. Wagner. *X-ray Photoelectron Spectroscopy.* New York: Nova Science Publishers, Inc, 2011.

[50] International Organization for Standardization. *Corrosion of metals and alloys - Crevice corrosion formers with disc springs for flat specimens or tubes made from stainless steel.* ISO 18070:2015. Geneva, Switzerland, 2015.

[51] ASTM International. *Standard Test Method for Electrochemical Critical Pitting Temperature Testing of Stainless Steels.* ASTM G150-13. West Conshohocken, Pennsylvania, 2013.

[52] D.A. Shirley. "High-Resolution X-Ray Photoemission Spectrum of the Valence Bands of Gold". In: *Phys. Rev. B* 5 (12 1972), p. 4709 4714. DOI: 10.1103/PhysRevB.5.4709.

[53] L.Q. Guo et al. "Effect of hydrogen on pitting susceptibility of 2507 duplex stainless steel". In: *Corrosion Science* 70 (2013), pp. 140–144. DOI: 10.1016/j.corsci.2013.01.022.

[54] S. Thomas et al. "The effect of absorbed hydrogen on the dissolution of steel". In: *Heliyon* 2.12 (2016). DOI: 10.1016/j.heliyon.2016.e00209.

[55] M.-S. Choi et al. "Effect of Pickling Treatment on the Pitting Corrosion of Hyper Duplex Stainless Steel in a Highly Concentrated Chloride Solution". In: *Materials Transactions* 54.9 (2013), pp. 1779–1787. DOI: 10.2320/matertrans.M2013093.

[56] J.M. Drugli and T. Rogne. *Korrosjonsegenskaper, materialvalg og bruksområder ofr rustfrie stål- og nikkellegeringer.* SINTEF Materialteknologi, 1997.

[57] M. Li et al. "The mechanism of hydrogen-induced pitting corrosion in duplex stainless steel studied by SKPFM". In: *Corrosion Science* 60 (2012), pp. 76–81. DOI: 10.1016/j.corsci.2012.04.010.

[58] V. Maurice, W.P. Yang, and P. Marcus. "X-Ray Photoelectron Spectroscopy and Scanning Tunneling Microscopy Study of Passive Films Formed on (100) Fe-18Cr-13Ni Single-Crystal Surfaces". In: *Journal of The Electrochemical Society* 145.3 (1998), pp. 909–920. DOI: 10.1149/1.1838366.

[59] Q. Yang and J.L. Luo. "Effects of Hydrogen on Disorder of Passive Films and Pitting Susceptibility of Type 310 Stainless Steel". In: *Journal of The Electrochemical Society* 148.1 (2001), B29–B35. DOI: 10.1149/1.1344529.

[60] W.-T. Tsai, K.-M. Tsai, and C. Lin. "Selective corrosion in duplex stainless steel". In: San Diego, California: NACE International, 2003.

[61] C. Marconnet et al. "Chemical composition and electronic structure of the passive layer formed on stainless steels in a glucose-oxidase solution". In: *Electrochimica Acta* 54.1 (2008), pp. 123–132. DOI: 10.1016/j.electacta.2008.02.070.

Appendices

A Material specification sheets

Below follows the material specification sheets for batch 1 and batch 2 of the UNS S32750 samples and the material specification sheet for the UNS S31254 samples used in the experimental work.

outokumpu
high performance stainless steel

CERTIFICATE - ZEUGNIS - CERTIFICAT

EN 10204-3.1

2428050-EN

Invoice No. / Rechnung Nr. / N° de facture: 6610/1000543235

Business Unit / QCM	Date Datum Date	Load, Ladung, Charge No	Acknowledged ID, Bestätigung, Commande ID
Avesta Works / Johan Nordström	10-Mar-2017	NO/148472	6610/300392951

Your ref, Ihre Ref., Votre ref
821163 Ove Mæhle.

Buyer, Besteller, Acheteur
Sverdrup Steel AS
Strandsvingen 2
NO 4032, Stavanger
NORWAY

Consignee, Empfänger, Lieu de livraison
Sverdrup Steel AS

Requirements, Anforderungen, Exigences
ASTM A 240M-16a
ASME BPVC SEC II PART A SA-240/SA-240M 2015
EN 10088-2:2014
EN 10028-7:2016
NACE MR0175/ISO 15156-3:2015
EN 10088-4:2009
NORSOK Standard M-630, Ed 6, MDS D55, Rev 5
EN ISO 9445-2

Mark of Manufacturer / Zeichen des Lieferwerkes / Signe de producteur	Process / Erschmelzungsart / Mode de fusion	Inspector's stamp / Zeichen des Sachverständigen / Poicon de l'expert	Grade, Werkstoff, Nuance
outokumpu	E+AOD	AJA	Outokumpu Forta SDX 2507 UNS S32750 1.4410

Product, Erzeugnisform, Produit
Stainless Steel Cold Rolled, Coil-Plate
finish 2E, pickled, cut edge

Line / Reihe / Ligne	Item / Position / Poste	Heat-Lot No / Schmelze-Lot Nr / Coulée n° - Lot No	Size / Abmessungen / Dimensions	Pieces / Stückzahl / Nombre	Quantity / Unit / Menge / Einheit / Quantité / Unité	
1	4	570167-005	3,00 X 1500 X 3000 mm	19	2022 KG	

Chemical composition – Chemische Zusammensetzung – Composition chimiques

	C	Si	Mn	P	S	Cr	Ni	Mo	Cu	N
Heat	.017	.38	.75	.029	.001	25.02	6.87	3.79	.27	.276

Radioactive contamination check acc. IAEA recommendations: Approved

Test results – Prüfergebnisse – Results dessais (1N/mm² = 1 MPa) F = Front – Anfan – Debut B = Back – Ende – Fin T = Transverse – Quer – Travers

Test Ref		Temp °C	RP 0.2 N/MM2	RP 1.0 N/MM2	RM N/MM2	A5 %	2" %	HB HB	FEH %
Min		+20	550		795	25	15		35.0
Max					1000			310	55.0
F	T	+20	720	802	917	34	32	270	50.0
B	T		729	801	912	33	32	270	46.0

Corrosion acc. EN ISO 3651-2C: Approved
Material conforms to NACE MR0175/ISO 15156 in supplied condition
PREN: Cr + 3,3Mo + 16N = 41.9
Heat treatment / Solution annealed: Material temp minimum 1160 °C / Quenched (forced air + water)
All supplied items fulfill the heat treatment requirements, including time, temperature and speed, acc. to the qualified procedure
QTR No: 2507 - 2014
Corrosion acc. ASTM G 48-A 50 °C - 24H: Approved
Intermetallic phases and/or precipitates acc. to NORSOK MDS D55 Rev. 5: No indications
Steel grade verification (PMI-spectroscopic): Approved
Marking, visual insp. and gauge measurement: Approved
Certified acc. Pressure Equipment Directive (2014/68/EU) by TÜV CERT-Certification body for pressure equipment of the TÜV NORD Systems; notified body, reg-no. 0045.
Microstructure acc to ASTM A 923-A: Approved

Outokumpu Stainless AB
Business Unit Special Coil
BOX 74, S-774 22 AVESTA
SWEDEN
Regoffice: Stockholm SWEDEN, Regno: 556001-8748

Telephone: + 46 (0)226 811 73
Fax: + 46 (0)226 816 46
V.A.T no: SE556001874801

This material is found to comply with order requirements

Joakim Johansson
Authorized Inspector

TÜV NORD CERT GmbH ISO 9001

CE 10
0045 – CPR – 0869
Declaration of Performance (DoP): See www.outokumpu.com/Avesta-DoP

outokumpu
high performance stainless steel

CERTIFICATE - ZEUGNIS - CERTIFICAT

EN 10204-3.1
2439259-EN

Invoice No. / Rechnung Nr. / N° de facture: 6610/1000561811
Page / Seite / Page: 1/2

Business Unit / QCM	Date Datum Date	Load, Ladung, Charge No	Acknowledged ID, Bestätigung, Commande ID
Avesta Works / Johan Nordström	11-May-2017	NO/151659	6610/300427641

Your ref, Ihre Ref., Votre ref
824760

Buyer, Besteller, Acheteur
Sverdrup Steel AS
Strandsvingen 2
NO 4032, Stavanger
NORWAY

Consignee, Empfänger, Lieu de livraison
Sverdrup Steel AS

Requirements, Anforderungen, Exigences
ASTM A 240M-16a
ASME BPVC SEC II PART A SA-240/SA-240M 2015
EN 10088-2:2014
EN 10028-7:2016
NACE MR0175 / ISO 15156-3:2015
EN 10088-4:2009
NORSOK Standard M-630, Ed 6, MDS D55, Rev 5
EN ISO 9445 / ASTM A 480

Mark of Manufacturer / Zeichen des Lieferwerkes / Signe de producteur	Process / Erschmelzungsart / Mode de fusion	Inspector's stamp / Zeichen des Sachverständigen / Poicon de l'expert	Grade, Werkstoff, Nuance
outokumpu	E+AOD	AJA	Outokumpu Forta SDX 2507 UNS S32750 1.4410

Product, Erzeugnisform, Produit
Stainless Steel Cold Rolled, Coil-Plate
finish 2E, pickled, cut edge

Line / Reihe / Ligne	Item / Position / Poste	Heat-Lot No / Schmelze-Lot Nr / Coulée n° - Lot No	Size / Abmessungen / Dimensions	Pieces / Stückzahl / Nombre	Quantity / Unit / Menge / Einheit / Quantité	
1	13	571361-004	3,00 X 1500 X 3000 mm	48	5100 KG	

Chemical composition – Chemische Zusammensetzung – Composition chimiques

	C	Si	Mn	P	S	Cr	Ni	Mo	Cu	N
Heat	.017	.35	.78	.027	.001	24.73	6.94	3.79	.31	.270

Radioactive contamination check acc. IAEA recommendations: Approved

Test results – Prüfergebnisse – Results dessais (1N/mm² = 1 MPa) F = Front – Anfan – Debut B = Back – Ende – Fin T = Transverse – Quer – Travers

Test Ref		Temp °C	RP 0.2 N/MM2	RP 1.0 N/MM2	RM N/MM2	A5 %	2" %	HB HB	FEH %
Min		+20	550		795	25	15		35.0
Max					1000			310	55.0
F	T	+20	721	790	899	31	30	264	47.0
B	T		708	784	894	33	32	270	48.0

Corrosion acc. EN ISO 3651-2C: Approved
Material conforms to NACE MR0175/ISO 15156 in supplied condition
PREN: Cr + 3,3Mo + 16N = 41.6
Heat treatment / Solution annealed: Material temp minimum 1160 °C / Quenched (forced air + water)
All supplied items fulfill the heat treatment requirements, including time, temperature and speed, acc. to the qualified procedure
QTR No: 2507 - 2014
Corrosion acc. ASTM G 48-A 50 °C - 24H: Approved
Intermetallic phases and/or precipitates acc. to NORSOK MDS D55 Rev. 5: Indications, reference photomicrograph appended
Steel grade verification (PMI-spectroscopic): Approved
Marking, visual insp. and gauge measurement: Approved
Certified acc. Pressure Equipment Directive (2014/68/EU) by TÜV CERT-Certification body for pressure equipment of the TÜV NORD Systems; notified body, reg-no. 0045.
Photomicrograph: Page 2, ID: 2713039063B. Etchant: V2A, Magnification: X400

Outokumpu Stainless AB
Business Area Europe
BOX 74, S-774 22 AVESTA
SWEDEN
Regoffice: Stockholm SWEDEN, Regno: 556001-8748

Telephone: + 46 (0)226 811 73
Fax: + 46 (0)226 816 46
V.A.T no: SE556001874801

This material is found to comply with order requirements

Joakim Johansson
Authorized Inspector

TÜV NORD CERT GmbH ISO 9001

CE 10
0045 – CPR – 0869
Declaration of Performance (DoP): See www.outokumpu.com/Avesta-DoP

outokumpu
high performance stainless steel

CERTIFICATE - ZEUGNIS - CERTIFICAT

EN 10204-3.1
2367642-EN

Invoice No. / Rechnung Nr. / N° de facture: 6610/1000440228
Page / Seite / Page: 1/1

Business Unit / QCM	Date Datum Date	Load, Ladung, Charge No	Acknowledged ID, Bestätigung, Commande ID
Avesta Works / Johan Nordström	05-Apr-2016	NO/132462	6610/300367790

Your ref, Ihre Ref., Votre ref
818423 Linda Oaland.

Buyer, Besteller, Acheteur
Sverdrup Steel AS
Strandsvingen 2
NO 4032, Stavanger
NORWAY

Consignee, Empfänger, Lieu de livraison
Sverdrup Steel AS

Requirements, Anforderungen, Exigences
ASTM A 240M-15b
ASME SEC II PART A SA-240/SA-240M 2015
EN 10088-2:2014
EN 10028-7:2007
NACE MR0175/ISO 15156-3:2015
EN 10088-4:2009
NORSOK Standard M-630, Ed 6, MDS R15, Rev 5
EN ISO 9445-2

Mark of Manufacturer / Zeichen des Lieferwerkes / Signe de producteur	Process / Erschmelzungsart / Mode de fusion	Inspector's stamp / Zeichen des Sachverständigen / Poicon de l'expert	Grade, Werkstoff, Nuance
outokumpu	E+AOD	AJA	Outokumpu 254 SMO UNS S31254 1.4547

Product, Erzeugnisform, Produit
Stainless Steel Cold Rolled, Coil-Plate
finish 2E, pickled, cut edge

Line / Reihe / Ligne	Item / Position / Poste	Heat-Lot No / Schmelze-Lot Nr / Coulée n° - Lot No	Size / Abmessungen / Dimensions	Pieces / Stückzahl / Nombre	Quantity / Unit / Menge / Einheit / Quantité / Unité
1	7	553942-007	3,00 X 1500 X 3000 mm	47	5094 KG

Chemical composition – Chemische Zusammensetzung – Composition chimiques

	C	Si	Mn	P	S	Cr	Ni	Mo	Nb	Cu	Co	N
Heat	.017	.30	.55	.019	.001	20.10	18.36	6.37	.010	.81	.780	.200

Radioactive contamination check acc. IAEA recommendations: Approved

Test results – Prüfergebnisse – Results dessais (1N/mm² = 1 MPa) F = Front – Anfan – Debut B = Back – Ende – Fin T = Transverse – Quer – Travers

Test Ref		Temp °C	RP 0.2 N/MM2	RP 1.0 N/MM2	RM N/MM2	A5 %	2" %	HB HB
Min		+20	320	350	690	35	35	
Max					850			223
F	T	+20	384	433	726	51	49	183
B	T		375	429	719	52	49	183

Corrosion acc. EN ISO 3651-2C: Approved
Heat treatment / Solution annealed: Material temp minimum 1240 °C / Quenched (forced air + water)
All supplied items fulfill the heat treatment requirements, including time, temperature and speed, acc. to the qualified procedure
QTR No: 254SMO - 2014
Material conforms to NACE MR0175/ISO 15156 in supplied condition
Corrosion acc. ASTM G 48-A 50 °C - 24H: Approved
Steel grade verification (PMI-spectroscopic): Approved
Marking, visual insp. and gauge measurement: Approved
Certified acc. Pressure Equipment Directive (97/23/EC) by TÜV CERT-Certification body for pressure equipment of the TÜV NORD Systems; notified body, reg-no. 0045.

Outokumpu Stainless AB
Business Unit Special Coil
BOX 74, S-774 22 AVESTA
SWEDEN
Regoffice: Stockholm SWEDEN, Regno: 556001-8748

Telephone: + 46 (0)226 811 73
Fax: + 46 (0)226 816 46
V.A.T no: SE556001874801

This material is found to comply with order requirements

Joakim Johansson
Authorized Inspector

TÜV NORD ISO 9001

CE 10
0045 – CPR – 0369
Declaration of Performance (DoP) See www.outokumpu.com/Avesta-DoP

Pickling procedure for the steel samples

In this section a detailed description of the pickling process Framo performed on the stainless steel used in this project is found.

RUTINE FOR BEISING

Hensikt

Rutinen skal sikre at beising gjennomføres etter en standardisert metode som ivaretar bedriftens krav til kvalitet og personlig sikkerhet.

Ansvar

Operatør ved beis er ansvarlig for at beising gjennomføres ihht.gjeldene rutine.

OPERATØR SKAL

Alltid bruke egnet verneutstyr ved arbeid i beisehall; vernestøvler, hansker og egnet kjeledress.

- Når håndbeising pågår skal hel kjemikaliedress og friskluftsmaske med hette benyttes.
- Når deler spyles med høytrykkspyler etter beis, skal friskluftsmaske med visir benyttes.

Ha gjort seg kjent med utstyret gjennom nødvendig opplæring.

Kun benytte godkjente beisevæsker, det vil si væsker som er registrert i stoffkartotek med gyldige datablad.

Kun benytte løfteutstyr som er av rustfritt stål og syntetiske stropper.

Påse at det **ikke** foregår arbeid i beisehall hvis lokk i syrekar er åpent.

RUTINE FOR PICKLING

Purpose

This routine shall ensure that pickling is executed using a standardized method and that the company's requirements for quality and personal safety are maintained.

Responsibility

The operator is responsible for ensuring that the work is carried out according to the prevailing routine.

OPERATOR SHALL

Always use suitable protection while working in the pickling hall: protective footwear, gloves and appropriate coveralls.

- Under pickling by hand a chemical suit and supplied air respirator with hood shall be used.
- When parts are flushed with a pressure washer after pickling, a supplied air respirator with a visor shall be used.

Have familiarized themselves with the equipment through sufficient training.

Only use approved pickling medium, i.e. fluids registered in the substance index with valid data sheets.

Only use lifting equipment that are of stainless steel and synthetic straps.

Ensure that there is **no** ongoing work in the pickling hall if the lid of the acid tank is open.

Beise rutine

Beisen inneholder:

SALPETERSYRE	HNO_3
ca 130 g/l	
FLUSSYRE	HF
ca 24 g/l	
VANNSTOFFPEROKSYD	H_2O_2
25 - 30 l/døgn	

Beisetemperatur: 32 - 35 ºC

Beising skal alltid skje ihht følgende prosess

Operasjoner i beisehall (vernestøvler og hansker skal benyttes):

- Inspisere deler som skal beises og påse at de er fri for slagg og skader.
- Samle deler som skal beises og legge de forsvarlig i beisekorg.
- Korg løftes over i biokar ved hjelp av traverskran.

Operasjoner fra kontrollrom:

- Korg flyttes fra biokar til syrekar. Stropper skal alltid ligge over kanten på syrekar når beising pågår. Traverskran skal brukes. Lukke lokk på syrekar. I de tilfeller hvor deler i korg eller del er av en slik karakter at lokk i syrekar ikke kan lukkes, skal hovedbryter til kran slåes av. Det er da **ikke** tillatt å oppholde seg i beisehall.
- Beisetid ihht tabell.

Pickling routine

The pickle medium consists of:

Nitric acid	HNO_3
ca 130 g/l	
Hydrofluoric acid	HF
ca 24 g/l	
Hydrogen peroxide	H_2O_2
25 - 30 l/day	

Pickling temperature: 32 - 35 ºC

Pickling shall always be done according to the following process

Operations in the pickling hall (protective shoes and gloves shall be used):

- Inspect parts that shall be pickled to ensure that they are free of slag and damages.
- Collect parts that shall be pickled and place them properly in the pickling basket.
- The basket is to be lifted into the bio tank by using the traverse crane.

Operations from the control room:

- The basket is moved from the bio tank to the acid tank. Straps shall always be placed over the edge of the acid tank during the pickling process. Travers crane shall be used. The lid of the acid tank shall be closed. In cases where parts in the basket or the dimension of the part prevent closing of the lid, the main switch of the crane shall be turned off. Under these conditions it is **not** permitted to reside in the pickling hall.
- Pickling time according to table.

Operasjoner i beisehall (Vernestøvler og hansker skal benyttes):

- Stropper løsnes fra kran.
- Annet arbeid i beishall kan pågå når lokk i syrekar er lukket.

Operasjoner fra kontrollrom:

- Korg løftes opp av syrekar og overrisslingsanlegg skal brukes når korg er hengende over karet. Påse at avrenning er stoppet før korg er klar for skyllekar.
- Korg løftes over i skyllekar ved hjelp av traverskran og lokk til syrekar skal lukkes. Påse at stropper senkes lengre ned i skyllekaret enn de var i syrekar. Skyll grundig.
- Korg løftes over til spyleområde ved hjelp av traverskran. Settes over rist i gulv.

Operasjoner fra beisehall (Vernestøvler, *hansker*, friskluftsmaske og kjemikaliedress skal benyttes):

- Spyle/rengjøre deler med høytrykkspyler. Deler skal dusjes, før høyt trykk blir benyttet. Dette for å sikre avrenning av eventuelle syrerester. Temperert vann skal benyttes. Spyling skal pågå til alt løst avfall i overflaten er borte.
- Visuell kontroll av overflaten skal utføres. I de tilfeller hvor det er tvil om kvaliteten på beisearbeidet skal formann kontaktes.

Operations in the pickling hall (protective shoes and gloves shall be used):

- Straps are detached from the crane.
- Other work in the pickling hall can commence when the lid of the acid tank is closed.

Operations from the control room:

- The basket is lifted up from the acid tank and the deluge system shall be used when the basket is hanging above the tank. Ensure that run-off has stopped before moving the basket to the rinsing tank.
- The basket is lifted into the rinsing tank by using the traverse crane, and the lid to the acid tank shall be closed. Ensure that straps are submerged further down into the rinsing tank than what they were in the acid tank. Rinse thoroughly.
- The basket is lifted over to the flushing area by using the traverse crane. Place the basket over the grate in the floor.

Operations from the pickling hall (protective shoes, gloves, supplied air respirator, and chemical suit shall be used):

- Flush/clean parts with a pressure washer. Parts shall be showered before high pressure is applied. This to ensure run-off of any acid remnants. Temperate water shall be used. Flushing shall continue until all loose contaminations on the surface are removed.
- Visual control of the surface shall be executed. In cases where there is doubt with regard to the quality of the

Beiserutine ved håndbeising

Følgende verneutstyr skal brukes ved håndbeising: Hel kjemikaliedress, friskluftmaske med hette, vernestøvler, gummihansker.

Ved utførelse av håndbeis, skal det alltid være to kvalifiserte operatører tilstede.
En for å utføre håndbeisingen og en for å for å overvåke arbeidet og påse at ikke uvedkommende kommer inn i beisehallen.

Etter håndbeising og skylling, skal det ventes i to timer før operatørene inspiserer håndbeisede tanker og frigir de til transport.

Alt utstyr som benyttes ved håndbeising skal fjernes straks håndbeisingen er utført.

Rester av beisepasta tynnes med vann og helles i syrekar.

Koster, filler etc. skylles ved rist og legges i container for spesialavfall.

Håndbeising skal alltid skje ihht følgende prosess:

- Påse at lufttemperatur ikke er under +5 grader C.
- Påse at sveist gods er kaldt.
- Rengjør godset slik at det er fritt for fett, olje, kjemiske avleringer, smuss og andre urenhet som ikke er forenelig med stålet før beising.
- Beisen omrøres godt i noen minutter før bruk.
- Påfør væsken med bruk av egnet kost eller sprøyte.
- Påfør væsken i et tynt lag over hele overflaten som skal behandles.
- La beisevæsken virke i 30-120 minutter eller lengre, avhengig av stålkvalitet og temperatur.

pickling work, the foreman shall be contacted.

Routine for pickling by hand

The following safety equipment shall be used when pickling manually: Chemical suit, supplied air respirator with hood, protective shoes and rubber gloves.

When executing pickling manually there shall always be two qualified operators present.
One to execute the operation and one to oversee the work and ensure that unauthorized persons do not enter the pickling hall.

After pickling and rinsing, the operator shall wait two hours before inspection of the tanks and releasing parts for transport.

All equipment that has been applied during the process shall be removed once the pickling has been performed.

Pickling paste leftovers are diluted with water and shall be poured into the acid tank.

Brushes, rags etc. are to be rinsed by the grate and placed in containers for special waste.

Manual pickling shall always be executed according to the following process:

- Ensure that air temperature is not under +5 grader C.
- Ensure that welded goods are cooled.
- Before pickling clean the goods so that it is free of grease, oil, chemical begets, dirt and other impurities that are not compatible with the steel.
- Pickle medium is to be agitated thoroughly for a few minutes prior to

- Skyll med temperert vann. Bruk høytrykkspyling.
- Beiserester skal nøytraliseres til PH7.

Renhold av beisehall og utstyr:

Beisehallen skal til enhver tid være ryddig og alt som ikke tilhører arbeid relatert til beiseprosessen skal fjernes.

Området rundt syrekar skal rengjøres grundig hver fredag. Friskluftsmaske og kjemikaliedress skal benyttes.

Stropper skal rengjøres daglig i eget kar for rengjøring. Dette skal utføres daglig. Vann i skyllekar for stropper byttes ukentlig.

Vinduer på kontrollrom mot beisehall skal rengjøres ukentlig.

use.

- Apply pickling medium by using an adequate brush or spray.
- Apply the pickling medium in a thin layer over the surface to be treated.
- Let the pickle work for 30-120 minutes depending on steel quality and temperature.
- Flush with temperate water. Use pressure washing.
- Pickling leftovers shall be neutralized to PH 7.

Cleaning pickling hall and equipment:

The pickling hall shall always be tidy, and equipment that is not related to the pickling process shall be removed.

The area around the acid tank shall be thoroughly cleaned every Friday. A supplied air respirator and a chemical suit shall be used.

Straps shall be cleaned daily in a separate tank for cleaning. Water in the rinsing tank for straps shall be changed weekly.

The windows of the control room towards the pickling hall shall be cleaned every week.

OVERSIKT OVER FRAMO FLATØY MATERIAL DATA ARK (MDS)	OVERVIEW OF FRAMO FLATØY'S MATERIAL DATA SHEETS (MDS).

MDS No.	***Populær Betegnelse (name)***	***Matr. Type***	***Beskrivelse (Description)***	***Beisetid min.* (pickling time min.*)***
001	316L	316L	Seamless /straight seam welded steel pipe	15-60
002	316L	316l	El. fusion welded austn. steel pipe HT serv.	15-60
003	316L	316L	Wrought austn. s.s. pipe fittings seaml./weld.	15-60
004	316L	316L	Forged or rolled pipe flanges/ forged fittings	15-60
007	316	316 B8M	Alloy-st./ s.s. bolting materials for h.temp. serv.	15-60
008	316	316	Carbon and alloy steel nuts for h.p/ h.temp serv.	15-60
009	316L	316L	Heat resisting stainless steel plate for pres.vess.	15-60
010	SMO/6MO	254 SMO	Heat resisting stainless steel plate for pres.vess.	30-150
011	SMO/6MO	254 SMO	Seamless /straight seam welded steel pipe	30-150
012	SMO/6MO	254 SMO	El. fusion welded austn. steel pipe HT serv.	30-150
013	SMO/6MO	254 SMO	Wrought aust. s.s. pipe fittings seaml./weld.	30-150
014	SMO/6MO	254 SMO	Forged or rolled pipe flanges/ forged fittings	30-150
017		SS gr. 660	Stainless steel bolting material	15-60
020	SUPERDUPLEX	UNS S-32750	Austenitic-ferritic castings for press.cont. parts.	60-240
021	SUPERDUPLEX	UNS S-32750	Seaml. and weld. ferritic/ austenitic SS pipes	60-240
022	SUPERDUPLEX	UNS S-32750	Heat resisting stainless steel plate for pres.vess.	60-240
023	DUPLEX	UNS S-31803	Seaml. and weld. ferritic/ austenitic SS pipes	30-150
024	DUPLEX	UNS S-31803	Austenitic-ferritic castings for press.cont. parts.	30-150
025	DUPLEX	UNS S-31803	Heat resisting stainless steel plate for pres.vess.	30-150
026	SUPERDUPLEX	UNS S-32750	Stainless and heat-resist. steel bars and shapes	60-240
027	SMO/6MO	UNS S-31254	Stainl. and heat-resist. steel bars for press.vess	60-240
028	DUPLEX	UNS S-31803	Stainless and heat-resist. steel bars and shapes	30-150
038	SMO/6MO	UNS S-31254	Castings, iron-chrom-nickel, corr. resist.	30-150
039	SMO/6MO	UNS S-31254	Austenitic/ ferritic castings for press.cont. parts.	30-150
040	DUPLEX	UNS S-31803	Wrought ferritic/austenitic SS piping fittings	30-150
041	DUPLEX	UNS S-31803	Forged or rolled pipe flanges/ forged fittings	30-150
043	SUPERDUPLEX	UNS S-32750	Forged or rolled pipe flanges/ forged fittings	60-240
044	SUPERDUPLEX	UNS S-32750	Wrought ferritic/austenitic SS piping fittings	60-240
049	DUPLEX	UNS S-31803	Longitudin. welded tubes f/ hyd. press line od 18	15-60
051	DUPLEX	UNS S-31803	Seaml. cold finished tubes f. hydr. press. lines.	15-60
052	316L	UNS S-31603	Austenitic, aust.-ferr. cast. for press.cont. parts.	15-60
063	BS5S.100	BS4S.100 S143	Precipitation hardening martensitic stainl. steel	15-60
068	DUPLEX	UNS S-31803	Ferritic/ Austenitic stainless steel pipes	15-60
100	DUPLEX	UNS S-31803	Ferritic/ Austenitic stainless steel forging	15-60
104	INCONEL	UNS N-06625	Inconel 625 plate	15-60
105	INCONEL	UNS N-06625	Inconel 625 pipe	15-60
106	INCONEL	UNS N-06625	Inconel 625 pipe	15-60
107	SUPERDUPLEX	UNS S-32750	Ferritic/austenitic SS piping and fittings	60-240

ANDRE MATERIAL BETEGNELSER (Other material terms)

BETEGNELSE (Name)	***Populær betegnelse (name)***	***Mat.type***	***Beskrivelse (description)***	***Beisetid min.* (pickling time min.*)***
UNS S-32750	SUPERDUPLEX			60-240
UNS S-32760	SUPERDUPLEX			60-240
UNS S-32550	SUPERDUPLEX			60-240
UNS S-31803	DUPLEX			15-60
UNS S-31603	316L			15-60
UNS S-31600	316L			15-60
W.NO. 1.4462	DUPLEX			15-60
6Mo	6Mo			30-150
AL6XN	SMO/6MO			30-150
[1]UNS R-3006	Stellite 6			10-20 1) ④
[1]UNS R-3012	Stellite 12			10-20 1) ④

1) Komponenter som skal pålegges Stellite 6 eller 12 må beises grundig før påleggingen. ④
1) Components that shall have Stellite 6 or 12 must be pickled thoroughly before applying.

Andre rutiner som gjelder beiseanlegget og beiseprosessen	**Other routines that apply the pickling hall and the pickling process**
Dok. Nr.: 70.3.12 Driftsrutine – Beiseanlegg Dok. Nr.: 70.3.22 Instruks for behandling av beisevæsker Dok. Nr.: 70.3.50 Prosedyre for oppjustering av syrebad Dok. Nr.: 70.2.16 Arbeidsinstruks for operatør, kjemisk overflatebehandling. Opplæringsplan for personell som utfører syrevasking/beising.	Doc. Nr. 70.3.12 – Operation routine - Pickling hall Doc. Nr. 70.3.22 – Instructions for treating pickling fluids Doc. Nr. 70.3.50 – Procedure for upward adjustments of acid bath Doc. Nr 70.2.16 – Work instructions for the operator, chemical surface treatment Training plan for personnel that conduct acid washing/pickling.